2005

Formation and properties of the PEO coatings on aluminum-silicon alloys.

Linlin Wang
University of Windsor

FORMATION AND PROPERTIES

OF THE PEO COATINGS ON Al-Si ALLOYS

By

Linlin Wang

A Thesis

Submitted to the Faculty of Graduate Studies and Research

through Engineering Materials

in Partial Fulfillment of the Requirements for

the Degree of Master of Applied Science at the

University of Windsor

Windsor, Ontario, Canada

2005

Your file Votre référence
ISBN: 0-494-09726-4
Our file Notre référence
ISBN: 0-494-09726-4

ABSTRACT

Plasma electrolytic oxidizing (PEO) of aluminium alloys is an advanced technique to deposit a thick and hard ceramic coating on a number of low Si content aluminium alloys. The rapid growth in the tribological applications of high Si cast Al-Si alloys has been motivating this study, i.e., development of a PEO coating with high wear resistance and low friction for high Si content cast Al-Si alloys.

In this research, the effect of substrate materials (i.e., silicon contents, Chapter 4) and process parameters (Chapter 5) on the PEO coating formation, microstructure, and composition were investigated in details. An oxide/graphite composite coating with low friction and high wear resistance was particularly developed and studied (Chapter 6).

Based on the observations of coating surface morphology change during the treatment, a coating growth model on the Si region was developed in Chapter 4. The PEO process had four stages where each stage was corresponding to different coating surface morphology, composition, and phase structure, characterized by different coating growth mechanisms. In the first three stages, the duration time and morphology of each stage were considerably affected by the silicon content in Al-Si alloys. The higher silicon content caused a rougher coating surface. After the process entered stage IV, the compositions of the oxide coatings for the Al alloys with different Si contents were similar.

Comparing study of coating depositions at different process parameters indicates that the coating produced in the high concentration electrolyte has larger thickness, rougher surface, a continuous dense layer in the between of outer porous layer and inner

dense layer, and more amounts of Al_2O_3-SiO_2 compound and α-Al_2O_3 phase. Current density effect on coating structure and coating hardness was not found to be significant.

The last part of study focuses on development of an oxide-graphite composite coating with improved tribological properties. The composite coating has a structure similar to a typical PEO coating except for having an oxide-graphite outer top layer. The composite layer in the oxide-graphite coating can supply graphite continuously, which results in formation of a solid lubricant layer at the interface during the sliding. Thus, the oxide-graphite composite coating has not only high wear resistance and low friction but also good compatibility to the steel counterface.

DEDICATION

TO MY HUSBAND

XIN HU

AND
MY PARENTS

ACKNOWLEDGEMENTS

I would like to express my sincere gratitude to Dr. Xueyuan Nie (Assistant professor, Department of Mechanical, Automotive and Materials Engineering), for his excellent supervision, encouragement for the research, and friendship.

Dr. A.T. Alpas is acknowledged for his comments, suggestions and most valuable technical support in the past two years. I would like to thank Drs. Jerry Sokolowski, Tom Perry and Henry Hu for provision of the Al-Si alloys. Thanks go to Dr. Y.T. Cheng for his assistance of XRD analysis.

I would like to extend my thanks to the group members, Ms. Yueyu Ma, Xia Li and Mr. Peng Zhang for their help and encouragement. Mr. J. Robinson's technical assistance during my graduate study is also gratefully acknowledged.

The financial supports from Natural Sciences and Engineering Research Council of Canada (NSERC), Canadian Foundation for Innovation, and Ontario Graduate Scholarship are very much appreciated.

TABLE OF CONTENTS

LIST OF TABLES

LIST OF FIGURES

CHAPTER 1 INTRODUCTION

The need to improve fuel economy and safety performance, reduce exhaust emissions and provide customers with new features have lead to new challenges in components design including reduced weight, reduced friction, and higher engine operating temperatures. Aluminium alloys are noted for their unique combination of desirable characteristics including their high strength-to-weight-ratio, good castability, low thermal expansion and high corrosion resistance. These properties have led to their substantial increase in the use of automotive and aircraft and aerospace industry. [1, 2]

3xx.0 series cast aluminium-silicon alloys have been increasingly applied as lightweight components especially using for all types of internal combustion engines as pistons, cylinder blocks and cylinder heads. In these alloys, silicon is added to aluminium to form a second phase in order to improve wear resistance for tribological applications. However, compared with iron and steel, aluminium alloys are relatively soft and have poor wear properties especially against scuffing wear under conditions of poor lubrication such as those which exist during starting or warming-up of engines. It is one of the main failure mechanisms affecting the life of engines. [3-5]

There are two main methods to improve the friction and wear properties of aluminium alloys. One is the application of Al-Matrix Composites (AMC), the other is achieved by surface coatings on aluminium alloys.

The AMCs have been widely considered for automotive and aerospace application. They exist in forms of fiber (C, SiC, B and Al_2O_3) reinforcement in particulate and whisker (SiC and Al_2O_3) as well as in layered laminated structures (sandwich structure of aluminum and aramid or glass/epoxy for high performance fatigue critical applications)

[6]. Processes for fabrication of AMCs include liquid state methods (sorted into infiltration process, dispersion process, spraying process, and in-situ fabrication process) and solid state methods (powder metallurgy, roll bonding and coextrusion) [7]. Among those, powder metallurgy (PM), molten metal processes and spray casting are the main processes applied for the fabrication of Al-Matrix Composites (AMC) [5, 8, 9].

The other method is involved in surface coating to eliminate the possibility of sever wear by hardening the surface and lowing friction. Various coatings have been developed to improve surface hardness and wear properties of the alloys. Titanium nitride and diamond-like carbon (DLC) coatings are deposited by vacuum vapour deposition (PVD and CVD) methods which require high vacuum in vacuum chambers [10,11]. Electroplating and electroless plating-Nickel based ceramic composite coatings (NCC) can increase the wear resistance but may be corroded if sulphur-contained fuel is used [10-12]. Thermal spraying technology can produce Fe-based or stainless steel-Ni-BN coatings. However, thermal spraying only produce mechanical adhesion of coatings to base materials, and precise process control (including surface pre-treatment) is vital for provision of good adhesion between coating and Al baselines [10,11,13]. Operating challenges still exist in producing spraying-coated Al cylinder interior surfaces in terms of economical manufacturing process, reproducible and reliable processing. Hard anodizing is an effective and equipment simple method used to produce hard ceramic coatings on aluminium alloys. Since alloying elements such as copper and silicon do not anodize during the process, leaving microscopic voids in the aluminum oxide coating, the coating exhibits a high friction coefficient and low peeling resistance. In general case, hard anodic coatings can not be applied to high Si (containing >8% silicon) alloys. [10,11,14]

Electrolytic plasma processing (EPP) is a relatively new plasma-assisted electrochemical treatment. It is considered as a cost-effective and environmentally friendly surface engineering technique and can be broadly applied to metal surface cleaning, metal-coating [15], carburizing, nitriding [16], and oxidizing [17-20].

The EPP for anodic oxidising process, called plasma electrolytic oxidation (PEO), in a silicate solution can produce Al-Si-O ceramic coatings with a high adhesion, hardness, and thickness on Al-based materials. Moreover, PEO process combining with other processes such as CVD [21] and electrophoretic deposition (EPD) [22] can be used in producing superhard, low friction, and/or biomedical compatible coatings.

Several studies have been involved in the coating formation mechanisms [20, 23, 24], characteristics of the coating deposition as well as tribological properties [18-20] of the ceramic oxide coatings deposited using PEO on various Al alloy substrates. Most of those works only dealed with 2xxx and 6xxx series, i.e., low silicon (<1.5% Si) content Al alloys, and characterized thick oxide coating (i.e., >100 μm in thickness). Little studies focus on the initial stage of the PEO coating formation and properties of the thin PEO coatings. Due to the rapid growth in applications of high silicon cast Al-Si alloys, the applications of the PEO on the cast Al-Si alloys have been paid more attention since recently. However, to our knowledge, a detailed investigation of the effects of silicon content in Al-Si alloys on the PEO coating formation and morphology has not been conducted yet.

Moreover, to produce a thick PEO coating the voltage required would be up to 600V-1000V and the treatment time over 60 mins. The process time is too long and

energy consumption is too high to be economically viable for treatments of most powertrain components.

Finally, like most of other ceramic coatings, PEO coatings have high hardness and wear resistance, but high friction and poor compatibility with many counterface materials.

Thus, in this research, low voltages (<500V) were adopted to produce thin PEO coating with thickness less than 30 μm. The PEO process on high Si aluminium alloys was investigated in terms of the effect of Si content, electrical and electrolytic parameters on formation, morphology, composition of the PEO coatings. A ceramic-graphite composite coating was developed to improve its tribological and wear properties and compatibility with steel counterface.

This thesis consists of seven chapters. Following this introduction, the related literatures regarding PEO coating technology on Al alloys and the previous work on the PEO coating formation and properties are reviewed in Chapter 2. Chapter 3 describes the experimental procedures. Chapter 4 reports investigation results of silicon effects on formation of thin PEO oxide coatings on hypereutectic and hypoeutectic Al-Si alloys. Surface morphology, composition, microstructure and surface roughness of those coatings prepared at low current density and low electrolyte concentration are investigated. According to the results of this part of experiment, the growth model in the Si region is developed.

Chapter 5 presents the results and discussion of the effect of electrical and electrolytic parameters on the formation and properties of coatings. Herein, two electrolyte concentration (4g/l and 8g/l Na_2SiO_3) and three current densities (0.05A/cm^2,

0.1 A/cm^2 and $0.2A/cm^2$) are used to systematically study the formation and properties of coatings.

In Chapter 6, a new oxide-graphite composite coating was developed. The composite coating structure and mechanical and tribological properties are investigated. To study effect of testing conditions on wear properties, uncoated substrates and two oxide PEO coatings with different thickness were tested with dry and lube wear.

Finally, conclusions of the present study are summarized in Chapter 7.

CHAPTER 2 LITERATURE REVIEW

In the mid-1970's, an advanced anodizing process was developed by two Russian scientists, G.A. Markov and G.V. Markova [25, 26]. They investigated wear resistant property of coatings for lightweight metals. The technology has later come to be known as 'micro-arc-oxidation' (MAO) process [27]. In the 1980s, 'micro-arc' or 'electrical discharges' in the oxide deposition process were attempted to apply on various metals in Russia by Snezhko [28-33], Markov [34-36], Fyedorow [37], Gordienko, [38-40] and their coworkers. In Germany early industrial applications were introduced by Kurze and cowcorkers [41-49]. In the past years, researchers in both USA and China were also involved in this field. Owing to the relatively sparse information on process phenomenology and, sometimes, a lack of understanding, different (and not always physically correct) terminology has been used in much of the above studies for that is, essentially, the same technique: 'micro-plasma oxidation', 'anode spark electrolysis', 'plasma electrolytic anode treatment' (anode oxidation under spark discharge), being typical examples of descriptions common to 'plasma electrolytic oxidation' (PEO).

The process yields fully dense, extremely hard-nearly as hard as corundum-tenacious coatings on aluminum and aluminum alloy surface. An important characteristic of this coating is that the hard oxide layer actually grows inward from the aluminum substrate surface. Thus, good adhesion and dimensional stability of the part is possible and the parts in the nearly finished, machined condition can be coated. Unlike other superhard coatings (PVD, CVD coatings or hard anodizing alumina coatings), the coating is compliant for thicknesses up to 100μm. In view of the attractive properties, recently the

PEO coatings were investigated for component applications, in particular, powertrain parts.

This chapter overviews the previous studies on the characteristic phenomena during the PEO process, physical and chemical fundamentals of coating formation and the coating properties including mechanical, tribological and corrosion-protection. Finally, the industrial applications and challenges are described in this chapter.

2.1 The PEO equipment

The equipment used for PEO is relatively simple which is similar to that of conventional electroplating except for the need of much higher voltage power supply. Fig. 2.1(a) is the schematic of a typical treatment unit [50]. The treatment unit consists of an electrolyser (Fig. 2.1(b)) and a high power electrical source. The electrolyser is usually a water-cooler bath placed on a dielectric base and confined in a grounded steel frame, which has an insulated current supply and a window to observe the process in operation. In the bath, a stainless steel plate is immerged served as the counter-electrode. In some case, the electrolyser incorporates electrolyte mixing, recycling, and gas exhausting arrangements, as well as electrical interlocks.

Various types of power source can be used for the PEO process. According to the applied electrical regime they can be classified into DC sources, pulsed DC sources, unbalanced AC sources and heteropolar pulsed current sources.

To produce the PEO coatings on aluminium alloys, alkaline electrolytes are widely used, containing silicates, aluminates, polyphosphates, etc. which can promote strong metal passivation due to the formation of near-surface gels or insoluble compounds.

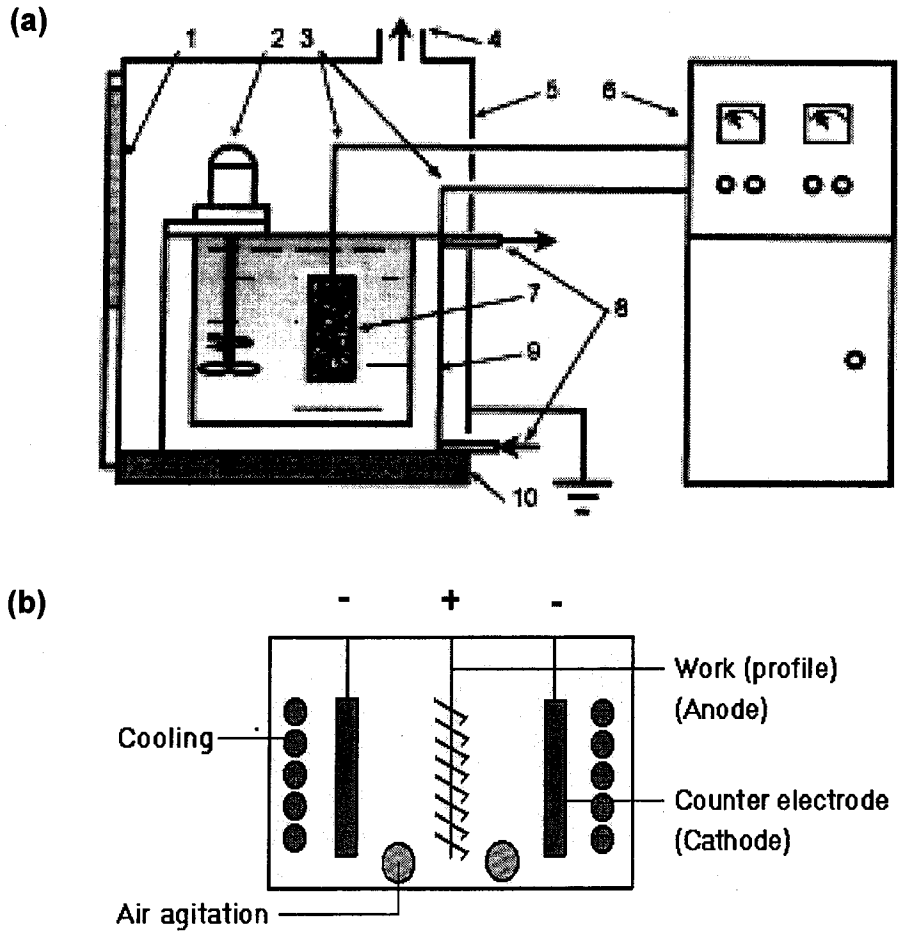

Fig. 2.1 (a) Typical arrangement of the equipment used for PEO treatment (1. window, 2. mixer, 3. connecting wires, 4. exhaust/ventilation system, 5. grounded case, 6. power supply unit, 7. workpiece, 8. cooling system, 9. bath, 10 insulating plate). (b) Electrolyte bath [50].

2.2 Deposition procedure

After simple pre-treatment consisting of cleaning and degreasing, the samples are attached to the current supply of the unit and typically immersed in the bath at a depth of 30mm to 50mm beneath the electrolyte surface. After the electrolyte cooling, mixing and gas exhaust are activated, the working voltage can be applied to the electrolyser terminal

and adjusted at the power supply in accordance with the selected treatment regime. Depending on the purpose, the PEO treatment is typically carried out for between 5 and 180min at current densities of 500-2000Am^{-2} and voltages of up to 1000V.

2.3 Phenomena during the PEO process

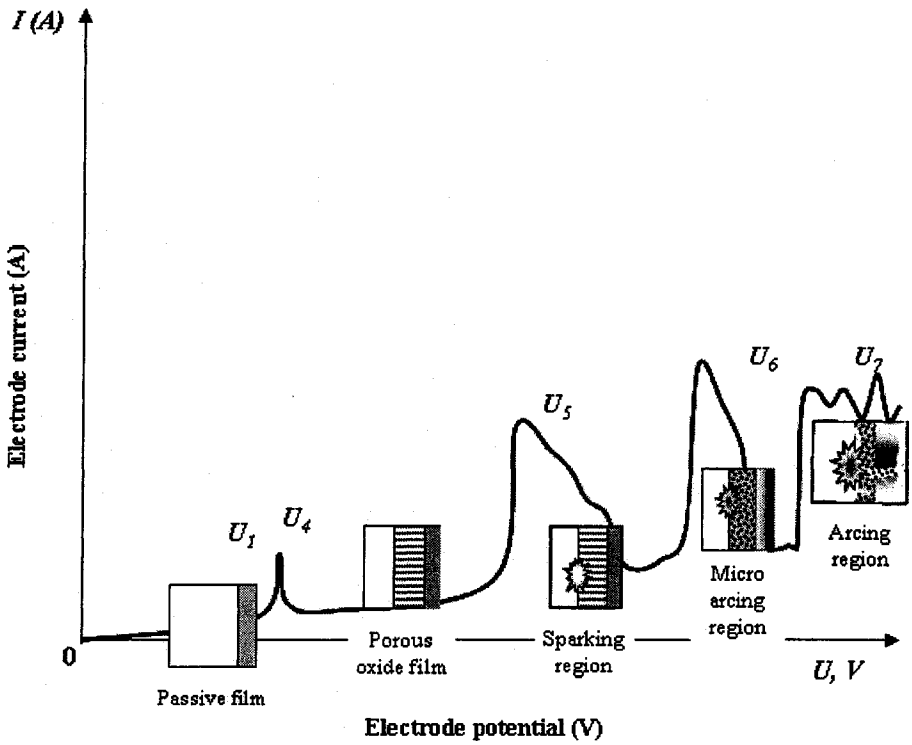

Fig. 2.2 Current-voltage diagram for the processes of plasma electrolysis: discharge phenomena are developed in the dielectric film on the electrode surface [50].

A.L. Yerokhin and X. Nie (1999) et. al. [50] overviewed electrical plasma process and described the current-voltage characteristics during the PEO process. Fig. 2.2 represents the current-voltage characteristics of a system where oxide film formation occurs during the PEO process. Firstly, the passive film previously formed begins to dissolve at point U_4, which, in practice, corresponds to the corrosion potential of the material. Then, in the region of repassivation U_4-U_5 a porous oxide film grows, across

which most of the voltage drop now occurs. At point U_5, the electric field strength in the oxide film reaches a critical value beyond which the film is broken through due to impact or tunnelling ionisation. At point U_6, the mechanism of impact ionisation is supported by the onset of thermal ionisation processes and slower, larger arc-discharges arise. In the region U_6-U_7, thermal ionisation is partially blocked by negative charge build-up in the bulk of the thickening oxide film, resulting in discharge-decay shorting of the substrate. Above the point U_7, the arc micro-discharges occurring throughout the film penetrate through to the substrate and (since negative charge blocking effects can no longer occur) transform into powerful arcs, which may cause destructive effects such as thermal cracking of the film.

A.L. Yerokhin et. al. (2003 and 2004) [51, 52] studied microdischarge using real time imaging of the plasma electrolytic oxidation process. By digital video imaging study of AC PEO of an aluminium alloy, both the spatial characteristics of individual micro-discharges and their collective behaviour throughout the oxidation process are analyzed. The typical evolution of microdischarge is shown in Fig. 2.3 from which four consecutive stages of the PEO process can be distinguished. During stage I, intense gas evolution is clearly observed, along with some luminescence at the surface (Fig. 2.3(a)), which is eventually replaced by the onset of a bluish glow discharge around the sample. In stage II, the discharge tends to contract at the areas of the surface with maximum electric field intensity and appears, therefore, in the form of moving discrete white microdischarges (Fig. 2.3(b)), though a uniform glow background remains visible for some time. After about 10-12 min of treatment, the process gradually enters stage III, where the appearance of the microdischarges becomes more pronounced (Fig. 2.3(c)). Further PEO processing

makes some of the microdischarges yellow, larger and slower moving, which becomes a major feature of the process in stage IV (Fig. 2.3(d)).

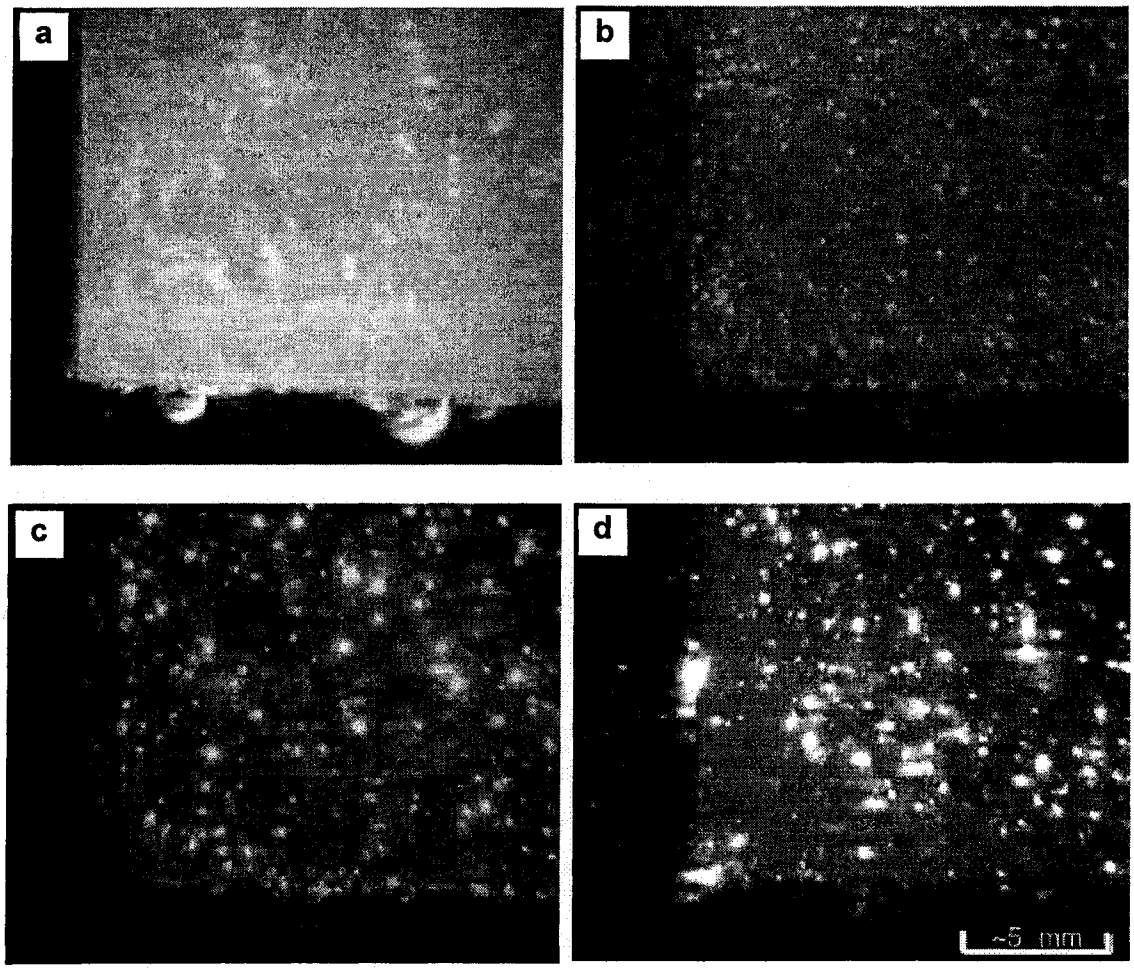

Fig. 2.3 Sample surface appearance at various stages of the coating formation process: (a) 0.5 min; (b) 10min; (c) 35min, and (d) 65min [51, 52].

2.4 Coating formation mechanism

2.4.1 Electrochemistry of plasma electrolytic oxidation (PEO)

With ionic current of the layer growth passing through oxide layer, there are two parallel processes for PEO coating growth: the electrochemical and the plasma chemical mechanisms [23].

The electrochemical formation of surface oxide layers can occur through different mechanisms. Unfortunately, there are few studies of the electrochemical formation of surface oxide layers in the electrolyte used for PEO such as aqueous solutions of inorganic polymers-silicates, aluminates, phosphates, etc. It has been proposed in early studies [53] that these layers are formed by the polycondensation of adsorbed anionic complexes of an electrolyte due to dehydration under the action of an electric field. Therefore, the processes associated with ionic diffusion can be ignored, so the coating composition can be formed only from the anionic complexes of an electrolyte when considering the electrochemical formation of oxides in such electrolytes.

In recent decade, several works [20, 23, 24] report on systematic investigation into the effects of process parameters on the growth kinetics and thermodynamics and associated changes in the structure, phase composition and mechanical properties of surface layers by the PEO treatment. However, existing data in the literature on the energy efficiency of PEO are quite controversial.

For revealing the basic electrochemical processes, a series of experiments on plasma electrolytic oxidation has been performed by A.L. Yerokhin et. al. In their early experiments [54], they attempted to develop a PEO process for deposition of aluminium titanate coatings on Ti. However, the process parameters chosen for that work (application of AC PEO mode and a complex aluminate-base electrolyte) allowed only qualitative consideration of current distribution (Fig. 2.4). According to the Fig. 2.4, oxide layer formation is induced both by the ionic component of the current which is transmitted via surface discharges and by the anodizing current passing across the surface which is free of discharges. Other components of the current cause secondary electrochemical processes which lead to liberation of electrode gases (e.g. H_2 and O_2),

accumulation of H_2O_2 in the electrolyte, anodic dissolution of the titanium metal and electrothermally induced metallurgical processes in the surface layer. The anodizing current is supported by electrolyte anions which (in alkaline aluminate solutions) are predominantly OH^- and AlO_2^-. Since the aluminate ions in particular are relatively unstable, they can in alkaline media partly interact with water and/or create complex anions between themselves, forming either mono- or poly-hydroxyanions, e.g. $Al(OH)_4^-$ or $Al_n(OH)_{4n+2}^{(n+2)-}$. On the surface of the Ti electrode, the above anions can take part in the following anodic processes [54]:

$$Ti^{4+}+2OH^-+2H_2O=TiO_2+2H_3O^+ \quad (2.1)$$

$$Ti^{4+}+4AlO_2=TiO_2+2Al_2O_3 \quad (2.2)$$

$$Ti^{4+}+4Al(OH)_4^-=TiO_2+Al_2O_3+2Al(OH)_3+5H_2O \quad (2.3)$$

In their subsequent works [24, 55], a quantitative evaluation of the rates of the major anodic processes is performed in a different approach, in which a simplified model situation should first be considered for the rate evaluation of partial processes during PEO. The experimental facility developed for this purpose comprises the following functions: (i) recording and analysis of the main electrical characteristics of the process, (ii) determination of the oxide layer thickness, (iii) anodic gas collection and composition analysis and (iv) electrolyte analysis to determine anodically dissolved metal. The experiments were performed on aluminium anodes oxidized in a model dilute alkaline solution (0.5 to 2 g l^{-1} KOH) under conditions of galvanostatic DC PEO, for which basic electrochemical processes were considered, such as oxide film growth, anodic dissolution and oxygen liberation. Four different stages of the PEO process were identified, characterized by various rate proportions of the partial anodic processes, i.e. (i) anodizing, (ii) anodizing with anodic dissolution, (iii) anodizing, dissolution and oxygen liberation

and (iv) plasma electrolysis (Fig. 2.5).

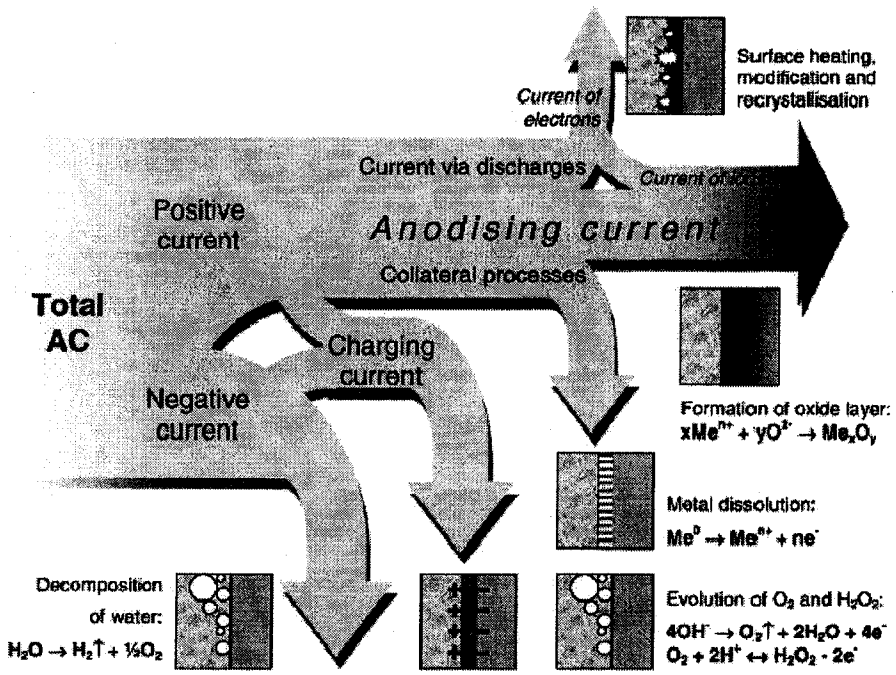

Fig. 2.4 Schematic diagram of current distribution during the PEO treatment of metals in AC mode [54].

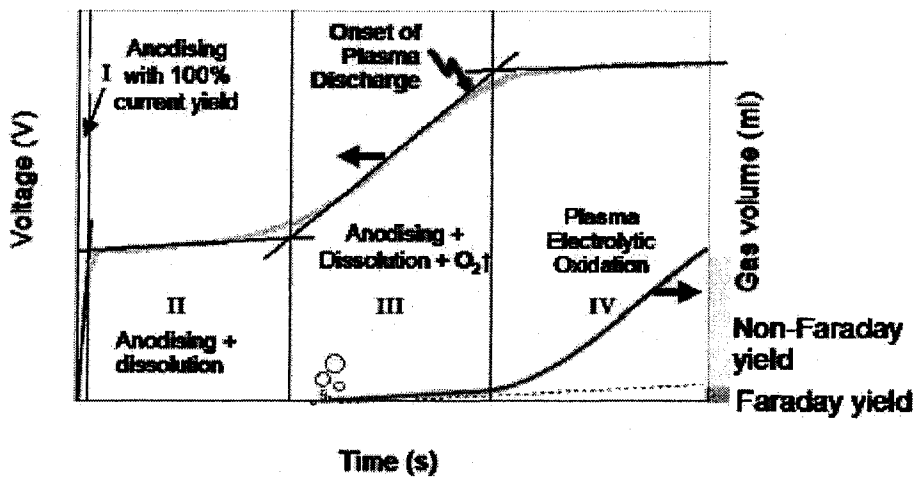

Fig. 2.5 Typical evolution of voltage and gas volume with time for galvanostatic DC PEO of Al in dilute KOH solutions [24].

Dynamic equilibrium of partial processes of oxide formation, dissolution and oxygen evolution is quite common of aluminum anodizing in alkaline solutions, where the following general reactions normally occur:

- Metal-oxide interface:

(i) anodic processes:

$$2Al + 3O^{2-}_{solid} \rightarrow Al_2O_3 + 6e^- \quad (2.4)$$

$$Al \rightarrow Al^{3+}_{solid} + 3e^- \quad (2.5)$$

- Oxide-electrolyte interface

(i) anodic process

$$4OH^- \rightarrow O_2 \uparrow + 2H_2O + 4e^- \quad (2.6)$$

(ii) alumina chemical dissolution and oxidation of ejected Al:

$$Al_2O_3 + 2(x-3)OH^- + 3H_2O \rightarrow 2[Al(OH)_x]^{n-}_{gel} \quad (2.7)$$

$$Al^{3+}_{ejected} + xOH^- \rightarrow [Al(OH)_x]^{n-}_{gel} \quad (2.8)$$

$$[Al(OH)_x]^{n-}_{gel} \rightarrow Al(OH)_3 \downarrow + (x-3)OH^- \quad (2.9)$$

The overall current efficiency of the oxide film formation was estimated to be in the 10 to 30% range (depending on the process conditions). It was also found that the film growth rate decreased significantly with increasing electrolyte concentration, since the rate of anodic dissolution increased. Oxygen evolution was shown to be the main electrochemical process at the potentials corresponding to the plasma stages of the electrolysis (oxygen current yields 60 to 80%). Estimations of the process efficiency were carried out, assuming that the partial processes of oxide film growth, dissolution and gas evolution on the surface are governed by the Faraday's law. The overall rate of oxygen

liberation at the anode exceeds the Faraday yield, which is probably due to the radiolytic effect of the plasma discharge on the adjacent electrolyte volume. The processes associated with this effect were considered and reaction routes leading to non-Faradic formation of gaseous products quantified, including (a) generation of free electrons with corresponding H_2O^+ vacancy formation, (b) quadratic recombination of the vacancies with the electrolyte anions and water molecules resulted in formation of free OH• radicals followed by (c) their annihilation due to either acceptor trapping or recombination processes, resulting in the formation of excessive gaseous products [24].

2.4.2 Plasma discharge models and plasma chemistry

Apart from the electrochemical, the plasma chemical processes were discussed [20, 23, 24, 53]. The plasma chemistry of the surface discharges is quite complex in nature, involving, on one hand, reactions between electrons, molecules of water and electrolyte anions and on the other, atoms and ions of the metal electrode. An important consequence of the occurrence of surface discharges is the development of metallurgical processes in the growing oxide layer, which are induced by the heat liberated in discharge channels from electron avalanches. Cycles of instantaneous local heating and cooling of the areas of the oxide layer in close proximity to a discharge channel lead to the melting, quenching and recrystallisation of the substances deposited onto the surface. As a result, decomposition of aluminium hydroxide to alumina, formation of complex compounds based on the Al-O system, as well as high-temperature transformations of alumina, can occur. The direction and intensity of these processes depend on the density and power of the discharges which are known to be defined by thickness of the oxide layer, so that the thicker the layer the less frequent yet more powerful and extended the discharges become.

In the plasma reaction, the key is the formation of microdischarge. Several microdischarge formation models have been proposed. For the first model [23, 56, 57], the microdischarges appear as a result of oxide film dielectric breakdown in a strong electric field (Fig. 2.6(a)). The breakdown is treated as a 'streamer propagation' due to the electron avalanche effects induced by film dopants and structural defects. Three main steps can be discerned in the breakdown process. In the first step, the discharge channel is formed in the oxide layer as a result of the loss of its dielectric stability in a region of elevated conductivity. This region is heated by generated electron avalanches up to temperatures of $\sim 10^4$ K. Due to the strong electric field (of the order of $\sim 10^6$ $V \cdot m^{-1}$), the anionic components of the electrolyte are drawn into the channel. Concurrently, owing to the high temperature, aluminium and alloying elements are melted out of the substrate and enter the channel. Thus, a plasma column (plasmoid) is formed as a result of these processes. In the second step, plasma chemical reactions take place in the channel. These lead to an increase in pressure inside the channel. So the plasmoid expands to balance it. At the same time, separation of oppositely charged ions occurs in the channel due to the presence of the electric field. The cations are ejected from the channel into the electrolyte by electrostatic forces. In the last step, the discharge cannel is cooled and the reaction products are deposited on to its walls.

The second group of models [51] considers each microdischarge as a gas discharge occurring in a micropore of the oxide film (Fig. 2.6(b)). The formation of a gas phase in the pore (and discharge ignition in it) is believed to be induced by an initial dielectric breakdown of a barrier layer in the bottom of the micropore.

An alternative model of microdischarge formation was proposed (Fig 2.6(c)) based on analogy with the contact glow discharge electrolysis originally studied by Hickling

and Ingram [58]. In their work, a glow discharge was observed at the interface of the electrolyte and a thin vapour sheath was formed at the surface of a platinum wire anode at $U^{+} \geq 420V$. In the case of an aluminium anode, however, the role of the vapour sheath is played by the gas bubbles accompanying the oxidation process and the discharge; therefore, it seems as if it is disintegrated into a number of microdischarges. Nevertheless, it is important to recognize that the common condition of discharge initiation in both cases appears to be electron emission from the electrolyte surface (partial cathode) into a gaseous phase, rather than dielectric breakdown of the growing oxide film. It should also be noted that free electrons might appear initially at the oxide-electrolyte interface in strong electric fields, regardless of the presence of any gas/vapour phase, due to the ionization of anions and molecules of water. The free electrons would then immediately participate in a series of reactions with water, resulting in the formation of gaseous products (H_2 and O_2), thus providing the necessary conditions for maintenance of a stable plasma discharge environment.

Another model worthy of consideration for AC PEO discharge is the dielectric barrier discharge, which has recently been reviewed by Wagner et al [59]. Similar to PEO, the barrier discharge operates under AC polarization and atmospheric pressure conditions, with one electrode covered by a thin dielectric film. The barrier discharge usually operates in a filamentary mode, for which the phenomenology is similar in appearance to a microdischarge in PEO, except that the barrier discharge occurs during both positive and negative half-cycles. Furthermore, unlike the discharge in PEO, dielectric barrier discharges cannot be produced using simple DC polarization.

A.L. Yerokhin et. al found that the above models do not fit the spatial, temporal and electrical characteristics of microdischarge phenomena which were observed in their

investigations [51-52]. A new model is suggested based on the analogy with contact glow discharge electrolysis. The model assumes the possibility of free electron generation and glow discharge ignition in the gaseous media at the oxide-electrolyte interface, which leads to heating, melting and quenching of the underlying oxide layer.

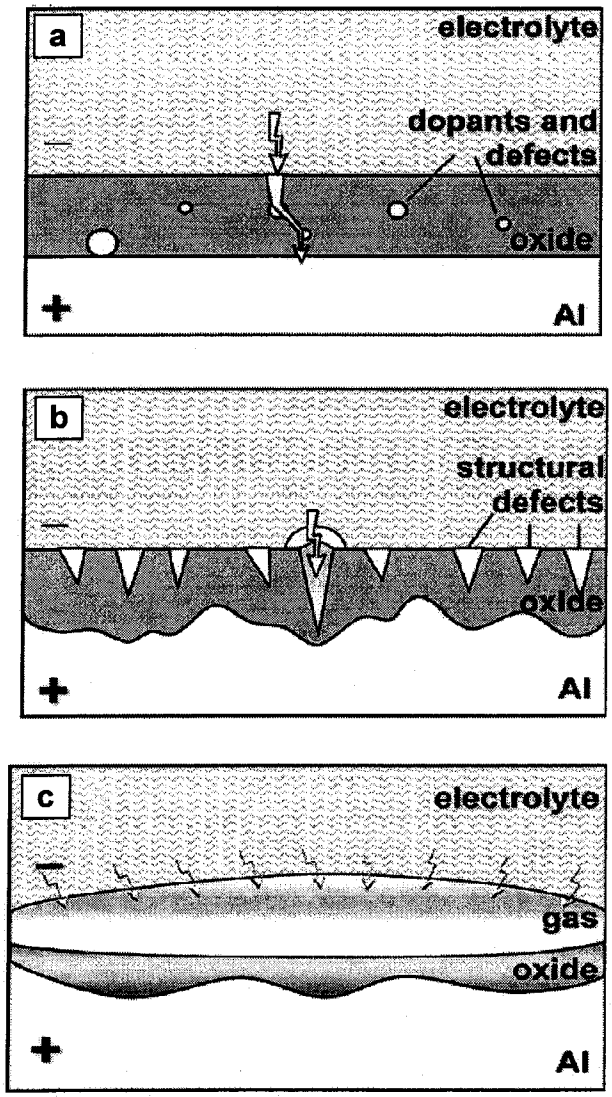

Fig. 2.6. Schematic illustration of models describing the appearance of surface discharge during anodic oxidation of Al: (a) model of the oxide film dielectric breakdown, (b) discharge-in-pore model and (c) model of contact glow discharge electrolysis adapted for the presence of an oxide film on the metal surface [51].

2.5 PEO coating structure

Fig. 2.7 illustrates the structure of the PEO coating [60]. SEM investigations demonstrate that alumina coatings, produced on Al alloys by the PEO technique, tend to consist of three layers, i.e. a porous outer layer, intermediate dense layer and thin inner dense layer. The porous outer region consists predominantly of the low temperature modification of Al_2O_3 (γ-Al_2O_3/η-Al_2O_3) and X-ray amorphous phases. A dense inner region is formed by mixture high temperature α, γ-Al_2O_3 modifications of Al_2O_3 and complex Al-X-O phases (X is the element from electrolytes), whereas complex phases of the substrate alloying elements are observed in a thin, interfacial region below the dense layer. The relative sizes of the regions, their structure and composition are substantially influenced by substrate composition, electrolyte composition and treatment regime. Comprehensive studies of these effects have been carried out for the treatment of Al-alloys in silicate solution [17, 50, 61]. In these studies, different treatment time, current density and concentrations of Na_2SiO_3 (2-20g/l) with addition of 2-3g/l of KOH solution were used to produce coatings with different ratios of Al_2O_3 and SiO_2 fractions. It has been observed that the increase of the silicon content in the electrolyte results in a higher growth rate by the formation of composite coatings and an extension of the inner dense layer. The relative proportion of the harder α-alumina is increased by raising the current density.

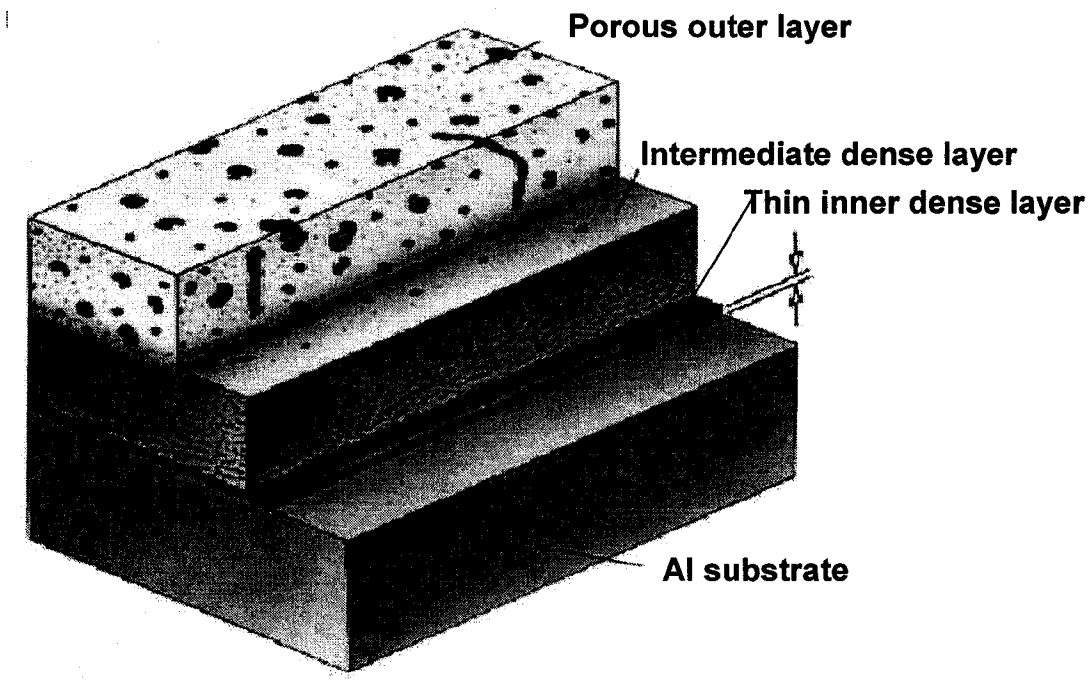

Fig. 2.7 Structure model of PEO coating [60].

X. Nie (2002) in reference 18 studied microstructure in the inner layer of the coating using cross-sectional TEM. Fig. 2.8 shows cross-sectional TEM images of a representative microstructure near the coating/substrate interface. The thin inner layer of the coatings exhibits a number of (predominately amorphous) sublayers, whilst the lower portion of the intermediate layer has a nanoscaled polycrystalline microstructure. Some occluded porosity of nanoscale dimensions was observed in the inner and intermediate layers, but not adjacent to the interface between the coating and the substrate. The characteristics of the coating near the interface with the Al-alloy substrate can be divided into three sublayers (1, 2 and 3 in Fig. 2.8(a)). Sublayer 1 shows a dense amorphous structure which has a thickness of ~140 nm constant over the entire sample, whereas the thickness of sublayer 2 varies, sublayer 2 shows a porous structure that is composed of amorphous and nanocrystalline regions with porosity of a size in the range of

approximately 10-100nm. Fig. 2.8(b) is an enlarged TEM image of the microstructure of sublayer 3. This layer was found to be composed of nanocrystalline structures whose grain size is in the range of 50-80nm. According to the TEM investigations, no porosity was observed at the interface between the substrate and the coating (sublayer 1) and the porosity in sublayer 2 was occluded, rather than interconnected.

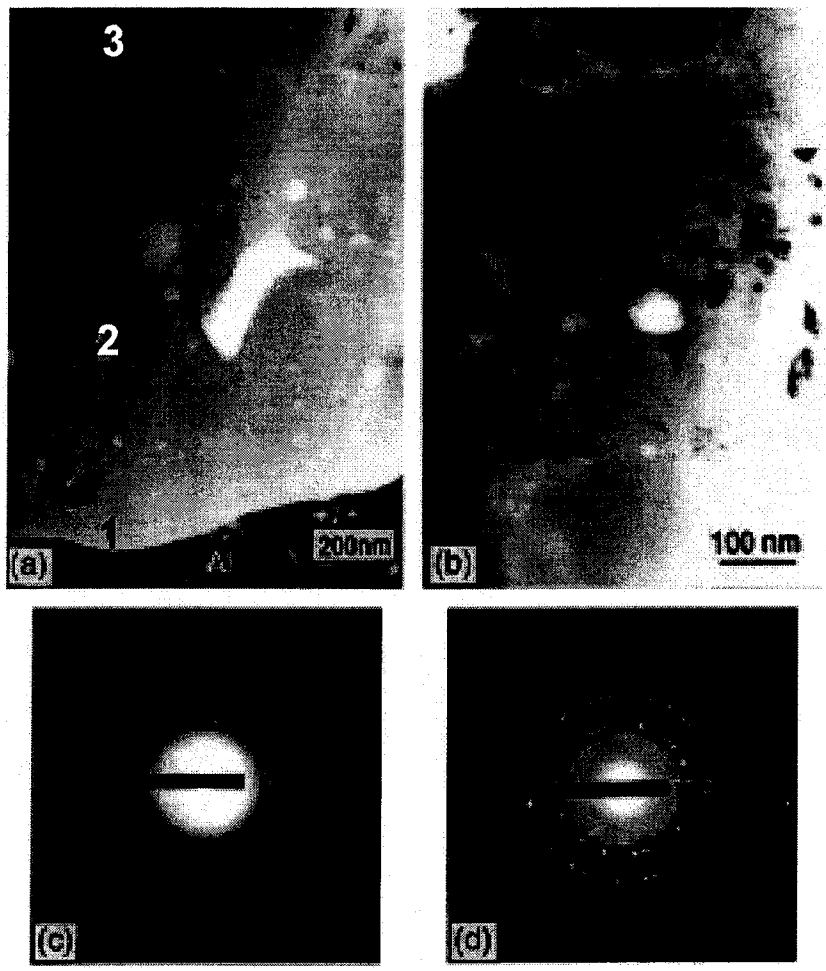

Fig. 2.8 Cross-section TEM images of (a) the inner layer near coating/substrate interface and (b) the intermediate layer, and SAED patterns taken from (c) sublayer 2 and (d) sublayer 3, respectively [18].

2.6 Properties of the PEO coatings

2.6.1 Coating mechanical properties

The PEO alumina (α-Al_2O_3/γ-Al_2O_3) coatings exhibit a high hardness. The formation of the Al-Si-O phase decreased Vickers hardness values (Indentation areas were on the order of 10^3-10^4 μm^2). However, when nanoindentation tests were performed (indentation areas were on the order of 10-10^2 μm^2), two characteristic values response to the indentation, representing two different phases. One phase had hardnesses between 18 and 25GPa, Young's moduli between 120 and 240 GPa. Another phase had hardnesses between 2 and 6 GPa, Young's moduli between 40 and 120 GPa. The relative number of indentations corresponding to the softer phase increased with the increase of the Si content in the coating [17]. Cross-sectional hardness is relative with the total coating thickness and dense (inner) layer thickness. The position of the maximum hardness (up to 2400HV) moved away from the interface with increasing coating thickness [62].

The effective adhesion of the oxide layer, as evaluated by microindentation tests, trends to increase with coating thickness. In 200 to 250 μm thick coatings the adhesion strength can reach 350 to 380 GPa, i.e., comparable to the tensile limit of the substrate in case of aluminum [50]. One explanation of the adhesion increase lies in a structural change in the coating's inner region due to diffusion processes. It is also likely that a thicker coating gives better load support, and that the interfacial region is, therefore, less stresses under the applied load [50, 62].

2.6.2 Corrosion resistance

The corrosion resistance of the PEO coatings on aluminum alloys was studied by X. Nie and coworkers [18]. Fig. 2.9 shows the polarization curves of the alumina coated alloy (with coating thickness of 250μm) and the untreated Al alloy substrate. Both types of sample were immersed in 0.5M NaCl solution for 1h, 1day and 2 days before corrosion tests. A stainless steel AISI 316L sample was also used in the corrosion test for comparison. The poor corrosion protection property of the uncoated Al substrate resulted from the fact that the corrosion resistance considerably decreased after the thin protective oxide film on the uncoated aluminium substrate surface was broken down by the corrosion processes. The PEO-coated Al alloys possessed excellent corrosion resistance in the solution-considerably better even than the stainless steel. The dense, amorphous sublayer 1 and the predominately amorphous sublayer 2 in the inner layer described in section 2.5 (Fig. 2.8) may serve as diffusion barriers to enhance the corrosion resistance and may in part explain the excellent anti-corrosion performance exhibited in the above corrosion test.

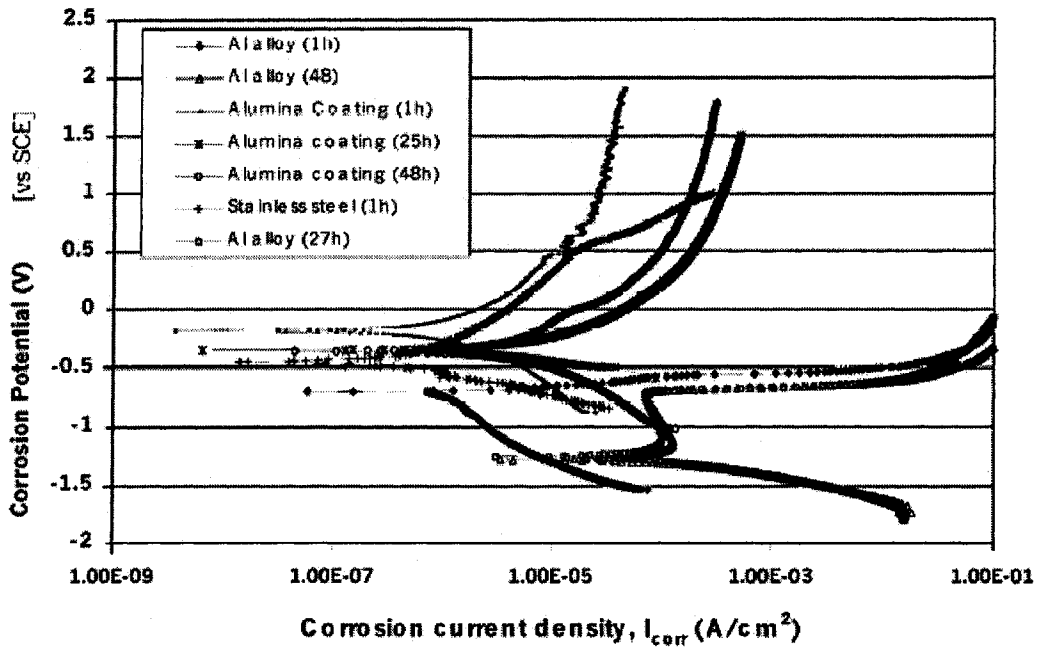

Fig. 2.9 Potentiodynamic polarization curves of untreated substrate materials and PEO alumina coatings in 0.5M NaCl solution after different immersion times [18].

2.6.3 Tribological properties of PEO coatings

The PEO technology can produce superhard and thick ceramic coatings which generally have excellent load-support characteristics. Thus, its tribological applications have attracted a lot of attention. Several studies have been reported on the tribological properties of the PEO coatings.

In reference 17, the tribological properties of the coatings produced by different current density and electrolyte concentrations were investigated in ball-on-disk sliding tests against 440C steel and sapphire balls. Tests were performed in air with relative humidity (RH) controlled in the range from 5-90% RH, and in vacuum of 10^{-3} Pa. Wear resistant properties of PEO coatings were estimated in ring-on-block sliding tests. Tests were run in an ambient environment with about 30-40% RH, sliding speed of 0.2m/s, and

load of 980N to provide contact pressures about 1GPa. Weight losses of friction pairs after 5000 ring revolutions were measured with microbalance to calculate mg/rev. wear rates. The results of above tests showed that friction of Al-Si-O composite coatings appeared to depend on the coating stoichiometry, counterpart material, relative humidity, and the formation of the transfer film. The lowest friction coefficient was found for the $Al_{0.26}Si_{0.08}O_{0.66}$ coating in sliding against itself and a sapphire ball, and varied from 0.15 to 0.25 depending on RH. The application of the $Al_{0.26}Si_{0.08}O_{0.66}$ coating to a block-on-ring friction pair manufactured from an Al-based alloy reduced friction from 0.65 to 0.17, decreased wear rate by four orders of magnitude, and prevented micro-cutting and/or adhesive wear of the friction pair at contact loads of 1GPa.

X. Nie (1999 in ref. 62) reported the effect of coating thickness on the tribological properties. The properties of the coatings with thickness from 100μm to 250μm were tested using a "ball-on-plate" reciprocating-sliding test with a load of 10N over 5000 cycles, at a frequency of 2Hz. The length of sliding path was 10mm with temperature and humidity controlled to 23±1°C and 50±5%. The friction coefficients of the PEO coating against bearing steel (BS) and tungsten carbide (WC) balls lay in the ranges 0.64-0.68 and 0.68-0.86, respectively, which is higher than the steady-state values for the untreated substrate, however the coatings all had excellent wear resistance. The dry wear rates were in the range 10^{-8}-$10^{-9}$$mm^3$/Nm, which compares favourably with the untreated alloy substrate at ~$10^{-4}$$mm^3$/Nm. It was found that the PEO coatings of intermediate thickness (150μm) showed relatively poor wear resistance relative to their thicker and thinner counterparts. In addition, for the intermediate thickness samples the wear rate against the BS counterface was larger than that against WC. The reason may be that the wear

mechanism changed from adhesive and fatigue wear to abrasive wear as well as adhesive and fatigue.

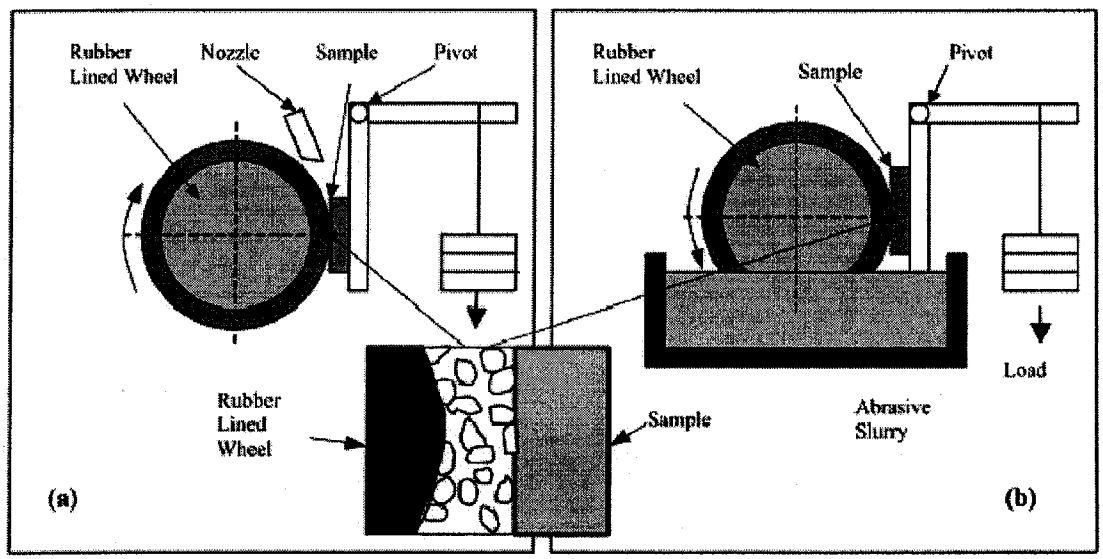

Fig. 2.10 Schematic of (a) dry and (b) wet rubber wheel abrasive wear tests [18].

In Ref. 18, dry and wet rubber wheel abrasive tests (Fig. 2.10) were carried out with dry silica sand with a size of ~50μm or wet slurry for the PEO-coated Al alloy samples. The results indicated that the PEO coated aluminium alloy samples possessed a much higher abrasive wear resistance than the uncoated aluminium alloy.

The coated aluminium alloy exhibited abrasive wear resistance which was nearly an order of magnitude lower than the untreated substrate, and approximately five times lower than that of the stainless steel. In comparing abrasion performance of the coated samples with thicknesses 150μm and 250μm, the weight loss of the 'thick' coating in the first 1000 revolutions was found to be larger than that of the 'thin' one due to the thicker porous top layer. A similar dry-sand rubber-wheel abrasive wear test, a solid-particle erosive wear test (ASTM G76-83) and a pin-on-disc sliding wear test (ASTM G99) were conducted in Ref. 63. The PEO coating in the study exhibited excellent performance

under abrasion and sliding wear modes in comparison with detonation spray Al_2O_3 coating and uncoated Al substrate.

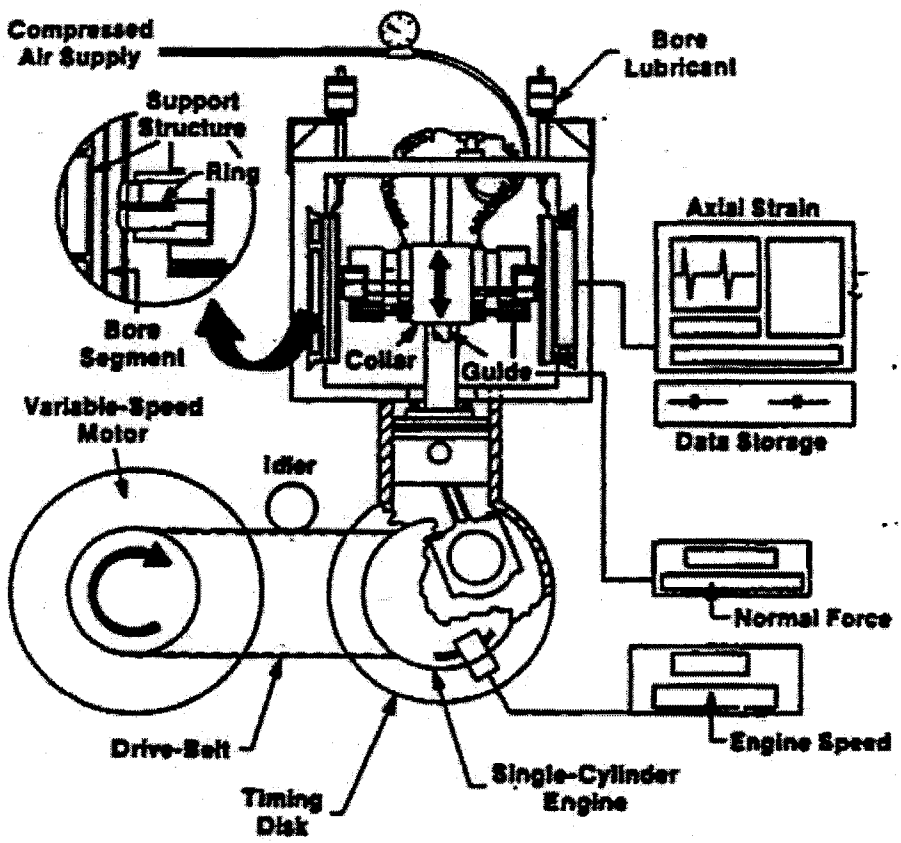

Fig. 2.11 Segmented Ring/Bore Liner test rig is an apparatus for accurate and direct comparative friction measurements between cast iron and coated bore and ring samples and oil viscosity at speeds from 100 to 600rpm [64].

In Ref. 64, PEO were applied in SAE 6061 aluminum alloy cylinder liners of a 4.6L-V8 aluminum block engine. The coating surface was honed and material removal during honing to obtain finished bore diameter specified. Friction properties of the PEO coatings along with a production engine cast-iron liner were evaluated in a cylinder bore/piston ring test rig (Fig. 2.11) capable of testing cast iron and the PEO specimens simultaneously under low speed-maximum load engine operating condition which

represents the most severe boundary friction condition that the cylinder bores are subjected to. PEO coatings yielded much lower friction than the cast-iron liner, and with high density PEO coatings, much lower wear. There are, however, attributable to smoother finish.

Although the PEO coatings have excellent wear resistance, for sliding wear applications, such alumina coating often exhibit relatively high friction coefficients against many counterface materials. Thus, there are also many prospects for the improvement of the PEO coatings with low friction and high counterface compatibility.

X. Nie, et. al (2000) in Ref. 21 investigated a duplex treatment, combining a load-supporting PEO alumina layer with a low friction diamond-like carbon (DLC) coating, produced by a modified plasma-immersion ion implantation (PI^3) process. The DLC-coated samples provided a low and stable friction coefficient (<0.2). An intermediate alumina layer is obviously beneficial in providing the load support essential to withstanding sliding wear at high contact loads and can also be beneficial in controlling impact wear damage.

X. Nie, et. al (2004) in Ref. 65 produce oxide/graphite composite coating. The graphite embedded into the porous outer layer of the PEO coating during the PEO treatment, which resulted in a low friction (~0.22) and exhibited good compatibility with the steel counterface during dry tribological testing.

2.7 Some challenges on PEO coatings

Plasma electrolytic oxidation (PEO) is a cost-effective and environment friendly process, which can be used to improve the wear resistance of aluminium alloy parts by

creating a hard, thick alumina coating on the component surface. However, there are still some challenges on the way to component applications.

Firstly, in most of previous works, 2xxx and 6xxx series, i.e., low silicon (<1.5% Si) content Al alloys were applied to produce thick oxide coating (i.e., >100 μm in thickness). Due to the rapid growth in applications of high silicon cast Al-Si alloys, the applications of PEO on the cast Al-Si alloys have been paid more attention since recently.

The study in Ref. 66 investigated the EPO coating formation on hypoeutectic Al-Si alloys (6.5-7.5% Si) and showed that silicon particles in the hypoeutectic Al-Si alloy substrate were able to be oxidized and mixed into the coating and silicon element in the Al-Si alloy had enhanced formation of a mullite coating. However, to our knowledge a detailed and systematic investigation of the effects of silicon content in Al-Si alloys on the PEO coating formation and morphology has not been reported yet.

Secondly, previous PEO processes were carried out at much higher voltages (normally over 600V) for longer duration (from several tens minutes to several hours) and therefore higher energy input. The porous outer layer made the as-deposited coating surface very rough and post-machining is necessary for industry application. Thus, the current PEO technology is not economically viable for applications of cost-sensitive component such as automotive parts.

Finally, although the PEO coating have excellent wear resistance, the hard ceramic coatings tend to hurt the counterface material during the sliding wear, due to hard ceramic phase in the wear interface. Therefore, severe abrasive wear and high friction coefficient occur during the sliding wear.

Therefore, a systematic investigation of the PEO coatings on high Si content Al-Si alloy (Si>7%) is needed. Development of a novel PEO coating which not only have low friction and high wear resistance but also good compatibility with most of counterface materials has been maintained as a challenge.

2.8 Summary of the review and objectives of the thesis

Plasma electrolytic oxidation (PEO) of metals is a complex process combining concurrent partial processes of oxide film formation, dissolution and dielectric breakdown. The probability of dominance for any of these partial processes in the overall process depends on the nature of both the metal and the electrolyte, as well as on the current regime employed. The ultimate stage of the PEO treatment is a quasi-stationary stage of persistent anodic microdischarges, which exhibit a progressive change in characteristics during the electrolysis. At high discharge temperatures and pressures (reaching about 2×10^3 to 3×10^3 °C and ~10^2 MPa, respectively), solid products of electrolysis and adsorbed gel layers are deposited on the metal surface in the form of high-temperature oxide phases or glassy ceramic coatings. The electrolysis is always accompanied by intensive gas evolution and localised metal evaporation due to the plasma thermochemical reactions in the microdischarges [24].

Four different stages of the PEO process have been identified, characterised by various formation mechanisms: (i) anodizing, (ii) anodizing film melted and broken down, (iii) micro-arc discharge and oxide coating formation, and (iv) coating composition fused and re-crystallized.

The PEO coating has a three layers structure, i.e., porous outer layer, dense layer and very thin inner dense layer.

The PEO coatings are very hard ceramic coatings with good wear resistance and adhesion. Thus, its tribological applications have attracted a lot of attentions, especially the application on Al-Si alloy components. But the high energy input, long treatment duration and post-machining make it not economical for many industrial applications. Moreover, the high friction and poor compatibility with most metal counterface limit the application span of these ceramic coatings. Therefore, a systematic investigation of PEO process on Al-Si alloys and development of a composite coating of a low friction with good counterface compatibility are the main objectives of this project.

CHAPTER 3 EXPERIMENTAL DETAIL

In this chapter, the experimental procedures are described. There are three main parts of experiments in this project.

3.1 Part A -Effect of Si contents in substrate materials on the PEO coatings

In this part of work, in order to best understand the growth mechanisms of the PEO coating on the Si phase regions in the substrate, the coatings on two Al-Si alloys are examined with special attention focussed on the effect of different Si contents in the aluminium alloys on the coating formation and properties.

3.1.1 Preparation of substrates

Two kinds of Al-Si alloys, i.e., hypoeutectic Al-Si alloy 319 (~7% Si) and hypereutectic Al 390 alloys (~17% Si) were chosen as substrate materials. The compositions of these two alloys are presented in Table 3.1.

Table 3.1 Nominal compositions of the Al-Si alloys

Alloys	Composition, wt%						
	Si	Fe	Cu	Mg	Mn	Other	Al
Hypoeutectic alloy 319	5.5-7.5	1	3-4	0.1	0.5	0.35 Ni, 1 Zn	The balance
Hypereutectic alloy 390	16-18	1.3	4.5	0.45-0.65	0.5	1.5 Zn	

A number of square coupons (25×25×5 mm^3) were cut from commercial cast Al-Si alloys (Al 319 and Al 390 alloys). All the coupons were polished to obtain a similar

surface roughness of 0.1±0.02 μm then degreased with solvent, flushed and cleaned with distilled water, finally dried by hot air.

3.1.2 Preparation of coatings

The treatment unit for PEO in this project consists of an electrolyser and a high power electrical source. A DC power supply (Magna Rack mount DC power supplies SQD500-26) (Fig. 3.1) has been used. The maximum output voltage used for this part of experiment is 500V. The electrolyser is a glass bath with a stainless steel frame inside which also serves as the counter-electrode. The schematic of treatment cell for the PEO coating preparations is shown in Fig. 3.2.

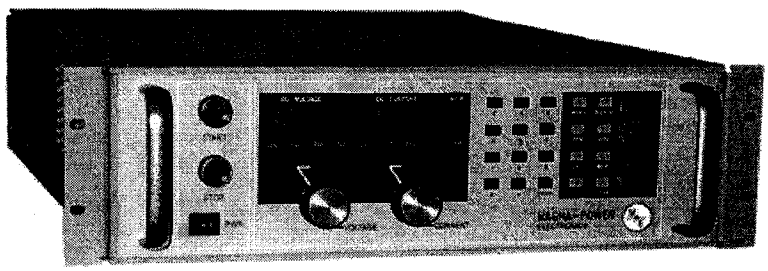

Fig 3.1 Magna Rack mount DC power supply SQD500-26 used for the PEO process

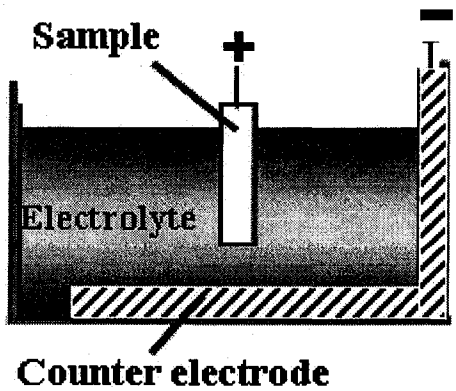

Fig 3.2 Schematic of the PEO treatment unit

To distinguish the individual process stages clearly with a wide investigation window, low current density (0.05 A/cm^2) and electrolyte concentration were selected to slow down the coating formation process. An alkali-silicate solution (4 g/l Na_2SiO_3 and 0.4g/l KOH) was used as an electrolyte. A constant current density of 0.05 A/cm^2 was set during the coating process, and the voltage increased gradually with process time so as to maintain the preset current density as the coating thickness gradually increased. Voltage variation vs. treatment time was recorded for both the Al 319 and Al 390 alloys. All samples for each of the alloys were treated and the treatments were stopped at certain voltages. The treated samples were taken out from electrolyte, then flushed by distilled water and dried by hot air, finally ready to subsequent tests.

3.1.3 Characteristics of coating formation process and coating property tests

(i) Metallurgical analyses of the Al-Si alloy substrates

An optical digital image analyzer (Buehler Optical Microscope, max 1000 times) with an image analysis software (Fig. 3.3) was used to carry out the metallographic observation of Al alloy substrates.

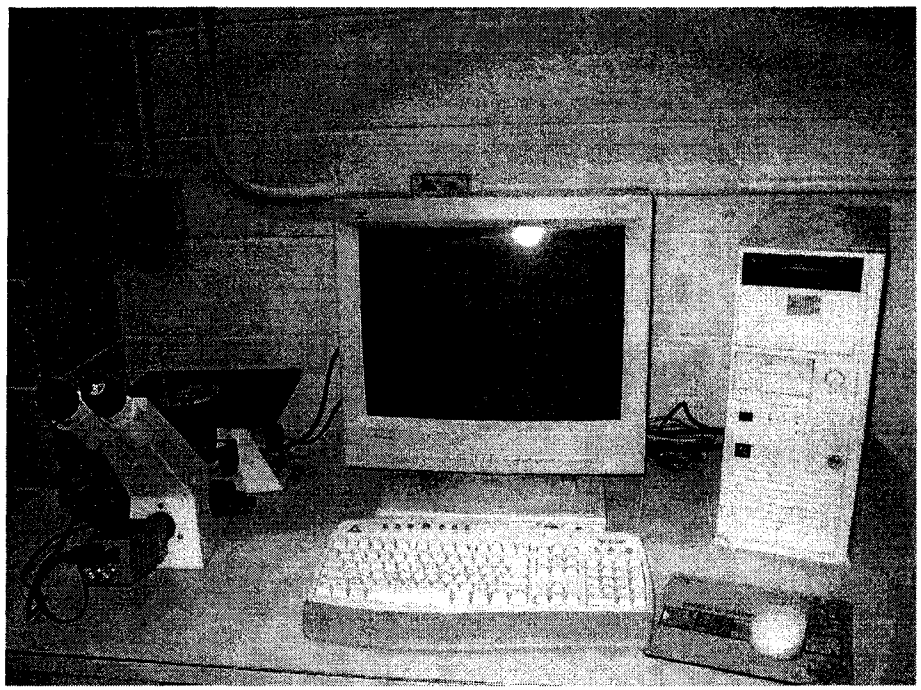

Fig. 3.3 Buehler optical microscope

(ii) Coating morphology and composition characterization

A JEOL Scanning Electron Microscope (SEM) with Kevex 5100C energy dispersive X-ray analysis (EDX) (Figure 3.4) was employed for study on the coating surface morphology and composition. SEM was operated at an accelerating voltage 15KV.

The cross-sectional morphology of the coatings treated to the 500V on both Al alloys was also studied by SEM observation. Before examination of the cross-sections, the cross-sectional samples were mounted with resin and polished first with a SiC abrasive paper of gradually decreasing grit size, then with an alumina suspension for the final polishing. Because of low electrical conductivity of the oxide coatings, the samples were sputter-coated with gold prior to SEM examination.

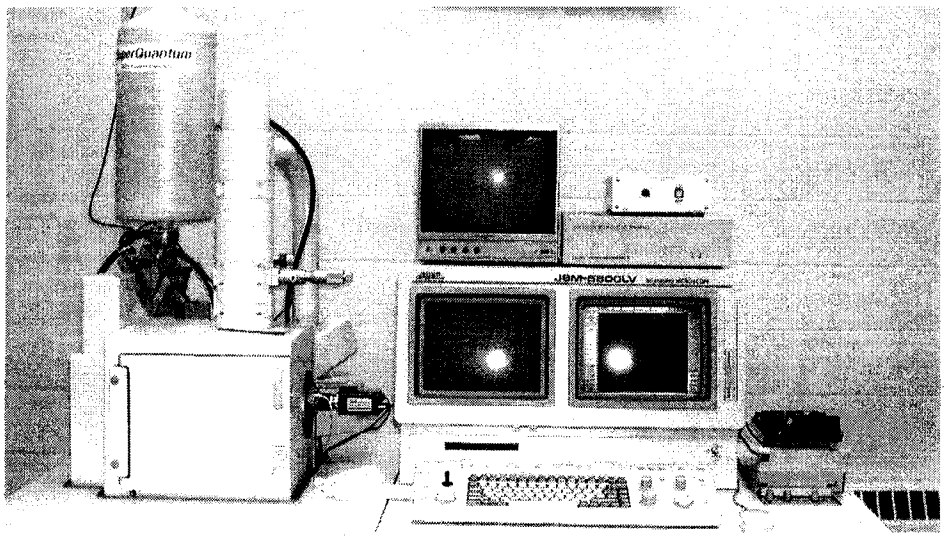

Fig. 3.4 A JEOL Scanning Electron Microscope (SEM) with Kevex 5100C energy dispersive X-ray analysis (EDX)

(iii) Surface roughness

Mitutoyo SJ-201P surface roughness tester (Fig. 3.5(a)) with a data acquisition system (Fig. 3.5(b)) equipped with SJ201 Serial Communication Ver. 2.20 software was used for surface roughness (Ra) measurements.

(iv) Phase identification of the coatings

The phase structures of the coatings were investigated using a Siemens D5000 X-ray diffractometer (Cu K_a radiation) (Fig. 3.6) with a glancing angle attachment. A glancing angle of 2° was used for the study in this section.

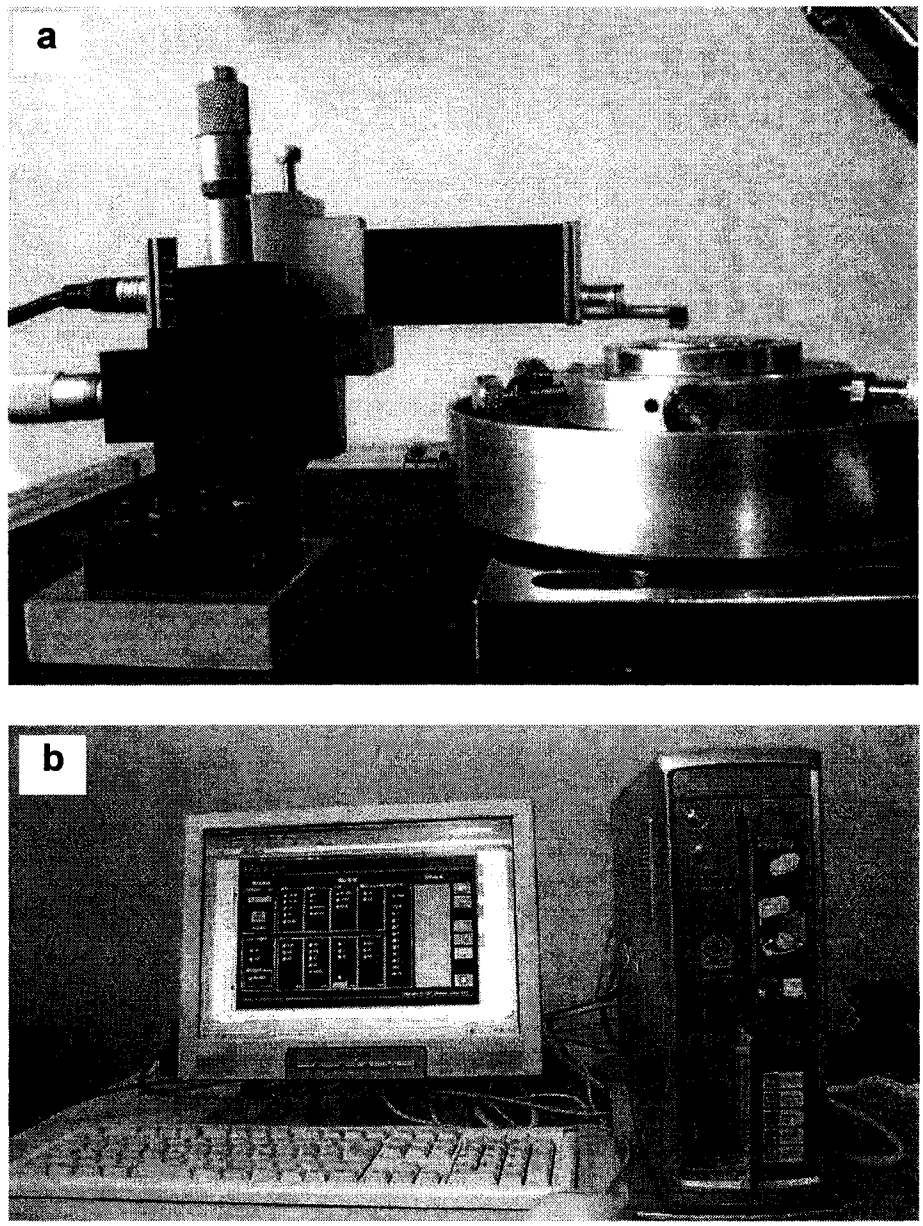

Fig. 3.5 Mitutoyo SJ-201P surface profilometer. (a) Surface roughness tester and (b) the data acquisition system

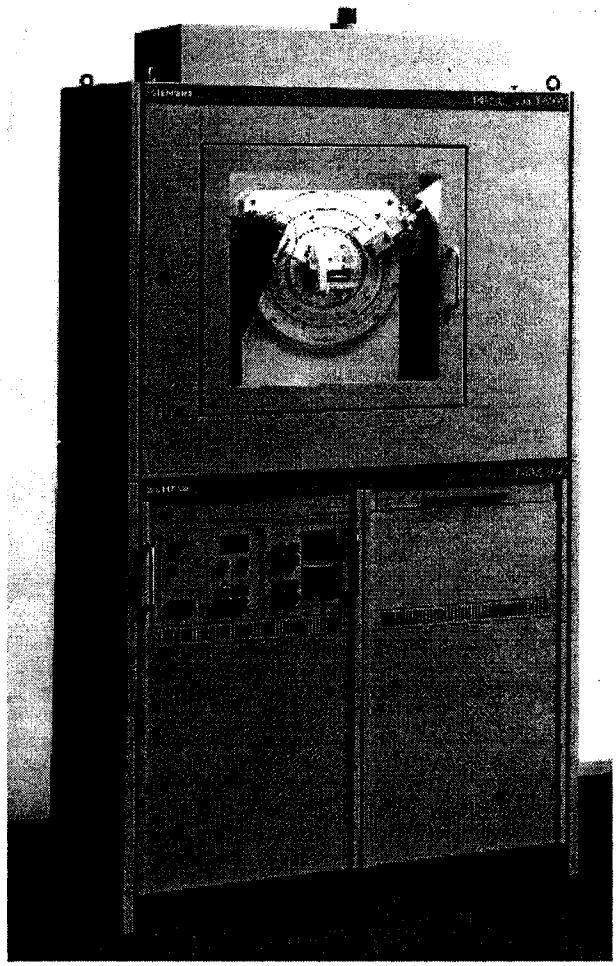

Fig. 3.6 Siemens D5000 X-ray diffractometer

3.2 Part B-Effect of electrical and electrolytic parameters on the PEO coatings

As described in Chapter 2, the previous study on the PEO coatings is mainly on low Si content (<1.5% Si) Al alloy (2xxx and 6xxx alloys) and the thickness of these coatings are usually over 100μm. In this part of experiment, a systematic investigation into the PEO coatings with thickness less than 30 μm on high Si content Al-Si alloy (~7% Si) were performed.

3.2.1 Coating formation process

A number of Al 319 square coupons (25×25×5 mm^3) were prepared as the description in the section 3.1.1. Two alkali-silicate solutions (4g/l Na_2SiO_3 with 0.4g/l KOH and 8 g/l Na_2SiO_3 with 0.8g/l KOH) and three constant current densities of 0.05 A/cm^2, 0.1A/cm^2 and 0.2A/cm^2 were adjusted to deposit the PEO coatings using the treatment unit in section 3.1.2. Samples treated by different electrolytic and electrical parameters are listed in Table 3.2.

Table 3.2 Samples treated with various process parameters

Samples code	Process parameters	
	Electrolyte concentration (g/l)	Current density (A/cm^2)
A11	4	0.05
A12	4	0.1
A13	4	0.2
A21	8	0.05
A22	8	0.1
A23	8	0.2

Constant current mode was used during the process. With the treatment time, the voltage firstly increased to maximum value 500V. Then, the voltage being constant, the current was decreasing due to the coating thickness growing. When the current density declined to 0.003A/cm^2 the treatment was stopped. The voltage and current density variation are recorded during the PEO treatment processes. After cleaned and dried, PEO-treated samples were ready to be measured and analysed.

3.2.2 Characteristics of coating formation process and coating property tests

(i) Surface morphology

The JEOL Scanning Electron Microscope (SEM) used for section 3.1.3 was also used to observe surface morphology of the coatings deposited by the various treatment parameters described as above. The surface roughness (R_a) was measured using the Mitutoyo SJ-201P surface profilometer (Fig. 3.5). The average size of surface oxide projections was estimated by determining the average length of peaks in profile plots. Fig.3.7 illustrates this method. Fig. 3.7(a) is the schematic of detector unit of surface profilometer. During the test, the stylus slides on the workpiece surface and the travel length is 3mm. Five travels were randomly taken on each sample. Fig. 3.7 (b) shows a profile plot obtained by intersecting a surface with a plane normal to the nominal surface. It is a representation of the real profile (a profile of the real surface) obtained by a surface roughness measuring instrument. The mean line (X axle in Fig. 3.7(b)) may be calculated to the position shifted from the position where it is supposed to be for surface roughness evaluation. In the profile plot, the peaks and valleys are correspond to projections and pores on the real coating surface as shown in SEM micrograph Fig. 3.7(c). The following equation is used to estimate the average size of oxide projections.

$$D_{Average} = \frac{1}{n}\sum_{i=1}^{n} D_i \qquad (3.1)$$

Where, $D_{Average}$ - the average size of oxide projection;

D_i- the single projection length in sliding way.

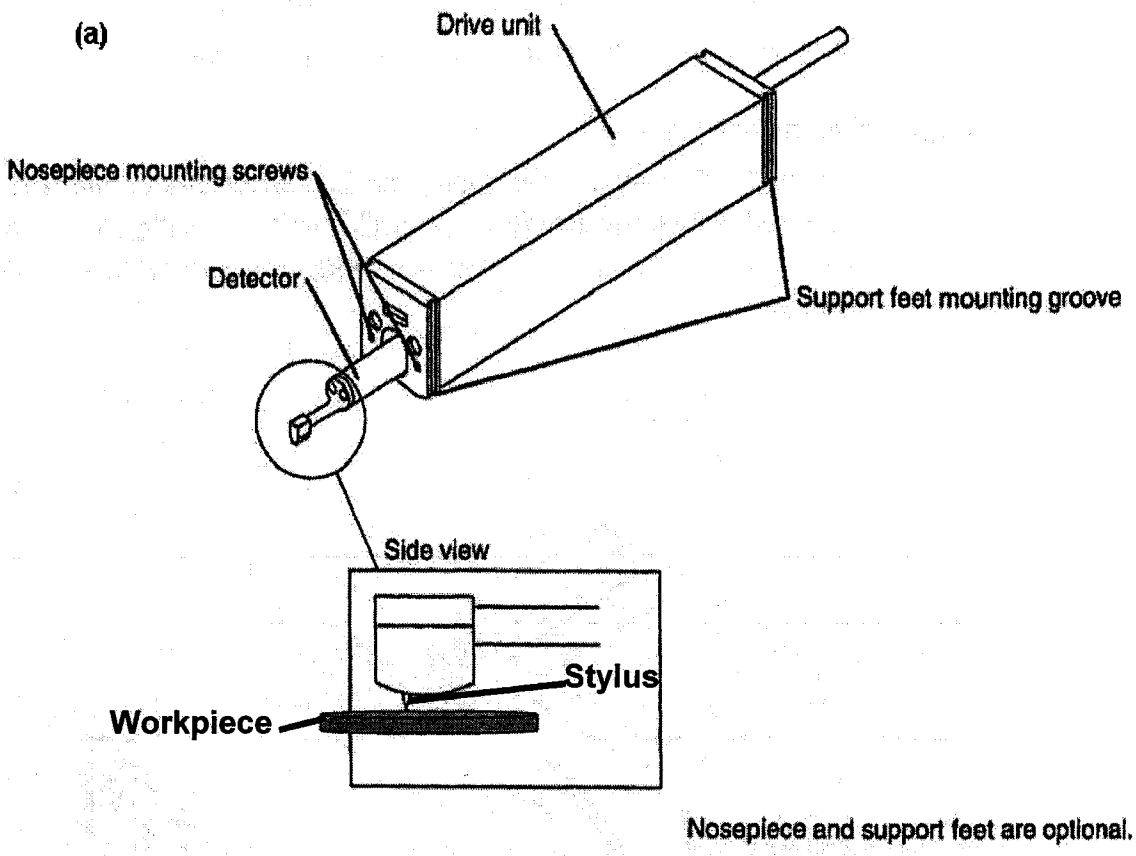

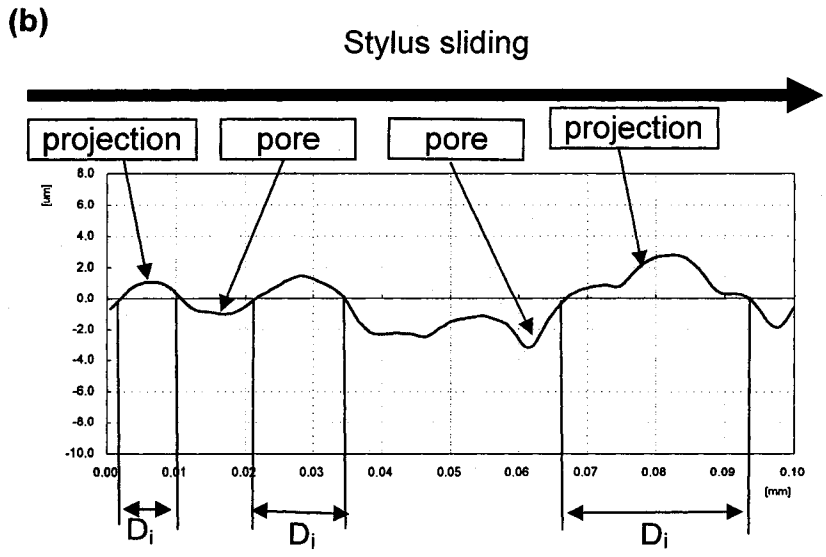

Fig. 3.7(a, b)

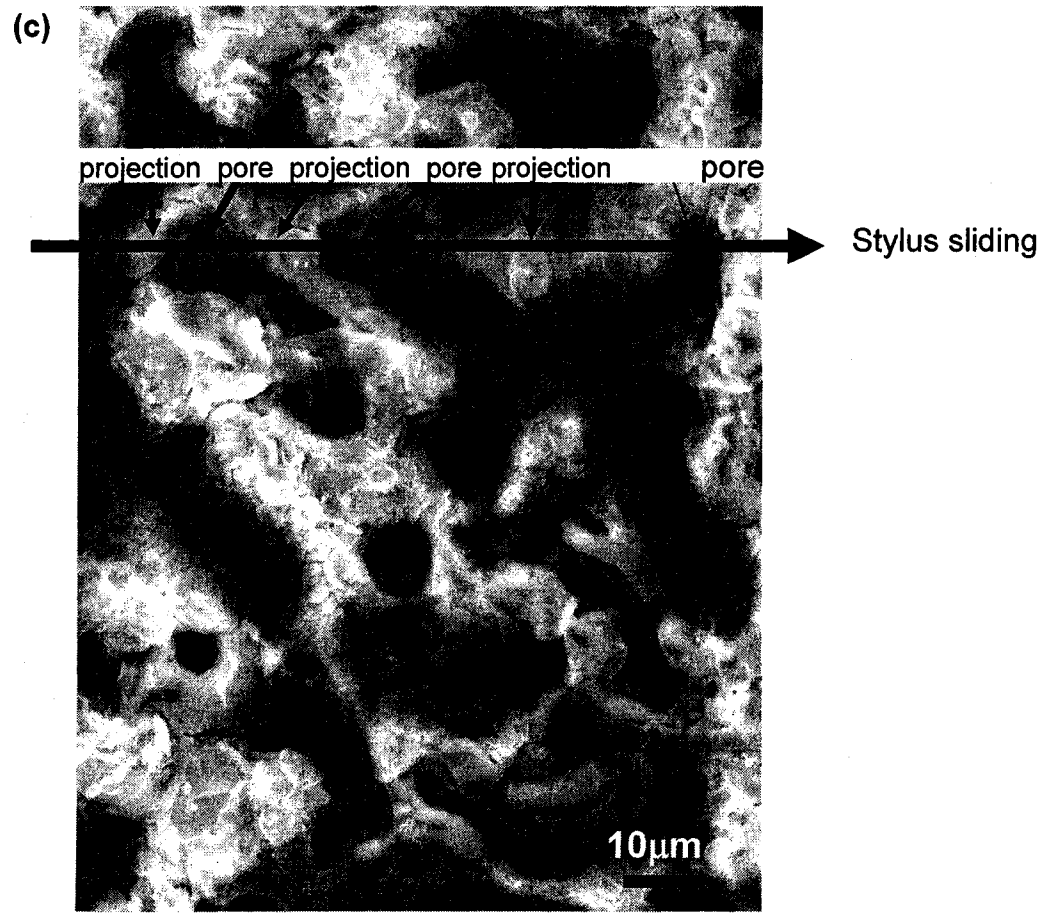

Fig. 3.7 Illustration of estimating the size of oxide projections on coating surface by profile plots. (a) The schematic of detector unit of surface profilometer, (b) a surface profile plot, and (c) an SEM micrograph showing the coating surface morphology.

(ii) Coating structure

The coating structure was studied by SEM observation of sample cross-section. The thicknesses of coatings and individual layers of coatings also were determined by cross-section investigation. The preparation of cross-sectional samples was described in section 3.1.3

(iii) Microhardness

A Buehler hardness tester (Figure 3.8) was utilized to measure Vickers hardness values of the coatings under 10g normal load.

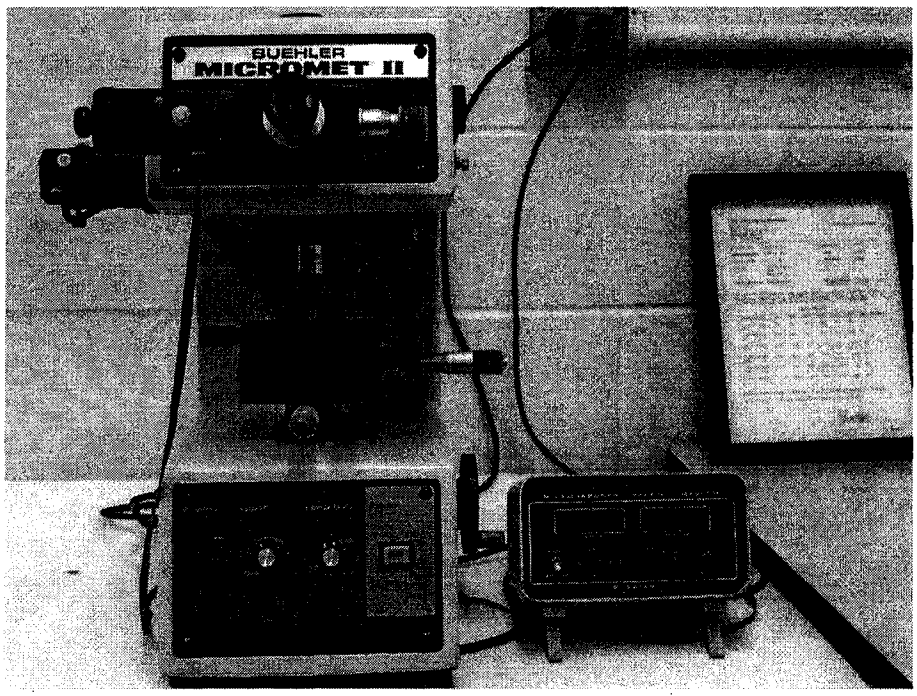

Fig. 3.8 Buehler microhardness tester

(iv)Phase structure of coatings

The phase structures of coatings were investigated using a Rigaku D/max 1200 XRD (Cu K_α) with scans acquired from 20° to 100° (in 2θ°). The XRD patterns were used to determine the phase structures.

3.3 Part C -Oxide-graphite composite coatings

Oxide coatings by using PEO have excellent wear resistance but poor compatibility with most of wear counterface. In this experiment section, we intend to produce oxide-graphite composite coatings to produce low friction and high wear resistance coating on an Al-Si alloy by using the PEO method in the selected aqueous silicate-based electrolytes.

3.3.1 Deposition process of oxide-graphite composite coatings

Cast Al-Si alloys 319 were used as sample substrates (rectangular coupons: 25×25×5 mm^3). The sample preparation procedure is similar to that of in section 3.1.1. The DC power source provided a constant current density 0.1A/cm^2 and maximium voltage of 500V.

Fig. 3.9 shows the schematic of treatment procedure of composite coatings. Firstly, two groups of oxide coatings were deposited in two electrolytes (4g/l $NaSiO_3$ with 0.4g/l KOH and 8g/l $NaSiO_3$ with 0.8g/l KOH in distilled water separately). The electrolyte temperature was controlled to remain lower than 60°C. When the applied voltage reached 480V, graphite was rubbed on these two group oxide layers, and then the samples were treated by the PEO process for around 1 minute. This process was repeated for 10-15 times, while the voltage gradually increased to 500V. The process parameters of the coating preparations were listed in Table 3.3.

Table 3.3 Process parameters of oxide and oxide-graphite composite coatings

Sample code	Process parameters		
	Electrolyte concentration (g/l)	Current density (A/cm^2)	Graphite rubbing
A12	4	0.1	-
A22	8	0.1	-
AG12	4	0.1	10-15 times
AG22	8	0.1	10-15 times

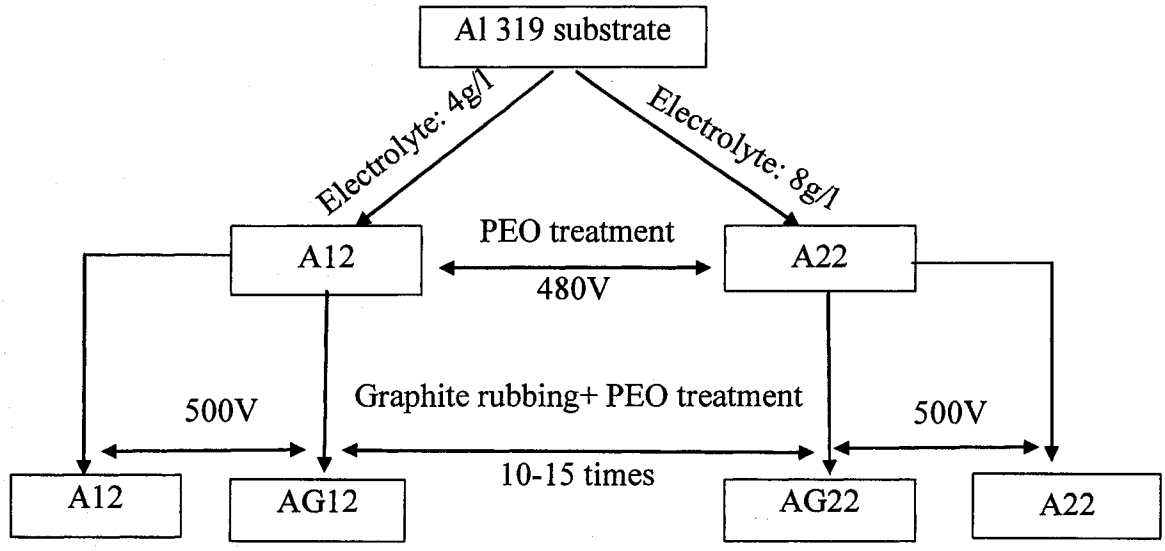

Fig.3.9 Schematic of treatment process of composite coatings.

3.3.2 Coating characterization and coating property tests

(i) The surface and cross-section of the oxide-graphite composite coatings

Scanning Electron Microscope (SEM) with energy dispersive X-ray analysis system (EDX) was employed for study surface morphology, coating composition and coatings thickness by cross-section investigation.

(ii) Roughness and microhardness

Roughness measurement and microhardness tests were performed using the instruments as the description in section 3.2.2.

(iii) Tribological properties

The tribological properties were tested by use of pin-on-disc tribometer (Sciland Pin/Disk Tribometer PCD-300A shown in Fig. 3.10) under dry and lube test conditions. Tribological tests on the uncoated, PEO oxide-coated, and oxide-graphite composite-coated Al alloy substrates were performed under room temperature (20 °C), ~50% humidity, a 1N normal load, 0.1m/s sliding speed with bearing steel balls (5.5mm in

diameter) as the counterface materials. Before the tests, all sample surfaces were slightly polished to have a similar surface roughness (2±0.2μm). During the wet tribological test, small amount of 3W10-30 engine oil was applied on the testing sample surfaces to simulate a boundary lubricant condition. The tribometer gave the coefficient of friction during the tests. The SEM with EDX was employed for study of wear mechanism and wear loss of counterface material. The wear volume loss of counterface steel balls illustrated in Fig. 3.11 was calculated by partially filled sphere equation (Eq. 3.2).

$$V = \frac{\pi}{3} Y^2 (3R - Y) \qquad (3.2)$$

Where $Y = \sqrt{R^2 - r^2} + R$

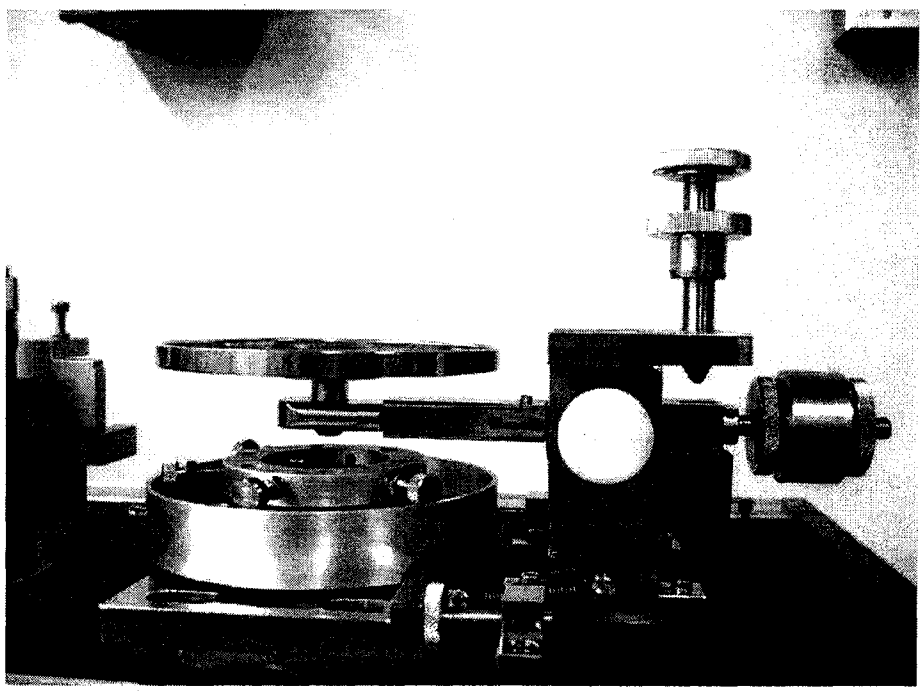

Fig. 3.10 Sciland Pin/Disk Tribometer PCD-300A

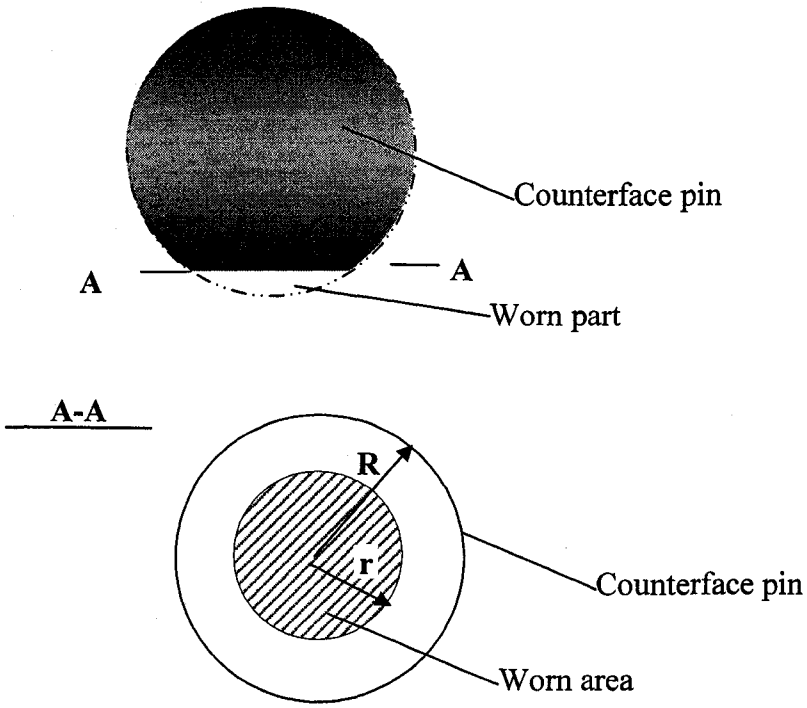

Fig. 3.11 Schematic of the worn counter pin/ball and its volume loss.

CHAPTER 4

EXPERIMENT RESULTS AND DISCUSSION

PART A – SILICON EFFECT ON PEO COATINGS ON Al-Si ALLOYS

4.1 Results

4.1.1 Metallurgical analyses of the Al-Si alloy substrates

Metallurgical analyses were conducted by optical microscopy. Optical photographs of the Al 319 and 390 alloys are given in Figs. 4.1(a-d). Fig. 4.1(a) shows a typical hypoeutectic Al-Si 319 alloy microstructure. Coarse Al-dendrites were separated by fine Al-Si eutectic. Fig. 4.1(b) shows the refined silicon crystal morphology in Al-Si eutectic. In Figs. 4.1(c, d), optical photographs of the 390 Al alloy exhibit a typical hypereutectic Al-Si alloy microstructure with a non-uniform distribution of needle-like and limited primary Si particles in the matrix of α-Al.

4.1.2 Voltage variation during the PEO process

Figs. 4.2(a) and 4.2(b) show the voltage change during the PEO treatment on Al 319 and Al 390, respectively. Four consecutive stages can be distinguished approximately by changes in voltage variation, surface morphology, and the mechanisms of coating formation during the whole anodic oxidizing process. Insets in Figs. 4.2(a) and 4.2(b) particularly show the difference between the regions III and IV in the voltage increasing slope.

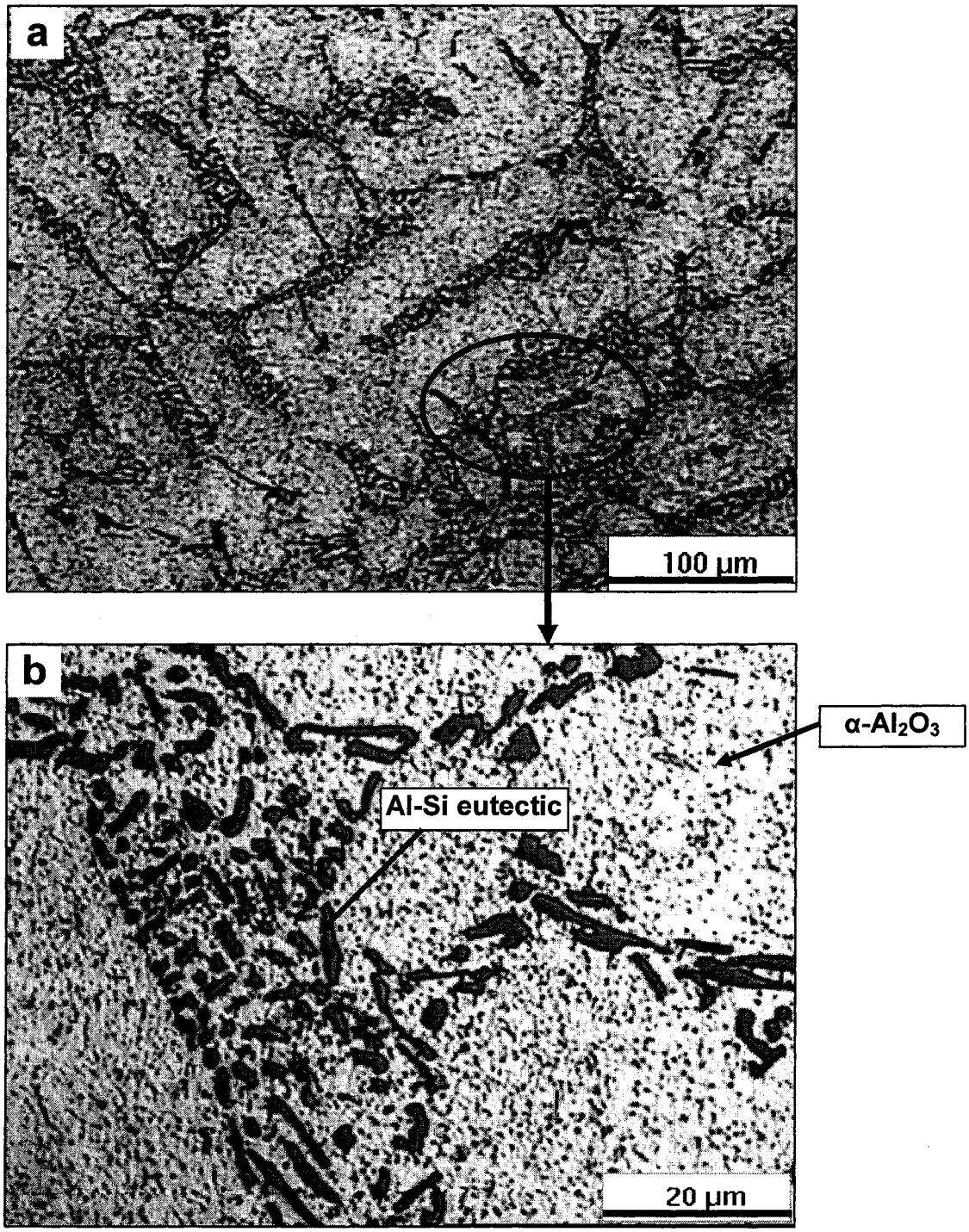

Fig. 4.1(a, b)

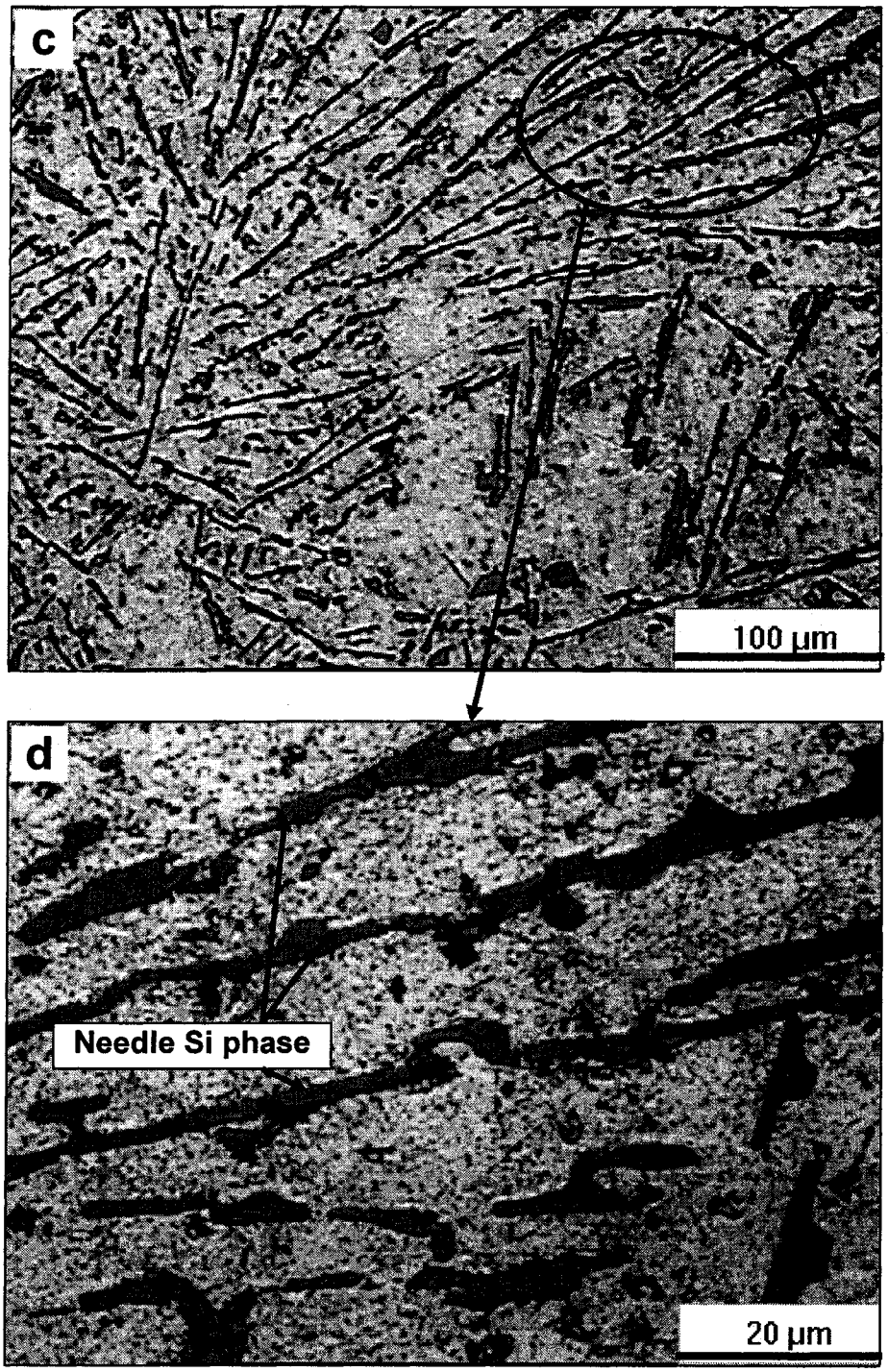

Fig. 4.1 Optical micrographs of as-cast aluminium alloys after polishing and etching, showing Si phase distributions in (a, b) 319 and (c, d) 390 aluminium alloys at low and high magnification, respectively.

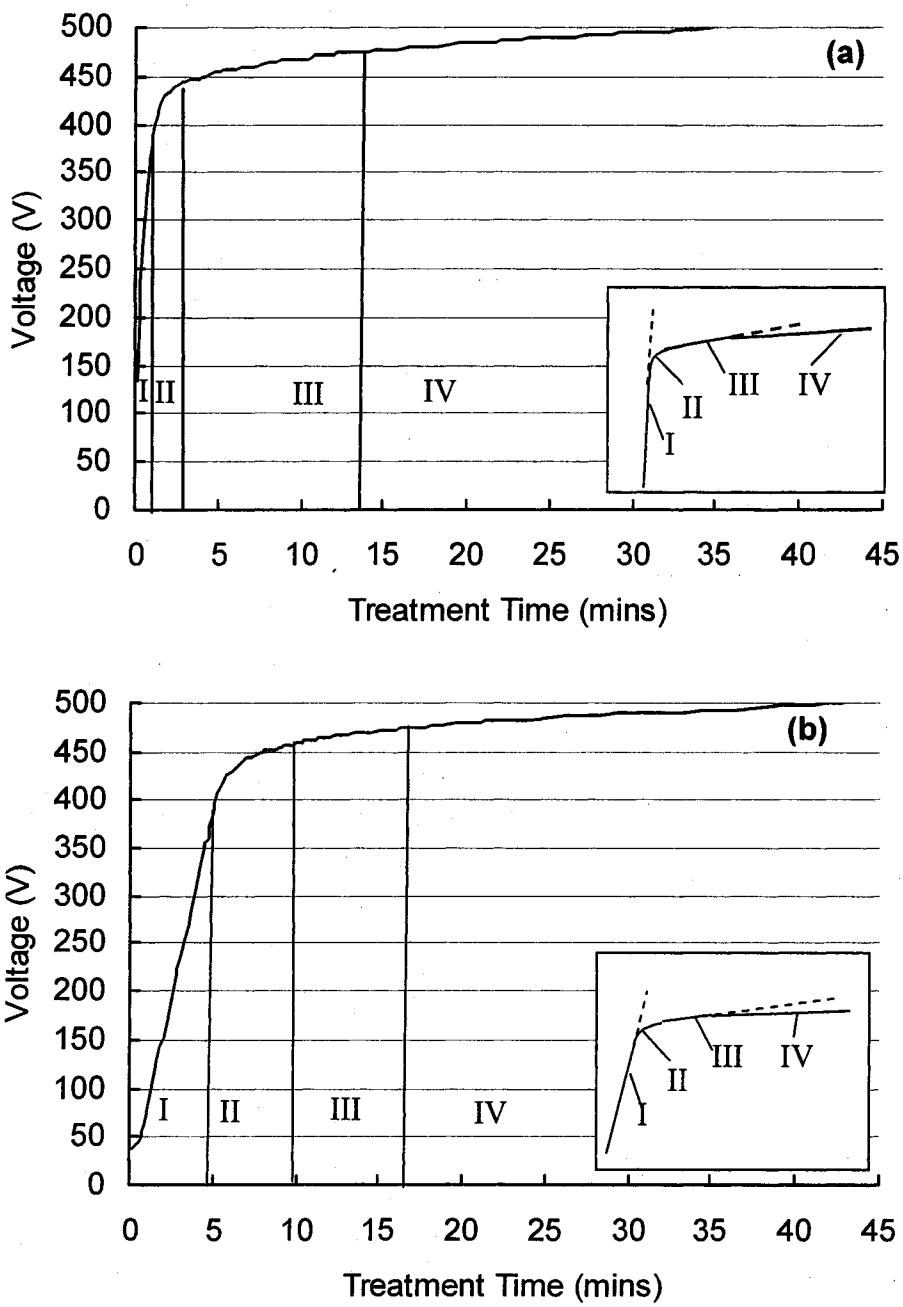

Fig. 4.2 Plots of voltages vs. treatment time during the PEO treatments (a) on the 319 aluminium alloy and (b) on the 390 aluminium alloy with the insets showing the difference in the voltage increasing slope between the regions III and IV.

The first stage started with a conventional anodic oxidation on the sample surface. A rapid linear increase in voltage was observed. For the 319 alloy the voltage jumped to 390 V in the first 1 minute, while the duration of stage I (from 0 to 400 V) for the 390

alloy was about 5 minutes. The difference in the voltage increasing rates indicated that the oxide film more readily formed on the 319 alloy than on the 390 alloy in the first stage.

In the second stage, the voltage increasing rate slackened and the curves in this stage were not linear anymore. Micro-arc discharges could be observed by naked eyes at this stage and beyond. The stage II ranging from 390 V to 440 V lasted about 1.5 minutes for the 319 alloy, whereas for the 390 alloy this stage (from 400 V to 465 V) extended about 5 minutes.

With the voltage increasing, the process entered stage III. The voltage biased on the 319 alloy gradually climbed up from 440 V to 480 V with the average voltage increase rate of about 2.79 V/min, while the coating process on the 390 alloy caused the voltage increase from 465 V to 480 V at the voltage increase of 1.65 V/min.

Beyond 480V, both of the coating processes on the 319 and 390 alloys were engaged into stage IV, and the voltage increasing slopes in this stage were similar.

4.1.3 Surface morphology and composition characterization in the four stages

Figs. 4.3(a-f) illustrate the surface changes of the PEO-treated 319 and 390 samples at the stages II-IV. Higher magnification SEM micrographs of those coated surfaces with EDX analysis are presented in Figs. 4.4-4.9.

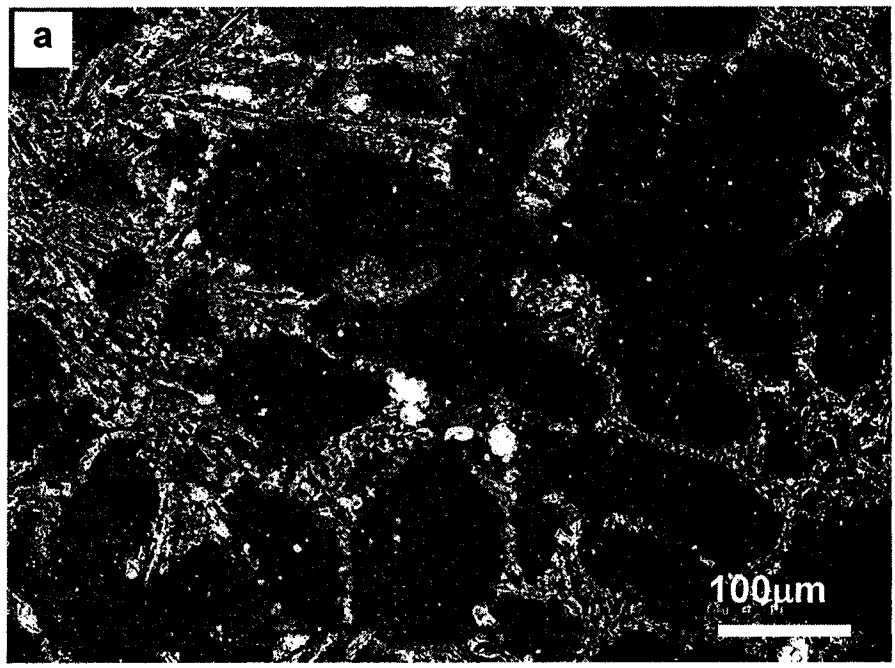

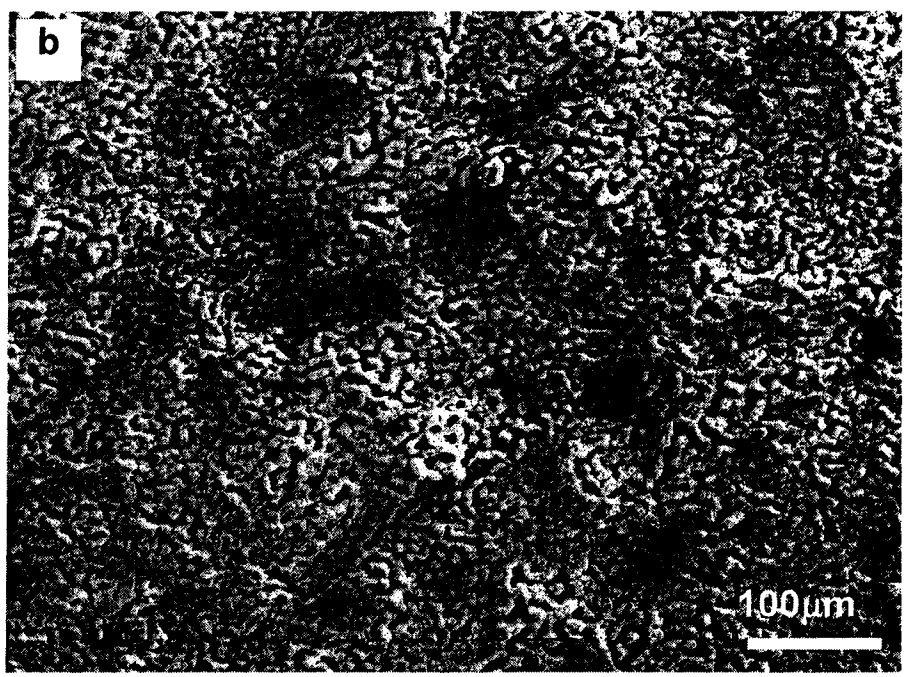

Fig. 4.3(a, b)

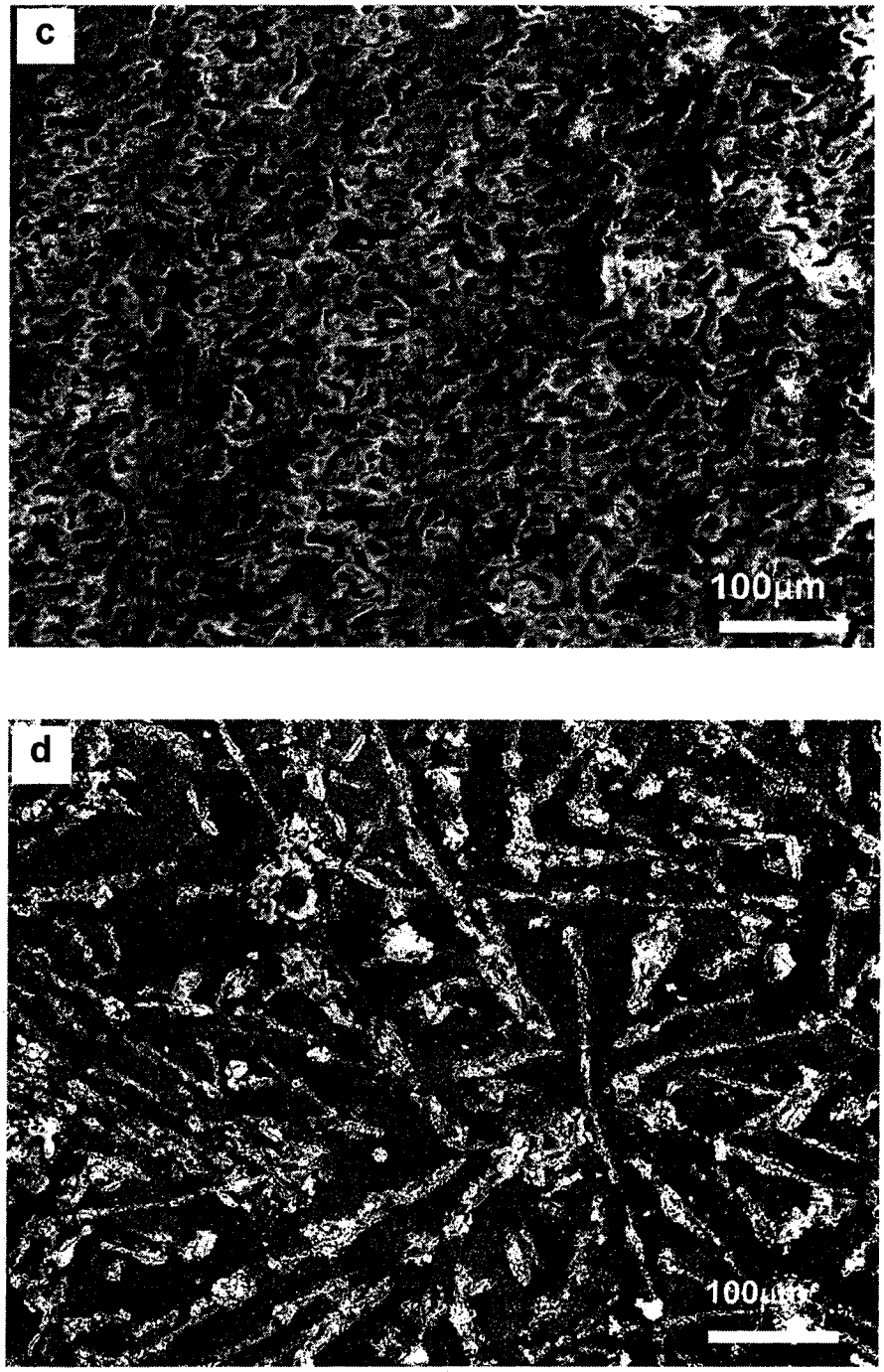

Fig. 4.3(c, d)

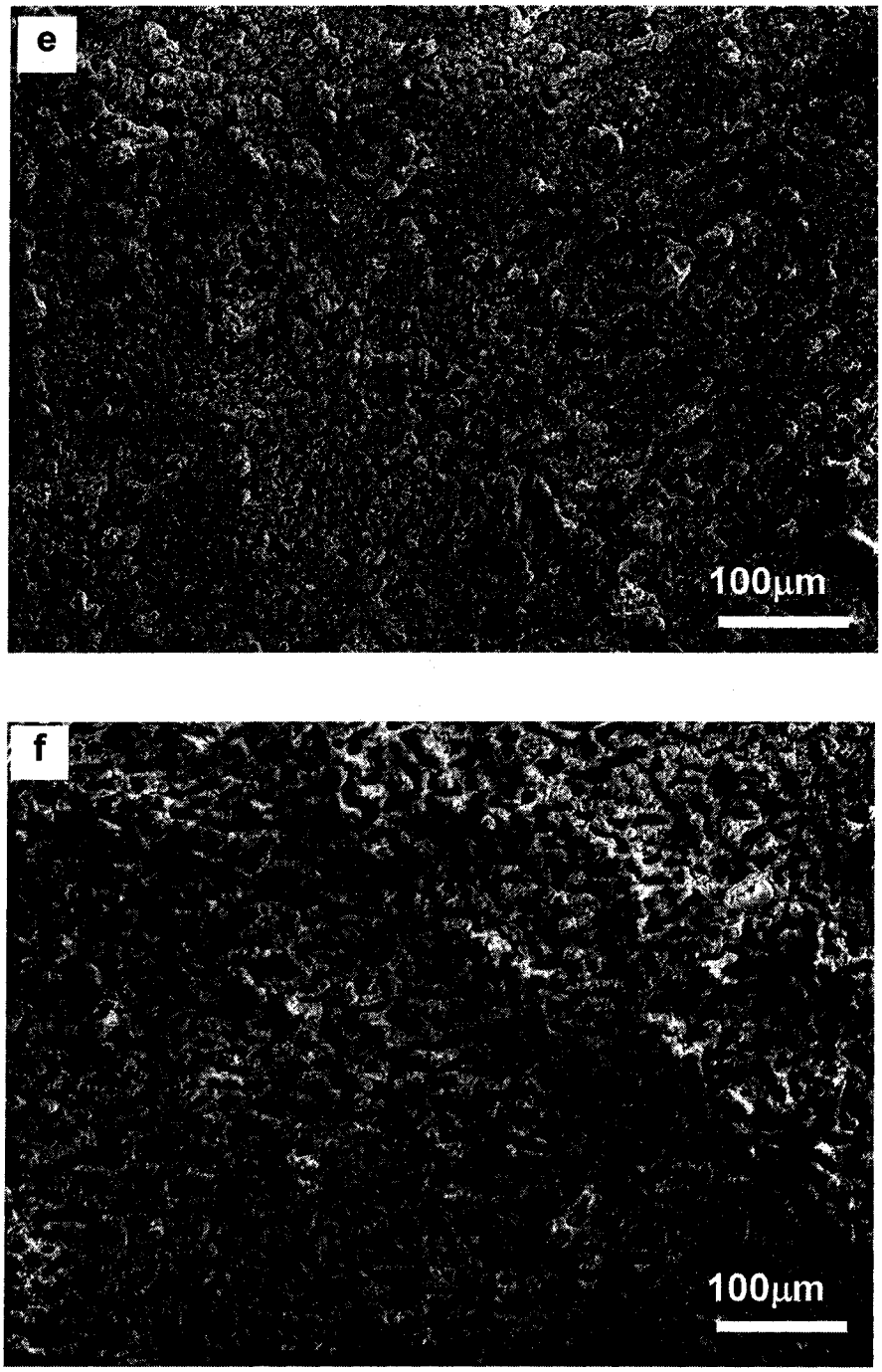

Fig. 4.3 SEM micrographs of coating surface morphology (a-c) on the 319 aluminium alloy and (d-f) on the 390 aluminium alloy at (a, d) stage II, (b, e) stage III, and (c, f) stage IV.

Figs. 4.4 and 4.5 are the surface morphology and EDX spectra detected from the treated 319 and 390 alloy samples at the stage II. While Figs. 4.4(a) and 4.5(a) show the surface morphology of the Al matrix regions, Figs. 4.4(b) and 4.5(b) present the surface morphology of Si phase regions on treated 319 samples and 390 alloy. Figs. 4.4(c) and 4.5(c) are EDX spectra for the corresponding region *i* and region *ii* on the two samples. Figs. 4.4(d) and 4.5(d) are the micrographs of a magnified Si particle at stage II, on 319 alloy and 390 alloy respectively. In the Al matrix region (region *i* in Figs. 4.4(a) and 4.5(a)), anodized aluminium oxide film was partially fused because of the tiny micro-arc discharges initiated in the stage II. In the Si rich region (Figs. 4.4(b) and 4.5 (b)), relatively large melting Si cells can be observed and main chemical compositions in these cells are Si-Al-O compounds which can be detected by EDX (Figs. 4.4(c) and 4.5 (c)). At this stage, the sizes of these Si cells are determined by the original sizes and shape of Si phases in the substrates. The micrographs of the magnified silicon cells (Figs. 4.4(d) and 4.5(d)) show that the edge of silicon particle has been melted and the boundary of Si particles became blurred. But some core parts of the silicon particle are not melted. Thus, it can be implied that at stage II, a stronger micro-arc discharge readily formed on the surface spots where the interface of Al matrix and silicon grain existed due to the tip/corner effect of electrical field concentration. Consequently, a large melted cell formed during the plasma discharge and then the solidified oxide surrounded the silicon particle surface after the discharge was extinguished at the current spot and moved to another location. The silicon surface was melted, and the silicon was mixed with the aluminium oxide during the formation and extinguishing of micro-arc discharge. Thus, amount of Si-Al-O compounds (Figs. 4.4(c) and 4.5(c)) with voids and bubble-like cavities were observed in the silicon region (Figs. 4.4(b) and 4.5(b)). The silicon mixture

to the aluminium oxide would reduce the melting temperature of the oxide compound, and lead to a larger melted cell that finally covered the whole exposed surfaces of original silicon grains.

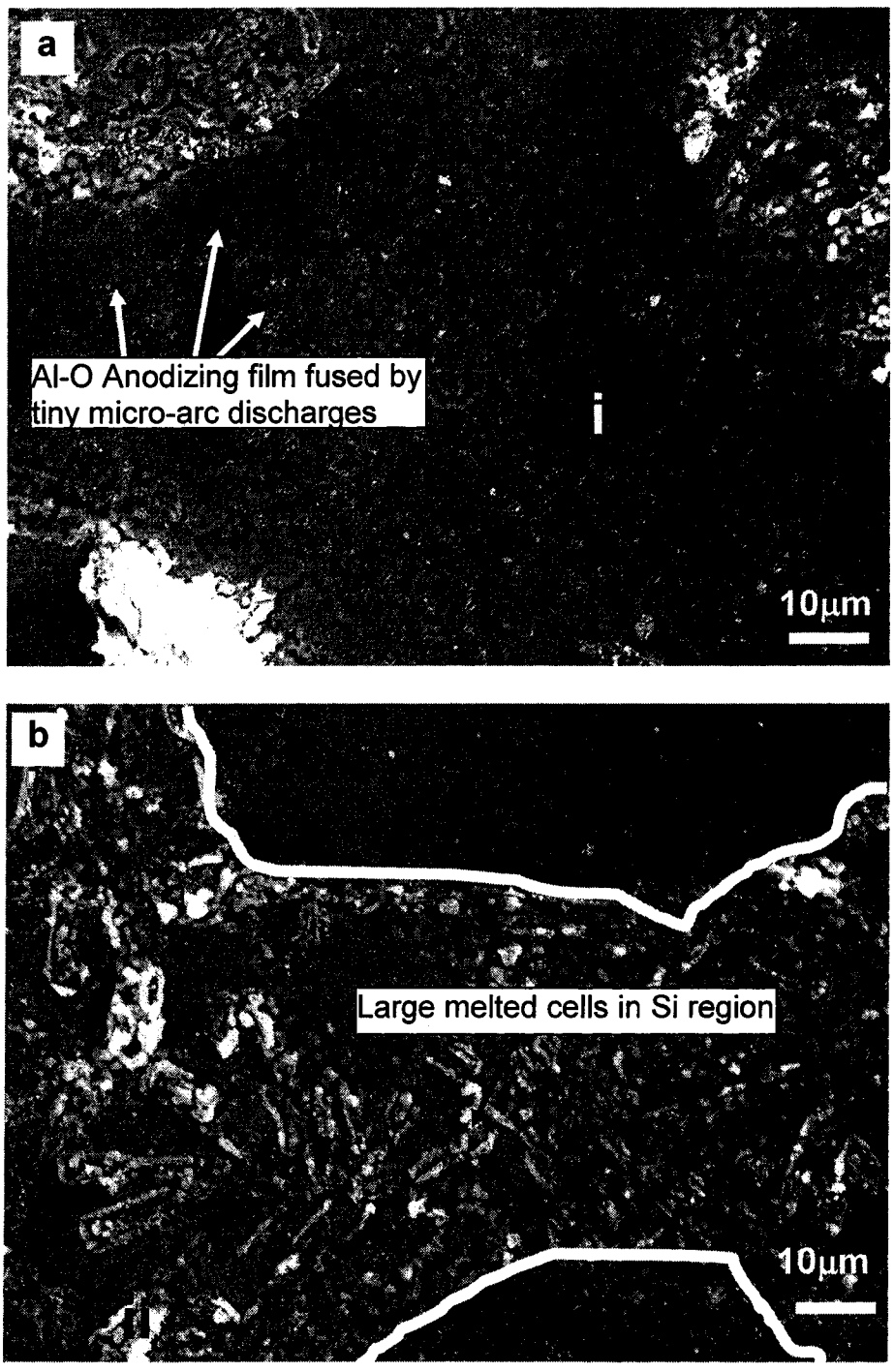

Fig. 4.4(a, b)

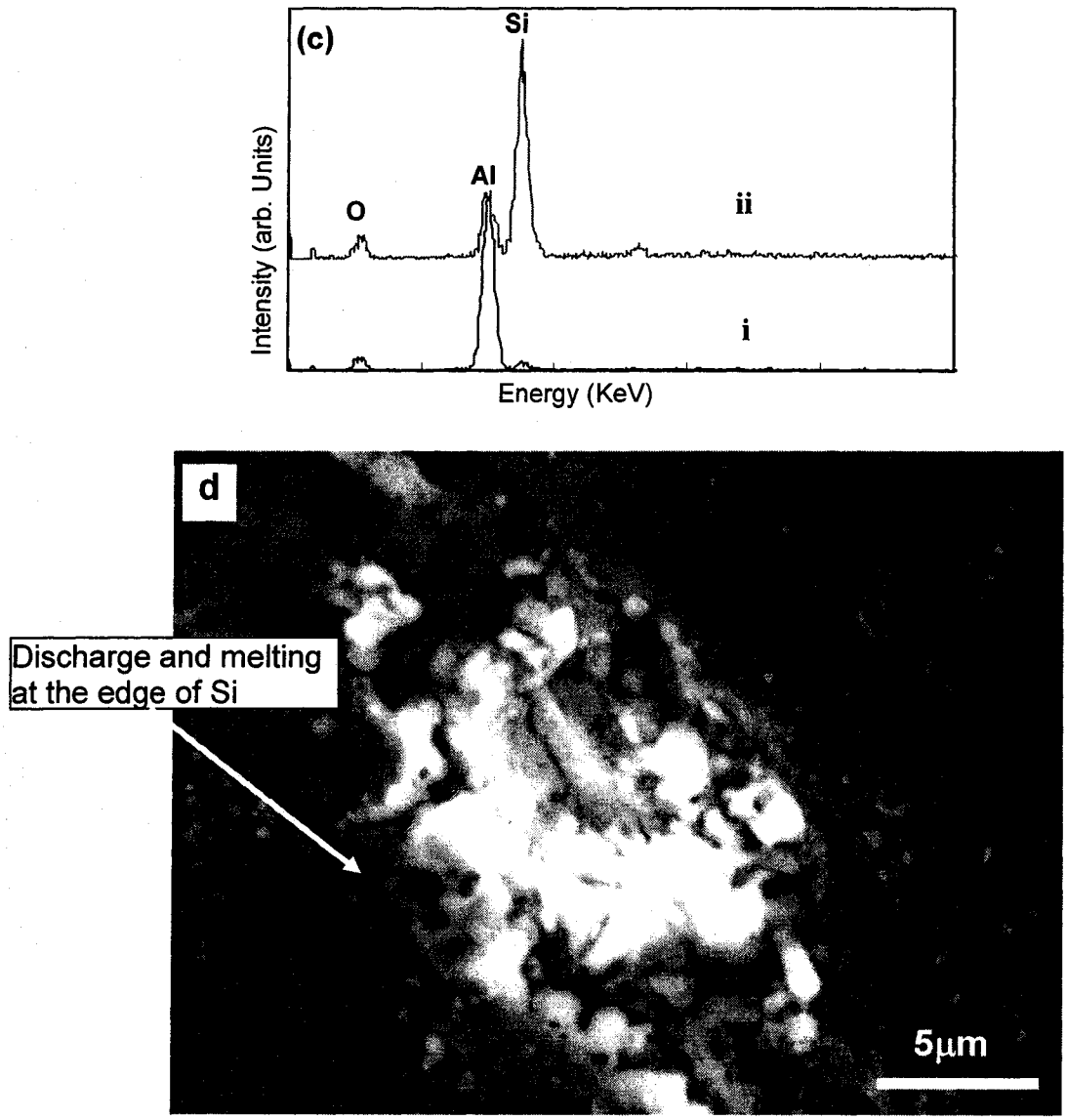

Fig. 4.4 SEM micrographs showing morphology of coating surfaces in stage II on the 319 alloy: (a) in Al matrix region and (b) the Al-Si eutectic region; (c) the corresponding EDX spectra for region *i* and *ii*; (d) a silicon particle at the stage II.

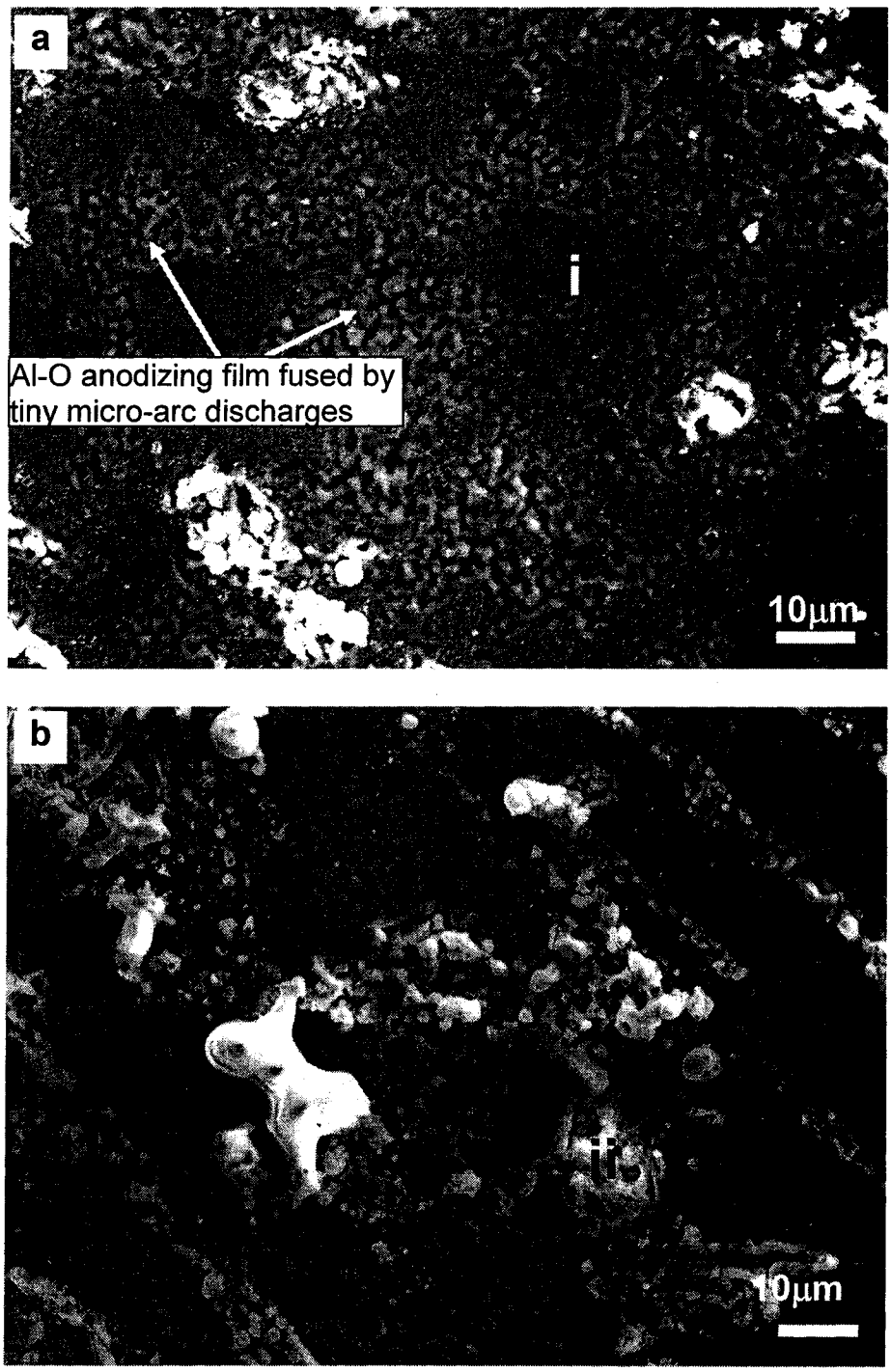

Fig. 4.5(a, b)

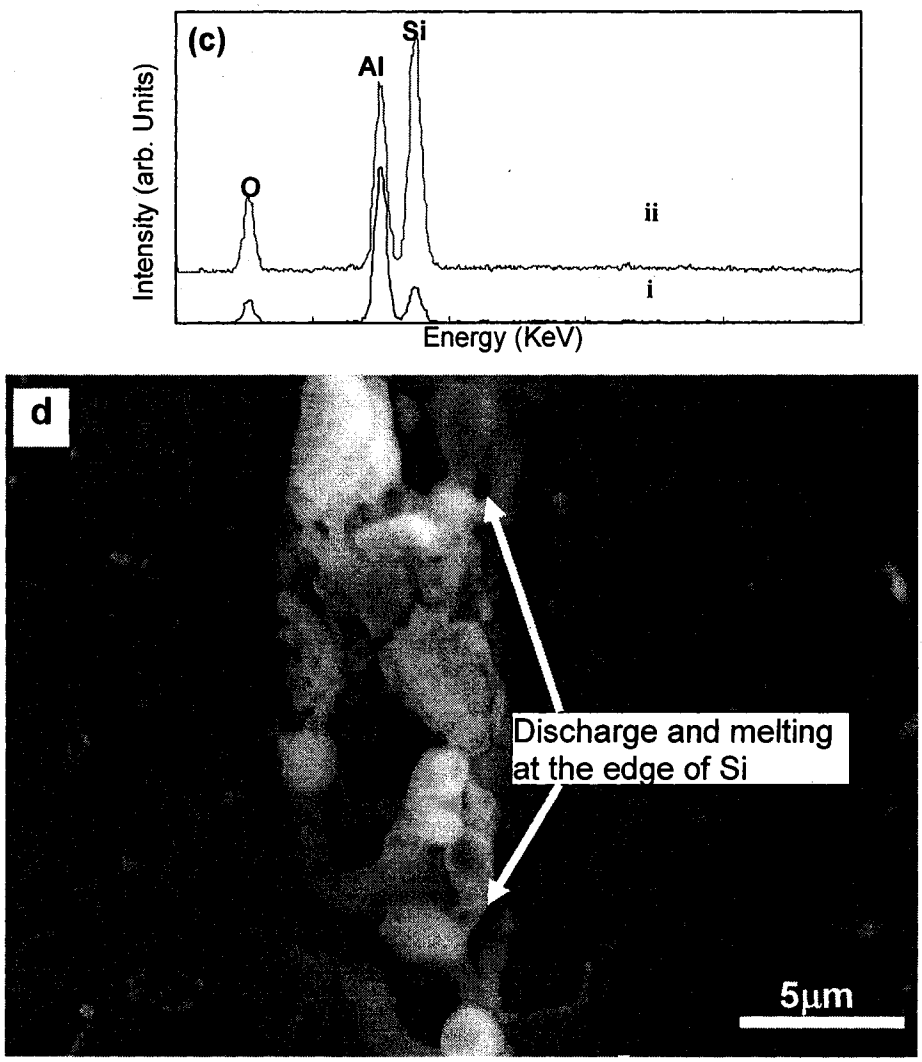

Fig. 4.5 SEM micrographs showing morphology of coating surfaces in stage II on the 390 alloy: (a) in Al matrix region and (b) the Al-Si eutectic region; (c) the corresponding EDX spectra for region *i* and *ii*; (d) a silicon particle at the stage II.

Figs. 4.6 and 4.7 are the surface morphologies and EDX spectra detected from the treated 319 and 390 alloy samples at the stage III respectively. Figs. 4.6(a) and 4.7(a) show the surface morphologies of samples treated at stage III on 319 and 390 alloy respectively. Figs.4.6 (b) and 4.7(b) are EDX spectra for the corresponding region *i* and region *ii* on the two samples respectively. On the 319 alloy sample, the coating surface is inhomogeneous and presents a granular meshwork aspect revealing two kinds of zones. The zone *i* (Fig. 4.6(a)) is made of small particles between which small circle pores existed. From EDX analysis, the chemical composition of the particles is main Al and O. EDX spectrum indicated the zone *ii* (Fig. 4.6(a)) is made of Si rich compound. The Si-Al-O compounds appear to have larger projections between which are elliptical pores. On the 390 alloy, porous silicon rich compounds (region *ii* in Fig. 4.7(a)) piled up from the base background where a much denser aluminium rich oxide formed (region *i* in Fig. 4.7(a)). The silicon rich compound regions were more readily fused, resulting in a preferential coating growth and large coating porosity.

The surface morphology of the 319 and 390 alloys treated at stage IV is shown in Figs. 4.8(a) and 4.9(a) respectively. A similar coating morphology could be observed on the coated 319 and 390 surfaces. It was also found that the coated 319 and 390 alloy surfaces had a similar EDX spectrum (Figs. 4.8(b) and 4.9(b) respectively). In this stage, the coatings on both of the alloys exhibited fairly even composition coverage, and the original aluminium region and silicon region could not be distinguished from the EDX composition analysis. Thus, the coatings on both alloys were Al-Si-O compounds with a uniform distribution in composition. It should be mentioned that at the maximum output 500V, the continuous dense layer of coating has not been formed yet.

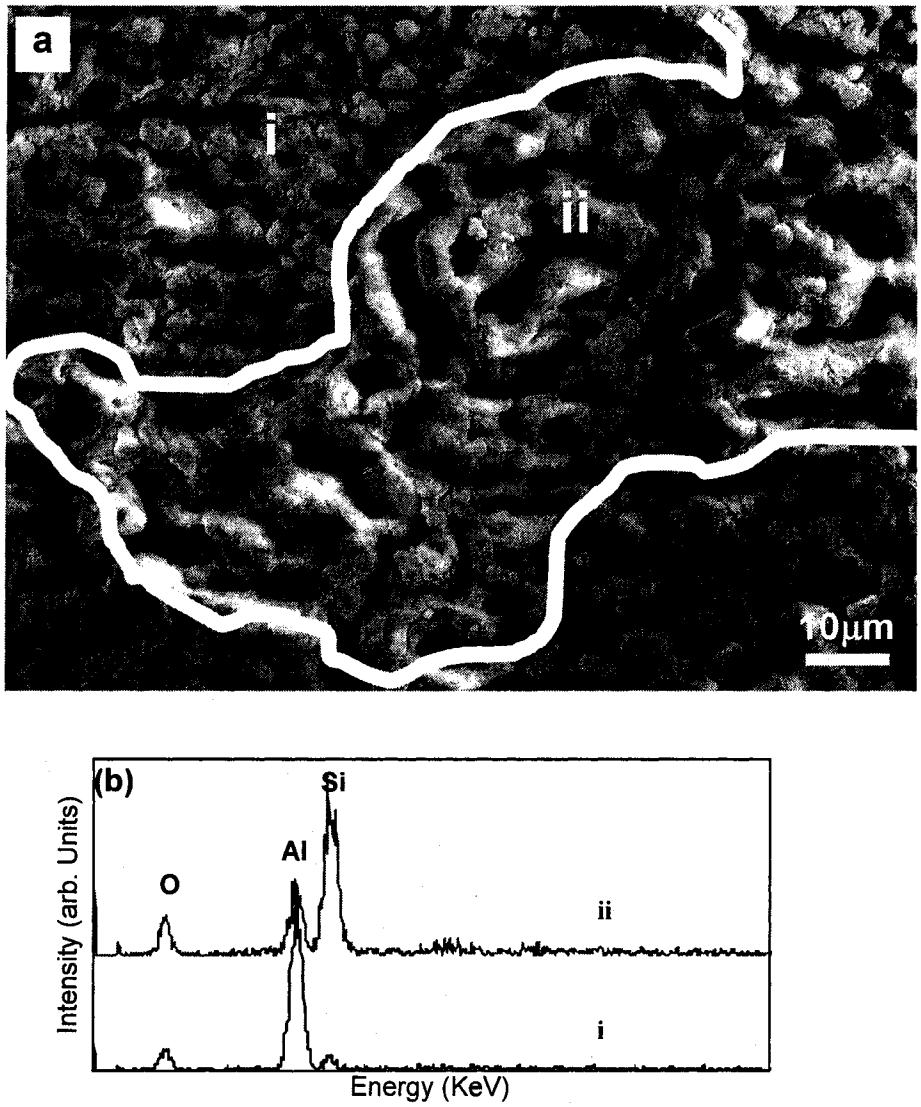

Fig. 4.6 (a) A SEM micrograph showing morphology of coating surfaces in stage III on the 319 alloy and (b) the corresponding EDX spectra for region *i* and *ii*.

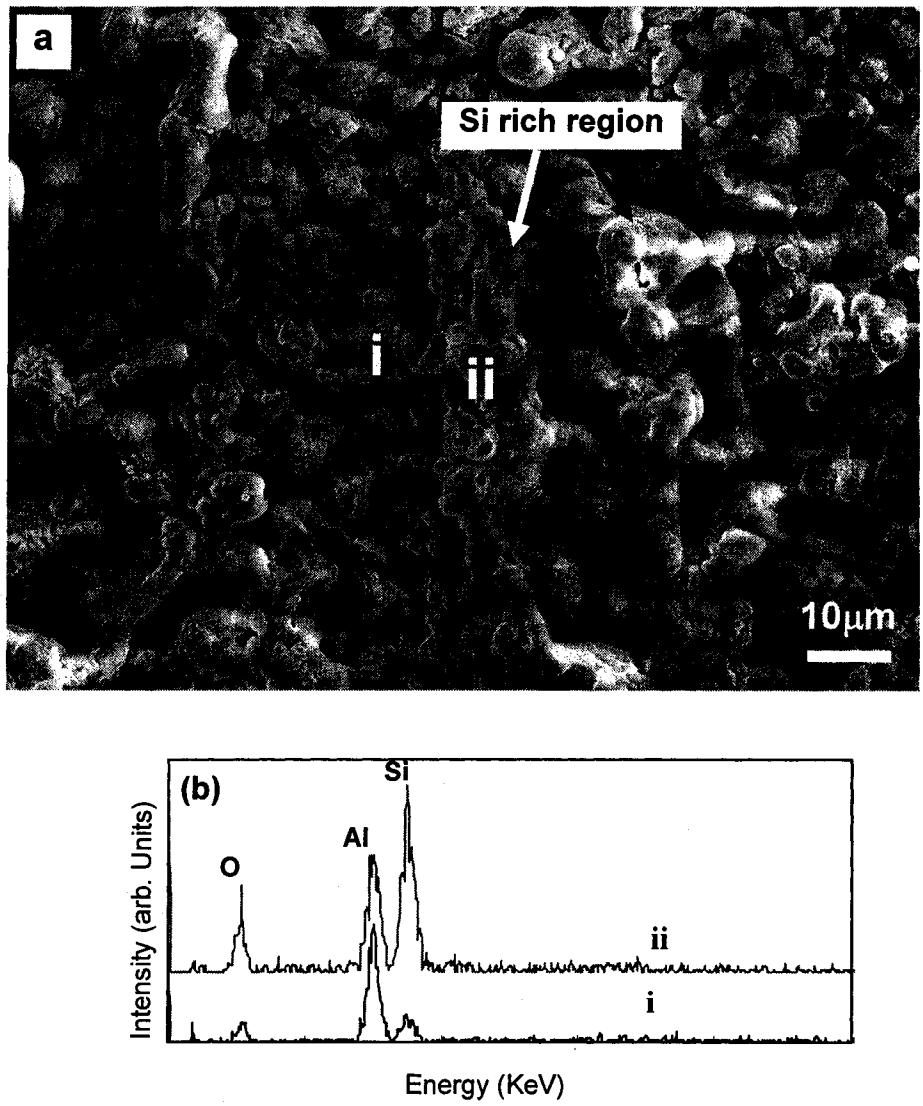

Fig. 4.7 (a) A SEM micrograph showing morphology of coating surfaces in stage III on the 390 alloy and (b) the corresponding EDX spectra for region *i* and *ii*.

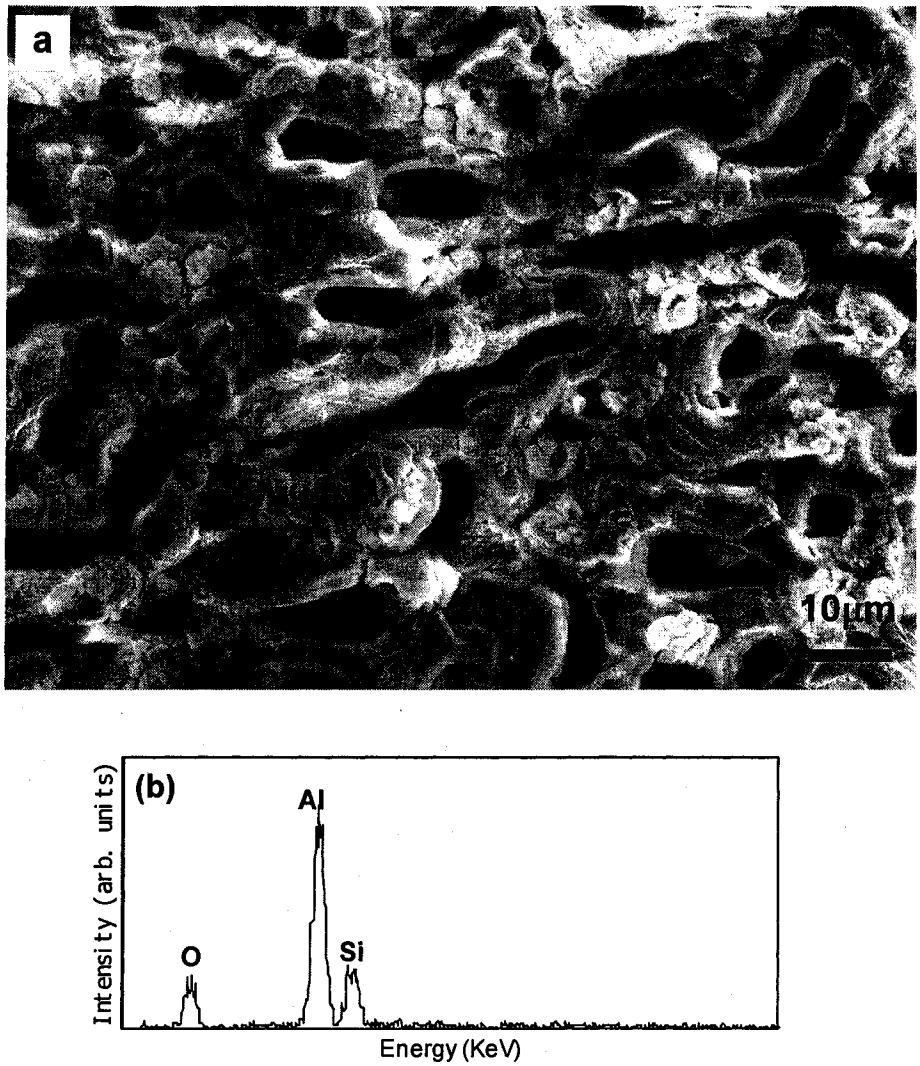

Fig. 4.8 (a) A SEM micrograph showing morphology of the coating surface in stage IV on the 319 alloy and (b) the corresponding EDX spectrum.

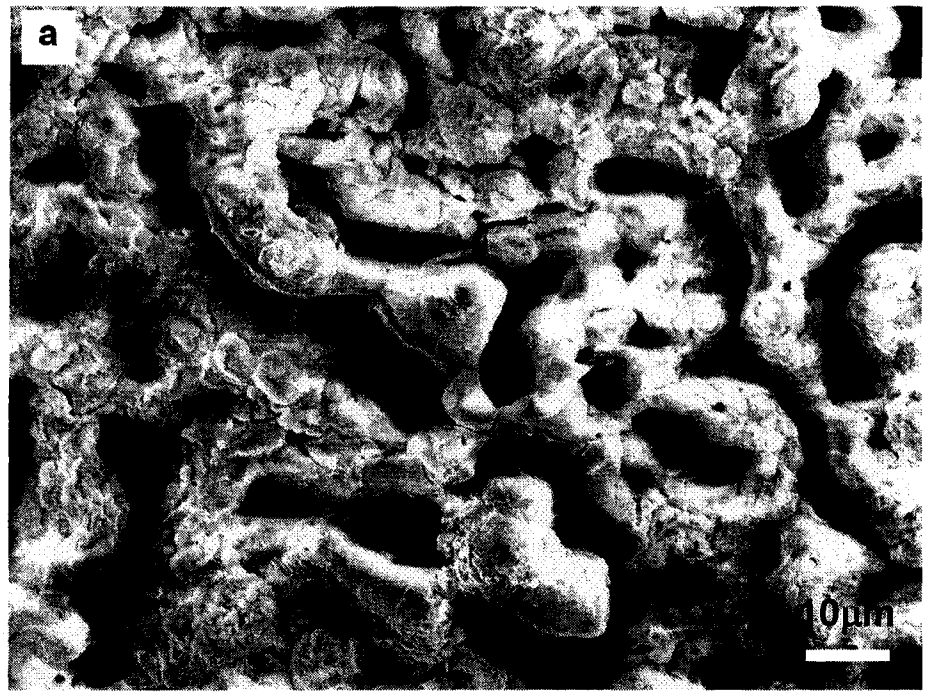

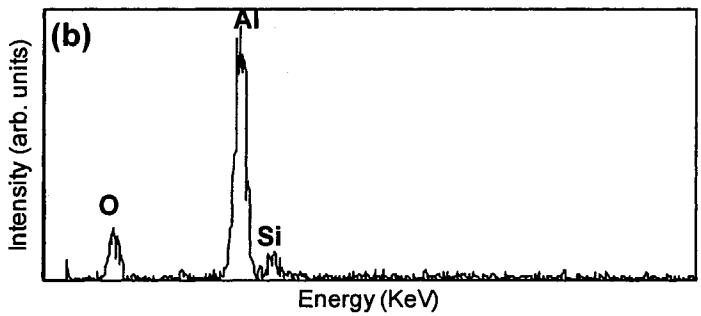

Fig. 4.9 (a) A SEM micrograph showing morphology of coating surfaces in stage IV on the 390 alloy and (b) the corresponding EDX spectrum.

4.1.4 Surface roughness

Surface roughness vs. treatment time is plotted in Fig. 4.10. A nearly linear increase in coating roughness was observed at the first 3 stages for the low silicon 319 alloy; whereas the high silicon 390 alloy behaved quite differently at various process stages. At the stage II, the coating on the 390 alloy had a much higher surface roughness compared with the coating on the Al 319. Then, the surface roughness increase slop descended in the stage III as shown in Fig. 4.10. At the stage IV, the surface roughness on the coated 390 was still higher than that of the coated 319 alloy; however, the roughness increase rate for the treated 390 alloy significantly declined.

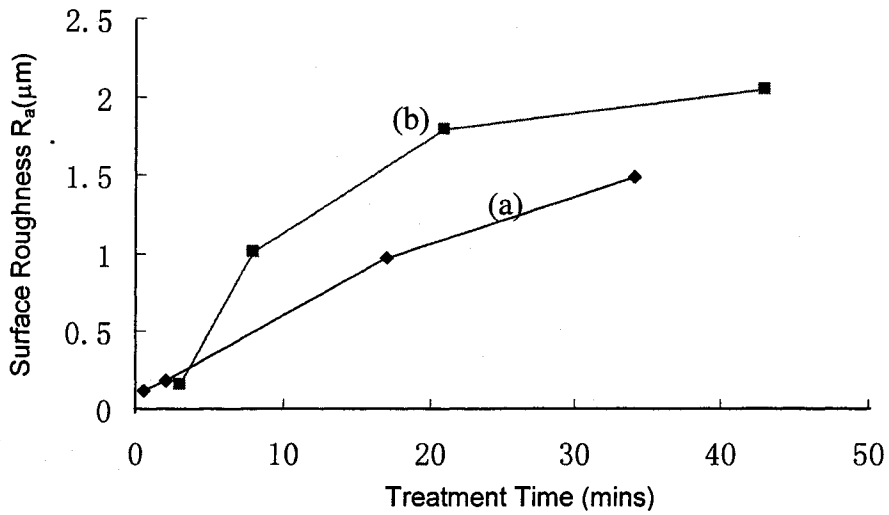

Fig. 4.10 Surface roughness Ra vs. treatment time on (a) the 319 alloy and (b) the 390 alloy.

The highest voltage applied in this research was 500V due to the power supply limitation. According to previous research on a thick Al-Si-O oxide coating [17, 21], the oxide coating has three layers, i.e., porous top layer, dense intermediate layer, and dense inner layer. When the voltage is increased to more than 600V and the coating thickness

reaches up to over 50 μm [51, 66], thickness of dense layer in the coating can be significantly increased. Thus, if the applied voltage in this research was higher, the density of the coating could be considerably improved due to the further sintering at the higher voltage and the coating surface roughness on both of the substrates could finally become similar. The effect of Si content on coating roughness and morphology might not be significant when a thick coating was deposited; for a thin coating, its effect was obvious.

4.1.5 XRD analysis

Figs. 4.11(a-f) show XRD patterns of the samples treated at four individual stages on the 319 alloy and the 390 alloy, respectively. The aluminium (Al) and silicon (Si) peaks in Fig. 4.11 were detected from the Al-Si alloy substrates. An Al_2O_3 phase was found in the coatings on both 319 and 390 alloys prepared at the stage II (circles in Figs. 4.11(a) and 4.11(d)). γ-Al_2O_3 phase started to form in the coatings from the stage III (Figs. 4.11(b) and 4.11(e)), and the coatings were composed of γ-Al_2O_3 and very little amount of mullite. At the stage IV, the γ-Al_2O_3 was still the dominate phase in the coating (Figs. 4.11(c) and 4.11(f)), however, the amount of mullite phase was increased compared to the stage III, suggested that silicon element from the silicate electrolyte was incorporated into the coatings at the stage IV. Compared with the XRD patterns of those two coated samples treated at the same individual stage, the phase structures on the coatings were similar.

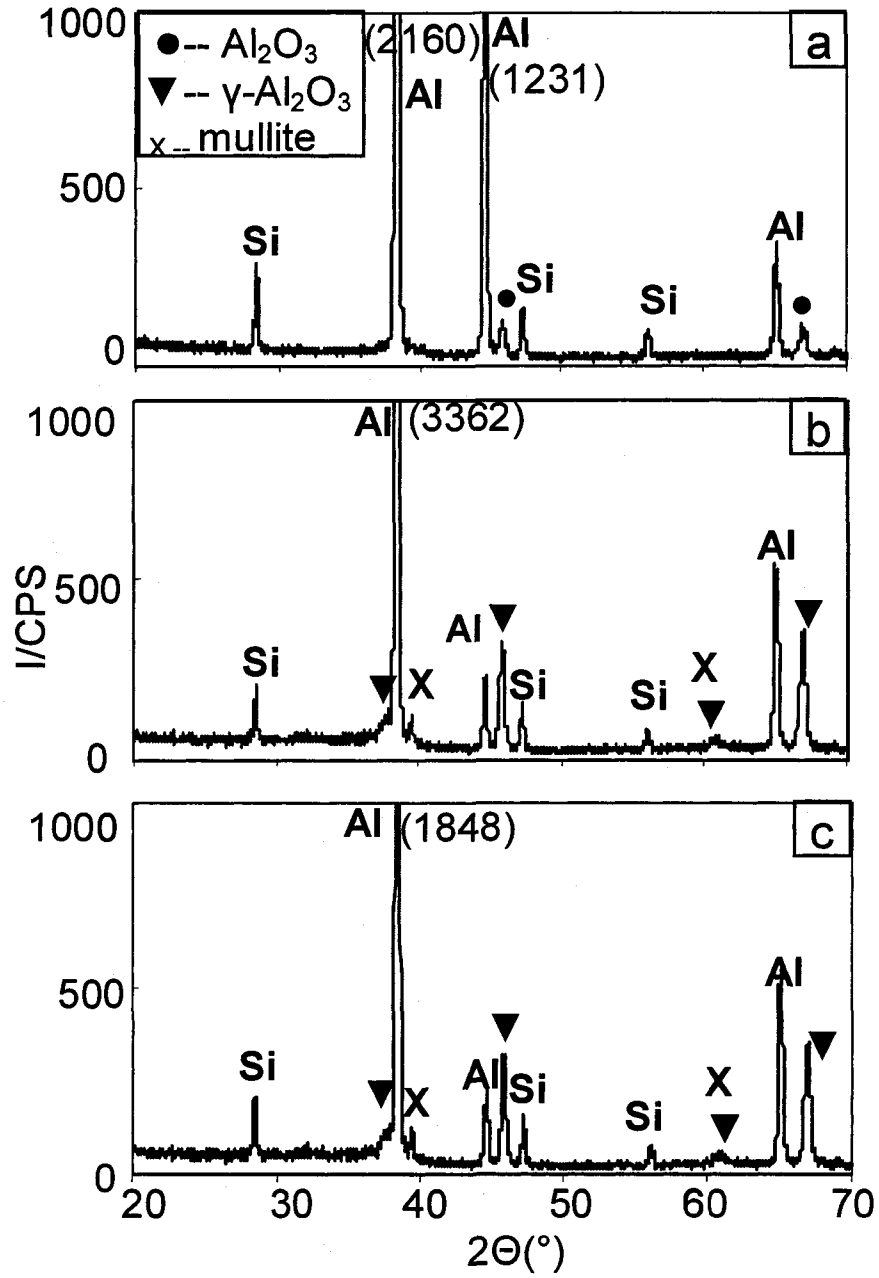

Fig. 4.11 (a, b, c)

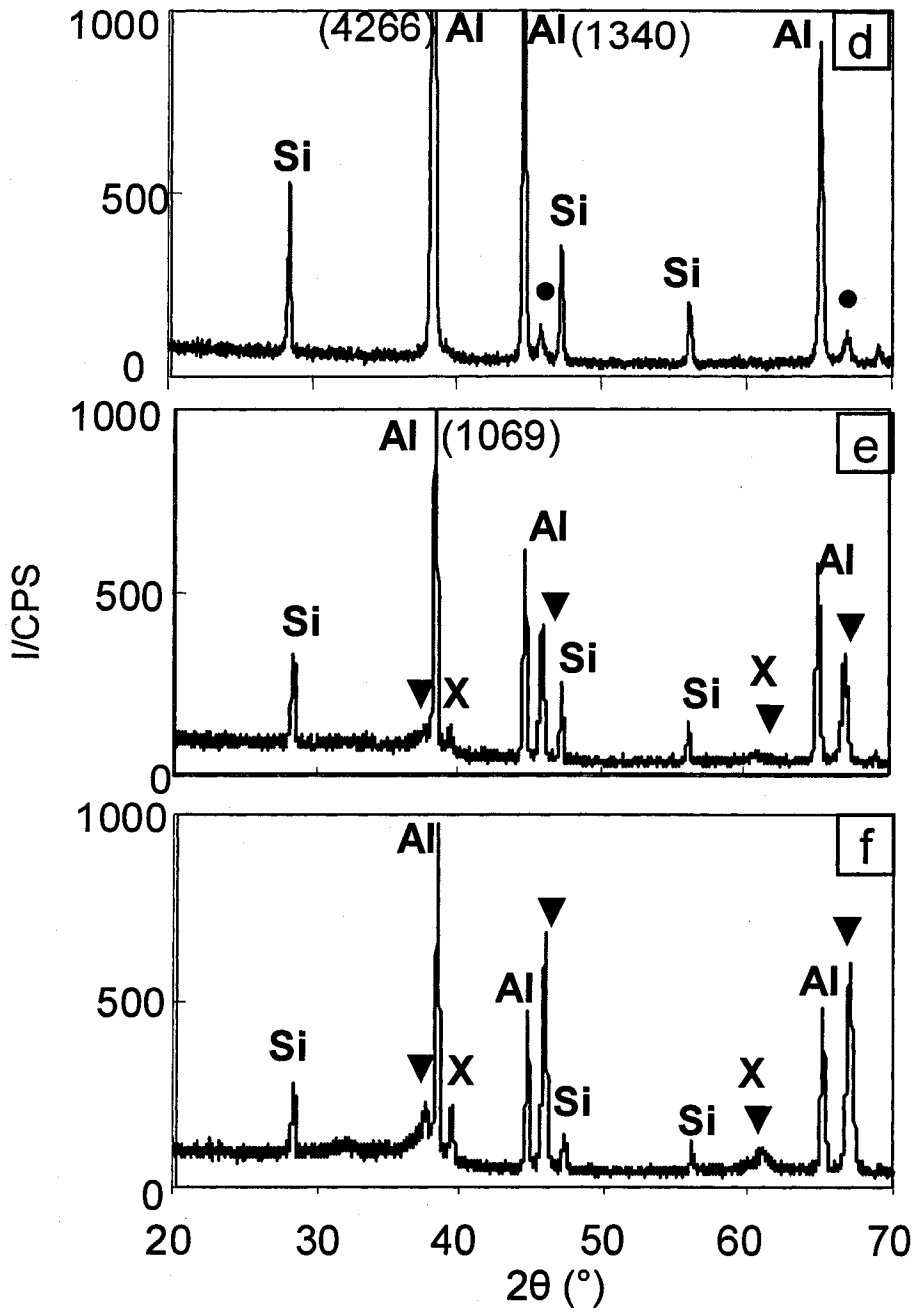

Fig. 4.11 XRD patterns of the PEO coatings on the 319 and 390 alloy at (a, d) stage II, (b, e) stage III, and (c, f) stage IV. Note: the numbers in brackets are the intensity of the peaks.

4.1.6 Cross-sectional structure of coatings

Figs. 4.12 (a) and 4.12(b) are the micrographs of cross-sections of the coated 319 and 390 alloys respectively. The coatings treated to 500V on both alloys are about 10μm in thick. The cross-section micrograph exhibits the typical PEO coating structure, i.e. porous outer layer, dense layer and continuous inner dense layer. In the coating on the 319 alloy, the dense layer is not continuous, the thickness is from 0-3μm, while the dense layer on the 390 alloy is more continuous and thicker with a thickness 3-5 μm. Fig. 4.12(a) shows that at the regions Si phase, some pores deducted by discharge and some porous spheroidal projection aspects existed. The discharge channels go through the entire coatings from inner dense layer to outer layer. However, these phenomena become not so on the cross-section of coated 390 alloy surface. It could be implied that with a continuous dense layer forming, Si particles in the aluminum alloy were oxidised and sintered into the dense layer. Thus, with the growth of dense layer, the effect of Si content of the substrates on surface properties becomes weak.

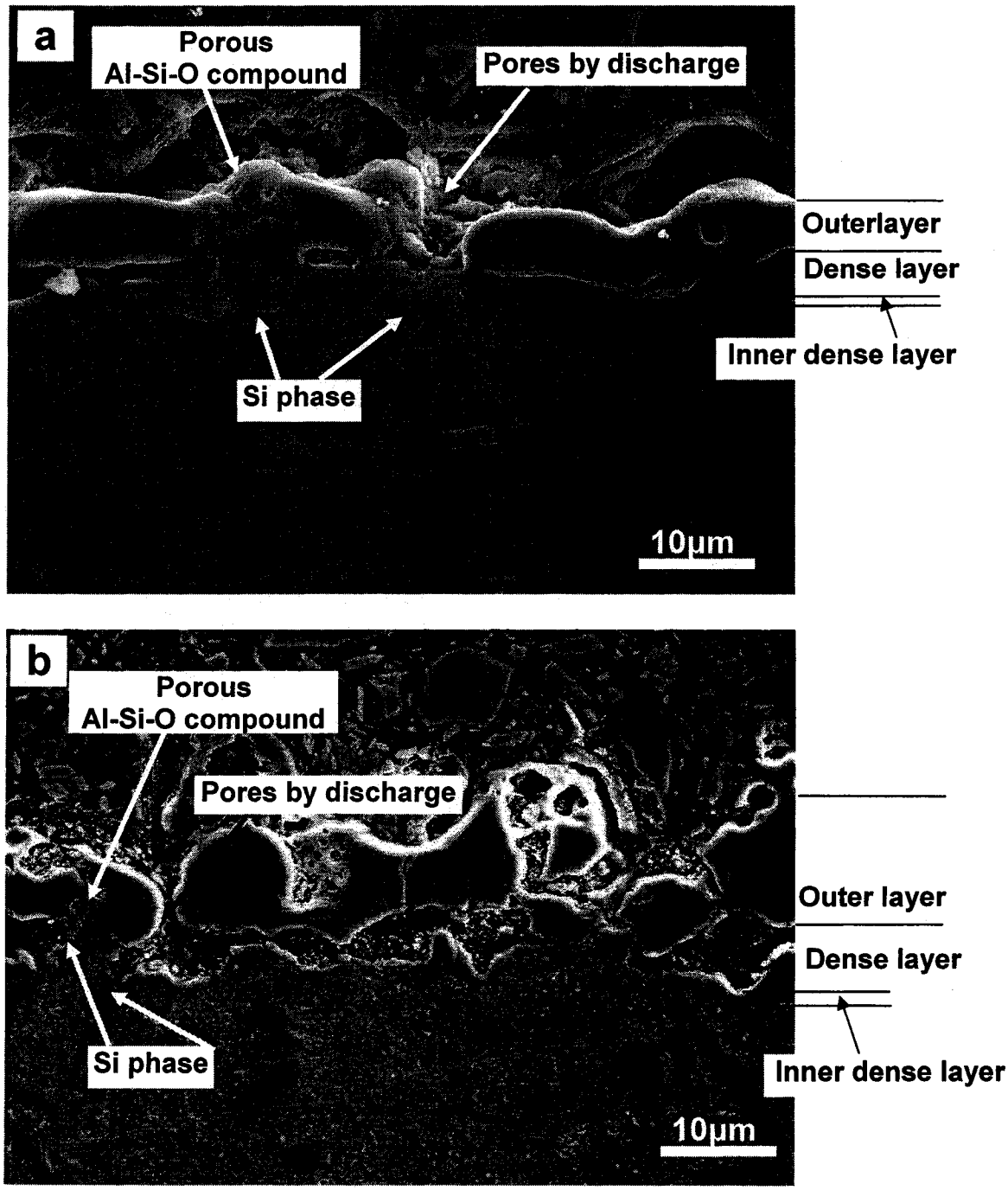

Fig. 4.12 SEM micrographs showing the cross-sectional morphology of the coated (a) 319 alloy and (b) 390 alloy (current density: 0.05A/cm^2, maximum voltage 500V).

4.2 Discussion

Investigation of the voltage variation with treatment time and corresponding surface morphology and EDX analysis on the PEO-coated Al-Si alloys has revealed four stages of the process, characterised by different mechanisms. Figs. 4.13(a-d) schematically illustrate the coating growth model of the PEO coating at the region of Si phase.

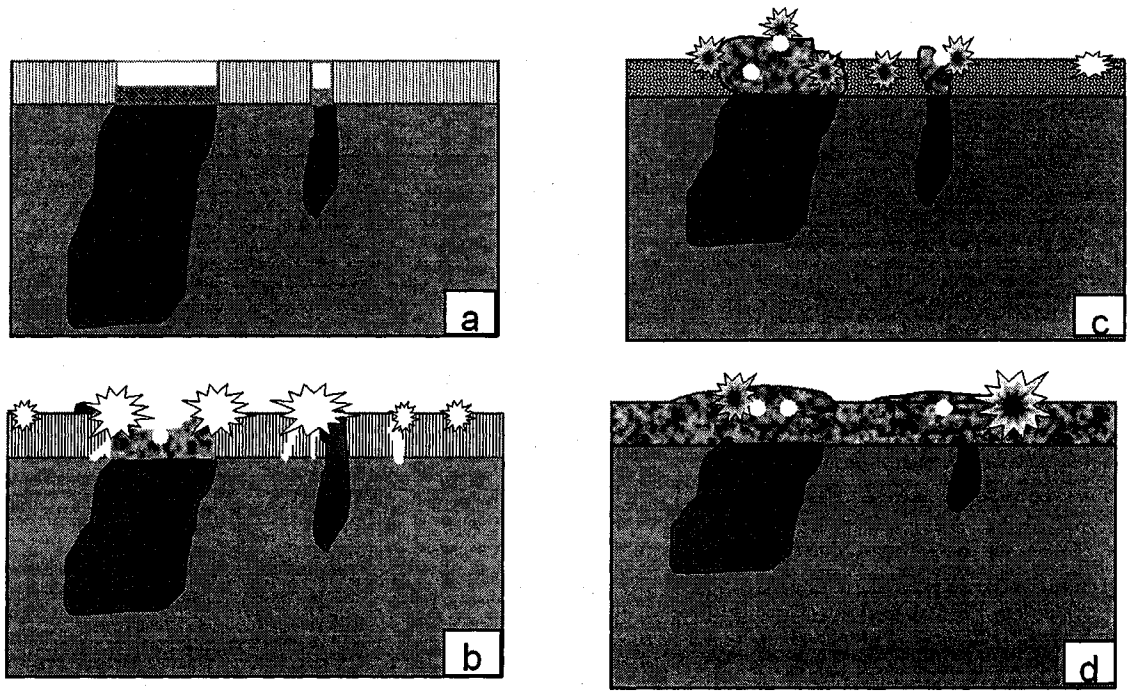

Fig. 4.13 Schematic of coating growth model around the Si regions at (a) stage I, (b) stage II, (c) stage III, and (d) stage IV.

The coating process started with a conventional anodic oxidation of the sample surface in Stage I (shown in Fig. 4.13(a)) where a rapid linear voltage increase was observed. The silicon precipitates, present in commercial aluminum-silicon alloys, are almost pure, faceted silicon crystals [67]. During this stage, the anodizing process occurred on the aluminium matrix regions, forming a conventional anodic oxidation film.

Silicon particles have low electrical conductivity (~10^{-4} $(\Omega \cdot m)^{-1}$), a passivation layer covered on silicon crystals only via chemisorption proceeds. This layer tends to be 6-20 nm thick [68]. Figs. 4.2(a) and 4.2(b) show that the voltage increase for the 319 alloy is much more rapid than that of 390 in this stage. Aluminium content is relatively higher in the 319 alloy than that of in the 390 alloy. Compared to silicon, aluminium is liable to be passivated. Thus, the 319 alloy has a higher oxide film growth rate than the 390 alloy. As a result, the voltage increasing slope for the former is larger than that for the latter in the first stage.

Whilst the aluminium oxide film growth, the electric potential (electric field strength) in the oxide film was increasing as shown in the stage II. (Figs. 4.4, 4.5 and 4.13(b)). Due to the tip/corner effect of electrical concentration on the localized surface where the interface of Al matrix and silicon grain existed, it was most likely that a large micro-arc discharge firstly formed at the Al-Si boundary when the voltage (electric field strength) in the coating with thickness in nano/micron-meter-scales reached a critical value (above dielectric strength of the oxides ~10^4 V/mm). During the process, a number of small sparks could also be observed at the region of the anodized Al matrix (Fig. 4.13(b)). The region of discharge was heated by generated electron avalanches up to temperatures of 10^3~10^4 K [23, 24] which is higher than the melting point of Si (~1410 °C) and SiO_X (<1800 °C), causing the silicon crystal surface to melt and be mixed with the aluminium oxide. Thus, Si-Al-O compounds firstly started to form in the silicon regions (Fig. 4.13(b)).

The Si-Al-O compound formed at the silicon region had a lower melting point than the aluminium oxide formed at the aluminium matrix region. The discharge would cause a large melted cell at the silicon region, and spheroidal projections were formed

after quenching by the electrolyte (Figs. 4.4, 4.5and 4.13(b)). The quenched projections contained a number of voids and bubble-like cavities. Due to its higher silicon content, the 390 alloy had larger coverage of the projections which caused a rougher surface on the 390 alloy than on the 319 alloy (Fig. 4.10). Again due to larger amounts of silicon in the 390 substrate, the number of discharge sites on the 390 alloy surface was larger than that on the 319 alloy surface. Thus, higher electrical quantities and electrical potential were needed, which can explain why the longer duration and higher final voltage for 390 alloy than for 319 alloy were observed in stage II (Fig. 4.2).

Fig. 4.13(c) illustrates the growth model of stage III. In this stage, micro-arc discharges are generated. Owing to this "micro-arcing", the film is gradually growing by mainly plasma oxidation and fuse of the substrate material. The roughness increase rate on the 390 alloy surface began to decrease (Fig. 4.10). Since the coating was still thin and the Si-Al-O compounds in the Si-rich regions had a lower melting point and more porosity than the aluminium oxide region, more discharge spots occurred at the silicon-rich regions which resulted in piling up of the Si-Al-O compounds. This feature could be observed in SEM and EDX analysis (Figs. 4.6 and 4.7). Due to more amount of less dense coating microstructure on the high silicon 390 alloy, the voltage increase rate required to breakdown the coating on the 390 alloy was lower than that of the 319 alloy as depicted in Figs. 4.2(a) and 4.2(b).

In the final stage, the coating was fused at the discharge spots and reacted further with the chemical element containing in the electrolyte, causing a more uniform mixture in composition. During the process, coating composite was mainly influenced by electrolyte instead of by substrate underneath the coating. Thus, voltage properties in this stage on both of the alloys were similar as shown in Figs. 4.2(a, b). Small differences in

composition and electrical properties between silicon and aluminium region were exhibited in the stage IV (Figs. 4.8 and 4.9). The coating composition and morphology became even and uniform gradually, which suggested that the silicon content would not have a significant effect at and after the stage IV. Due to the limited maximum voltage 500V, the composition and structure mixing has not achieved completely. From the cross-section microstructure (Fig. 4.12), the localized spheroidal projections and discharge channels occurred at the region of Si phase still can be observed. Nevertheless, the phenomena will not be found at the coatings with thickness more than 50μm produced by a higher voltage (600V), in which the dense layer exhibited a better continuity. Thus, with the growth of dense layer, the effect of Si content of the substrates on surface properties becomes insignificant.

4.3 Summary

The effect of silicon content on the coating process and surface morphology and composition were investigated. With low current density, electrolyte concentration and the maximum 500V voltage, thin PEO coatings (about 10μm in thickness) were produced on the 319 and 390 Al-Si alloys. The coating process was found to have four distinguished stages. In the first three stages, the duration time and morphology of each stage were considerably affected by the silicon content in Al-Si alloys. The micro-arc discharge started to appear at Al-Si interfaces on the alloy surface when the electrical potential reached up to the critical voltage of ~390V for the 319 alloy and ~400 V for the 390 alloy. At the silicon-rich region in the alloys, an Al-Si-O compound with a relatively low melting point formed and it exhibited a porous microstructure comparing with the aluminium rich matrix. The higher silicon content resulted in a rougher coating surface on

the PEO-treated 390 alloy than on the PEO-treated 319 alloy. After the applied voltage was higher than 480V and the process entered stage IV, the composition of the oxide coating for the 319 and 390 alloys were similar. The main phases were γ-Al_2O_3 and a small amount of mullite for both coated alloys. Although the coating on the 390 alloy exhibited a higher surface roughness than the coating on the 319 alloy, the coating surface morphology and roughness are expected to be similar for both alloys when the voltage increases to a higher level (e.g., 600V). The effect of silicon content in a thicker coating (e.g., >50 μm) might not be significant.

CHAPTER 5

EXPERIMENT RESULTS AND DISCUSSION

PART B – EFFECT OF ELECTROLYTIC AND ELECTRICAL PARAMETERS ON PEO COATINGS ON Al-Si ALLOYS

5.1 Results and discussion

5.1.1 Voltage and current variation during the PEO process

The dependencies of anode voltage and current density on PEO treatment time obtained at various preset current densities and electrolyte concentrations (see table 3.2) are shown in Figs. 5.1 and 5.2, respectively. Figs. 5.1(a) and 5.1(b) are the plots of voltage vs. PEO treatment time at the conditions of two electrolyte concentrations (4g/l and 8g/l Na_2SiO_3), respectively; As discussion in chapter 4, the voltage variation was distinguished as four characteristic areas, according to the evidencing changes in the voltage increase gradient, discharge characterization, and surface morphology, which are illustrated by the schematic in Fig. 5.1(c). These regions are characterized as follows. Region I represents the maximum voltage change rate, corresponding to a conventional aluminium anodizing process. In Region II, the rate of voltage increase slackens, indicating a decrease in the oxide film growth rate. In this region, the oxide films are broken down and Si phases were melted partially by high temperature of discharge occurrence. In Region III, micro-arc discharges are generated. Owing to this "micro-arcing", the film is gradually growing by mainly plasma oxidation and fuse of the

substrate material. In final Region IV, the coating was fused at the discharge spots and reacted further with the chemical element containing in the electrolyte, causing a more uniform mixture in composition. In Fig. 5.1(c), the points a, b, c are the critical points between two regions, beyond which the process entered the next stage. At point d, the voltage increased to 500V, this voltage will be constant until the end of the treatment (poin e). T_a, T_b, T_c, and T_d are corresponding treatment time at voltages of a, b, c, and d. Generally, a higher current density would supply a higher electrical field strength and more electric charges within the unit time. Thus, in the same electrolyte the total treatment time is shortened when the current density increases. At the same current density, the process in a higher concentration electrolyte exhibits a lower voltage increase rate than that in a lower concentration electrolyte.

Table 5.1 summarizes the values of critical voltages between two regions and duration time of each region of these processes. In comparison of critical voltage between Region I and Region II (point *a* at Fig. 5.1(c)), and duration of Region I, in the process treated in the 8g/l Na_2SiO_3 electrolyte the critical voltage increased from 385V to 412V when the current density increases from 0.05A/cm^2 to 0.2A/cm^2; with 8g/l Na_2SiO_3 electrolyte, the value of point *a* changed from 384V to 413 V with the variation of current densities. While, at the same current density, the effect of electrolytes on the critical values of point *a* is neglectable. Thus, it indicates that the critical voltage between Region I and Region II is mainly affected by the current density. In 4g/l Na_2SiO_3 electrolyte, the duration of Region I is decreasing proportionally from 60 seconds to 15 seconds with the current density increase from 0.05A/cm^2 to 0.2 A/cm^2. It reveals that under low electrolyte concentration (i.e., 4g/l Na_2SiO_3), the durations of region I with various

current density are followed Faraday's law, which indicates that the oxide film growth rate can be evaluated in the framework of a conventional electrochemical approach. In the high electrolytes (i.e. 8g/l Na_2SiO_3), the durations of Region I are changed from 90 seconds to 30 seconds with the increase of current density but the relation between current density and duration time becomes complex, which implied that film growth is not conventional anodizing but a complex process with dissolution and chemical combination. Point *b* is the critical point between Region II and Region III (Fig. 5.1 (c)), at low electrolyte concentration (4g/l Na_2SiO_3), the value of *b* is about 440V, which is only slightly higher than that of at high electrolyte concentration (8g/l Na_2SiO_3) (~435V). Thus, the effect of electrolyte and current density on the critical voltage between Region II and Region III are weak. According to the conclusions reached from chapter 4, the oxide films, formed in region I, were broken down and Si phases were melted and oxidized partially by high temperature of discharge. Thus, Region II is mainly controlled by substrate material and anodized oxide film characterization formed during region I. A higher current density can supply a higher voltage increase rate, and shortened the duration of region II. However, in higher concentration of electrolyte, dissolution and complex electrochemical combination could lower the efficiency of oxide layer formation and make the duration of region II longer. In the electrolyte of 4g/l Na_2SiO_3, the duration of region II is reduced from 100 seconds to 12 seconds, while in 8g/l Na_2SiO_3, the duration is from 270 seconds to 40 seconds when the current density increases from $0.05A/cm^2$ to $0.2A/cm^2$. From Table 5.1 and Fig. 5.1, it can be noticed that the critical voltage between region III and region IV (point c) is strongly affected by electrolyte concentration. The effect of current density can be neglectable. For 4g/l Na_2SiO_3

electrolyte, value of point c is about 470V; for 8g/l Na_2SiO_3 electrolyte, it is about 450V. Like the region II, the duration of Regions III, and IV increase with the increase of electrolyte concentration and decrease with the increase of current density.

Figs. 5.2(a) and 5.2(b) show the current density variation during the PEO process in the two electrolytes, respectively. In this experiment, after the voltage reach the maximum (500V), the current density will decrease gradually until the system becomes insulated when no more discharge occurs. According Ohm law, under the same voltage, the current density are determined by coating resistance which in some degree can reflect the change of coating material. Fig. 5.2(c) is the schematic of current density variation for different samples. The variation of current density can be roughly distinguished as two stages: rapid changing stage f-g and slow changing stage g-h (Fig. 5.2(c)). While the point *f* indicates the originally preset current density, the point *g* is given with a value of $0.033A/cm^2$ for the endings of all the processes carried out at different treatment parameters. According to the investigation of experiment phenomena, we find that the variation of current density is sensitive to many factors such as the electrolyte temperature, single localized discharge occurrence, current density, and electrolyte.

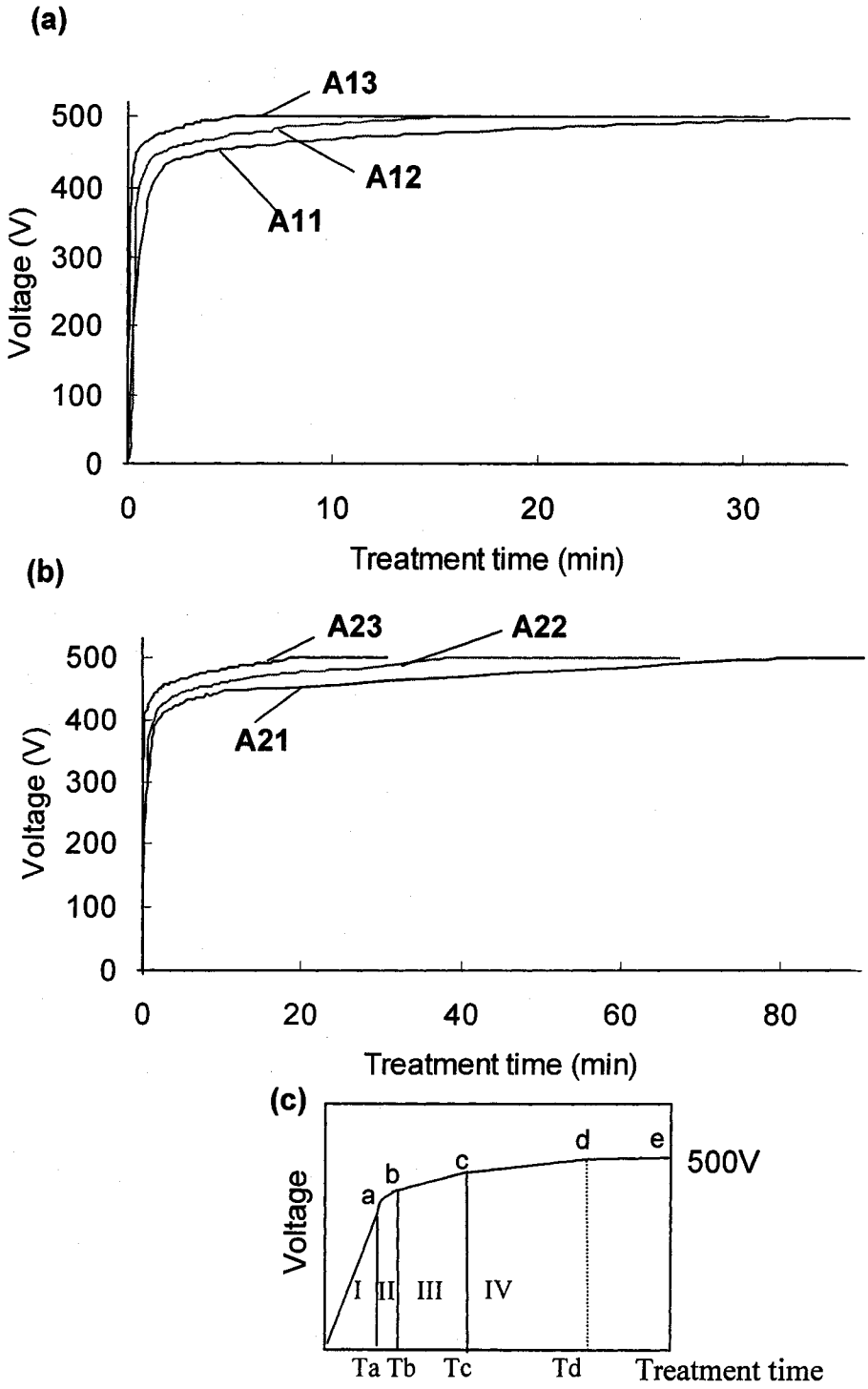

Fig. 5.1 Plots of voltages vs. treatment time during the PEO treatments with electrolyte concentrations (a) 4g/l, and (b) 8g/l; (c) The schematic illustrates the four resolved regions of voltage variation during the PEO process.

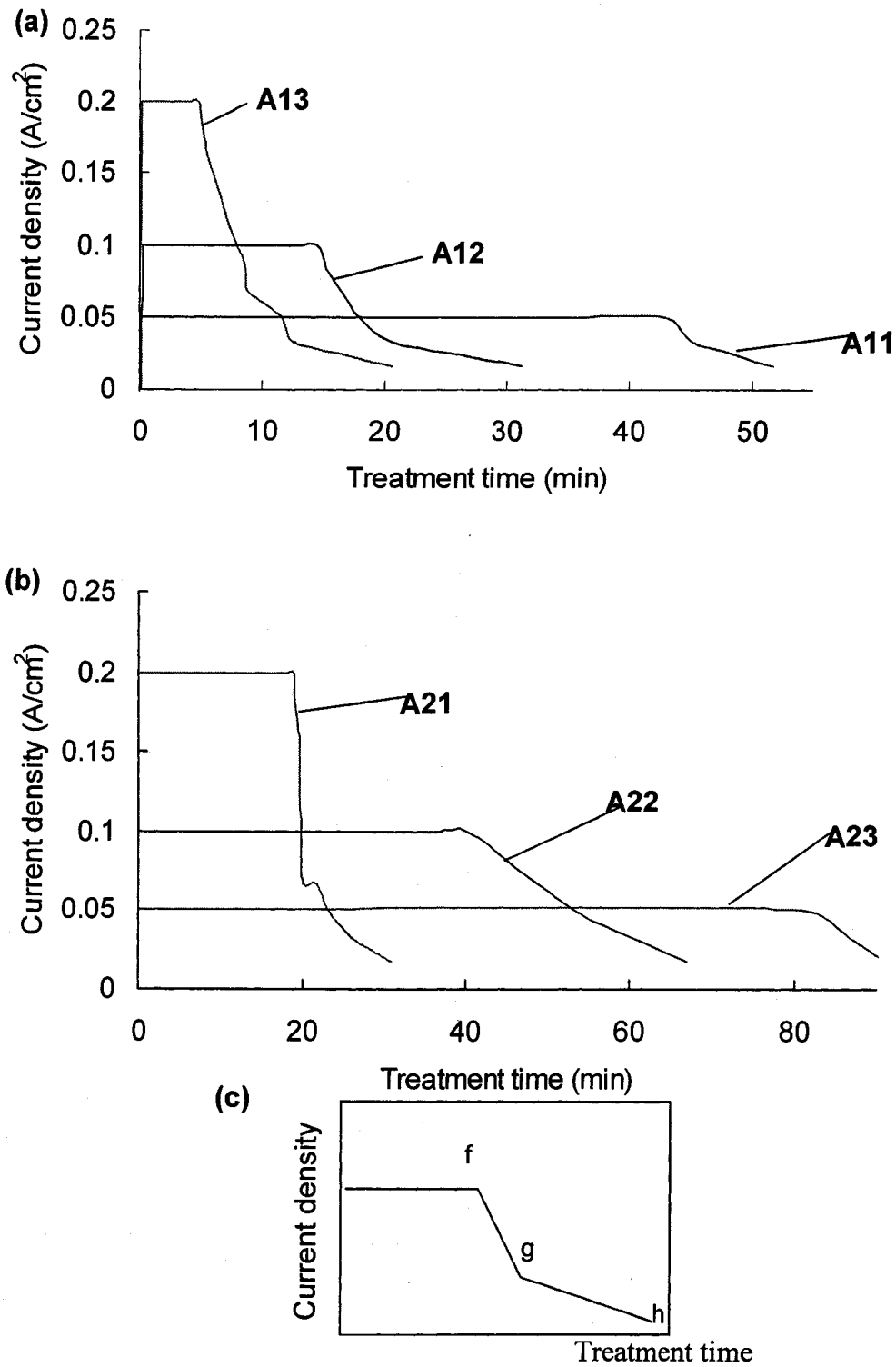

Fig. 5.2 Plots of current density vs. treatment time during the PEO treatments with electrolyte concentrations of (a) 4g/l, and (b) 8g/l. (c) Schematic of current density variation trend.

Table 5.1 Summary of voltage variation characterization

		A11	A12	A13	A21	A22	A23
Stage I	a (V)	385	392	412	384	398	413
	T_a (s)	60	30	15	90	80	30
Stage II	b(V)	441	440	443	433	436	436
	T_b-T_a(s)	100	35	12	270	140	40
	$\frac{\Delta U}{\Delta T}$	0.56	1.37	2.58	0.18	0.27	0.575
Stage III	c(V)	470	472	471	450	455	452
	T_c-T_b(s)	480	225	48	350	170	70
	$\frac{\Delta U}{\Delta T}$	0.06	0.14	0.58	0.048	0.11	0.56
Stage IV	d(V)	500	500	500	500	500	500
	T_d-T_c(s)	1450	625	250	4130	2016	962
	$\frac{\Delta U}{\Delta T}$	0.021	0.0448	0.116	0.012	0.022	0.050
T_d (mins)		34.8	15.3	5.4	80.6	40.1	18.3

5.1.2 Coating structure

Figs. 5.3(a, b, c) are the micrographs of cross-section of coatings produced in 4g/l Na_2SiO_3 electrolyte and at current densities of $0.05A/cm^2$ (A11), $0.1A/cm^2$ (A12), and $0.2A/cm^2$ (A13), respectively. Fig. 5.3(d) is the magnified micrograph of A11 to show the subtle detail of coating structure. All the coatings have a similar structure, i.e. outer layer and inner dense layer at the interface of substrate and coatings. At some regions, the intermediate dense layer is emerged but it is not continuous. The maximum thickness of the dense layer we observed is about 3μm. The out layer is typically porous aspects and about 4μm in thick and some discharge channels go all the way through the outer layer. The inner dense layer is basically uniformed with thickness about 0.8-1μm.

Figs. 5.4(a, b, c) show the cross-section structure of samples A21, A22 and A23 and Fig. 5.4(d) is the magnified cross-section micrograph of sample A21. Compared with Fig. 5.3, a thicker PEO coating can be produced using a high electrolyte concentration at the same maximum voltage. The high concentration electrolyte supplied more Si and O, which accelerates the combination of Al-O in coatings with Si-O in the electrolyte. Compared with Al_2O_3, the Al-Si-O compound has a low electrical resistance and low breakdown voltage. Thus, at relatively low voltage, plasma reaction can still perform, which in turn enhances the compound formation. The thickness of outer layers of A21, A22 and A23 are all similar about 10-15μm. At the $0.05A/cm^2$ current density, a relatively thick (thickness: 1-5μm), dense layer can be observed in the cross-section structure (Fig. 5.4(a)). But at a higher current density, the denser layer becomes thinner and somewhere incontinuous. The mechanism of formation of dense layer is known that

with coating thickness increasing, thermal conductivity decreases, which provokes the γ-Al_2O_3 transformation to α-Al_2O_3. At high current density, the discharges are more intensive than that at low current density and could deduct that more oxidized aluminium is ejected from the discharging channels towards the coating surface in touch with the electrolyte. The process at condition of high current density allows the outer layer to grow fast and only thin intermediate dense layer formed. It is interesting to notice that the thickness of inner dense layer is still about 0.8-1μm.

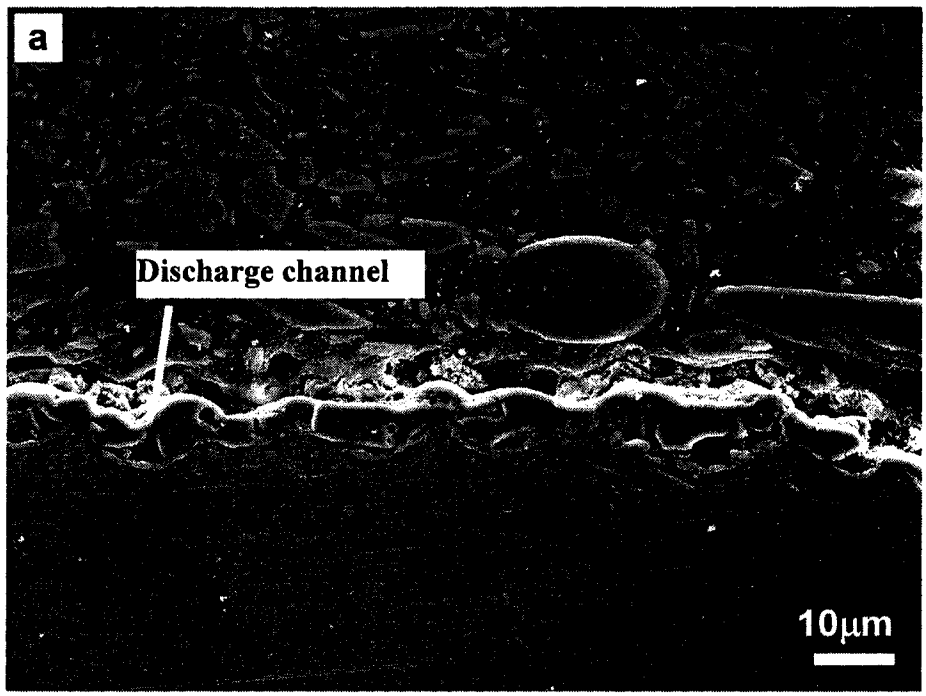

Fig. 5.3(a)

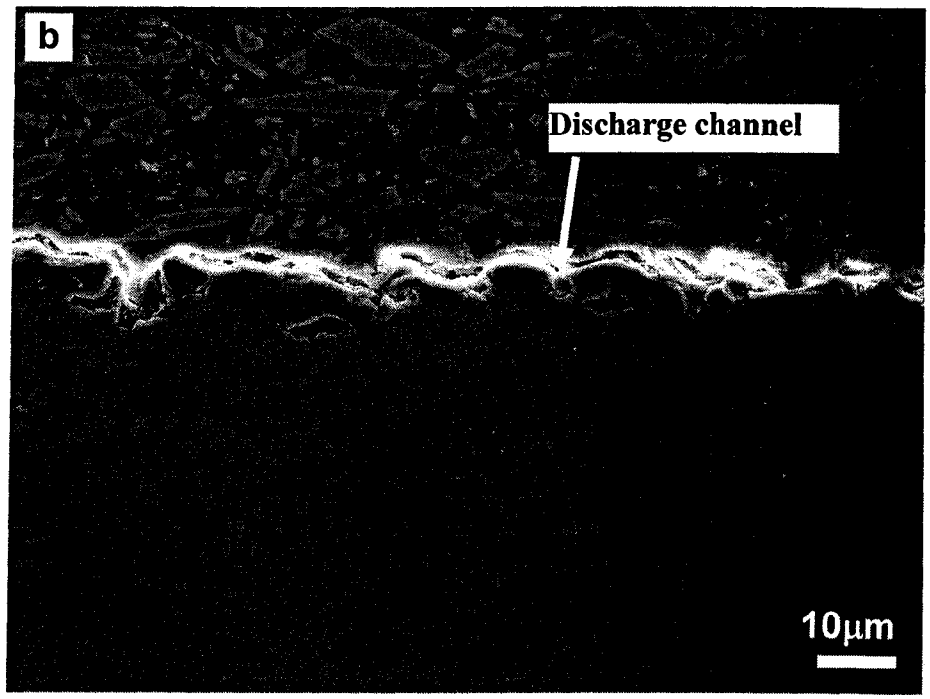

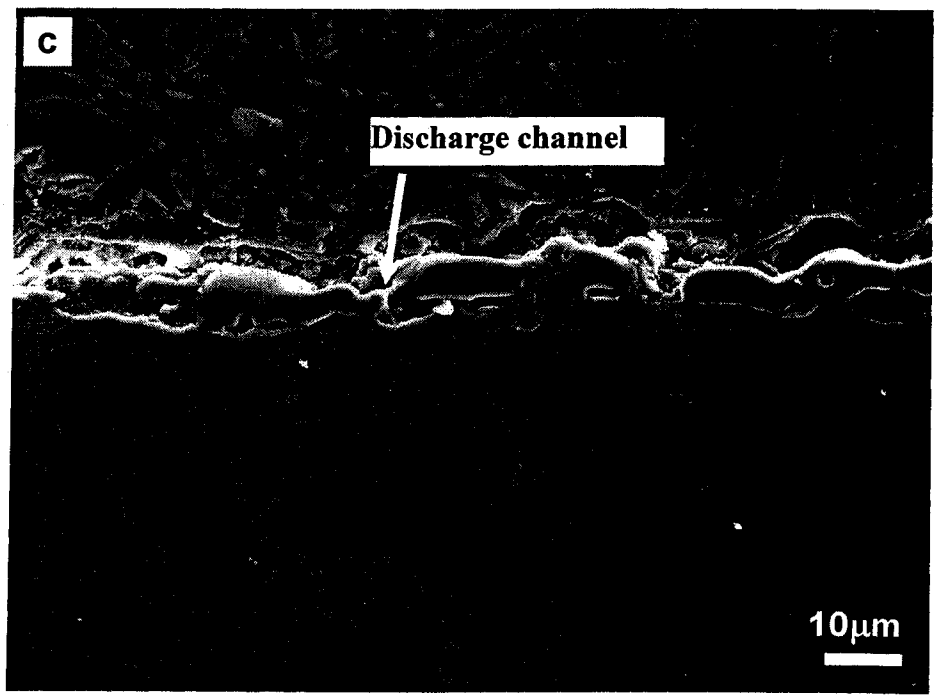

Fig. 5.3(b, c)

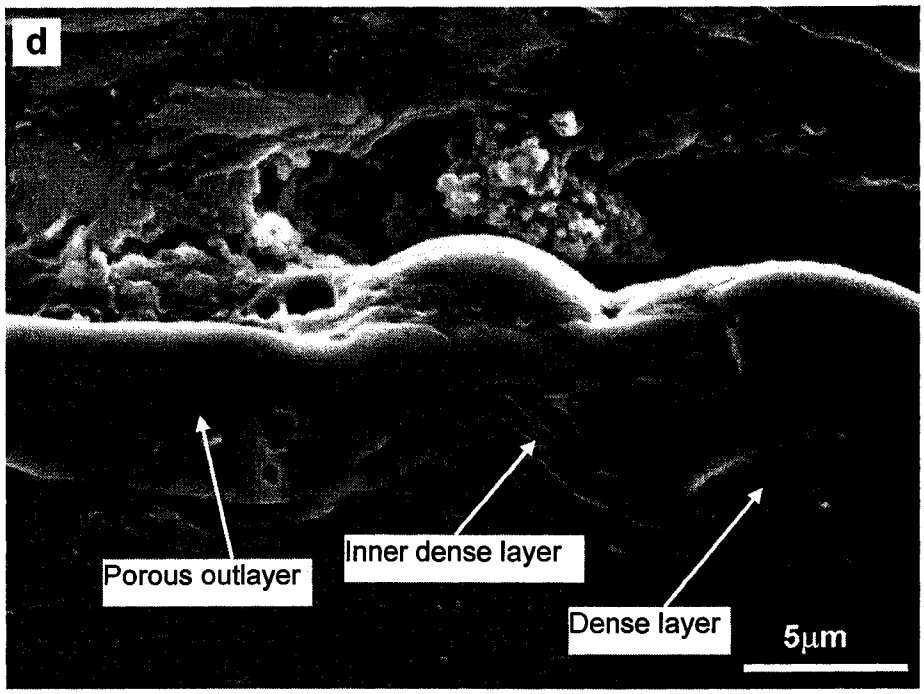

Fig. 5.3 SEM micrographs of cross-section structures of samples (a) A11, (b) A12, (c) A13, and (d) the magnified cross-section micrograph of A11.

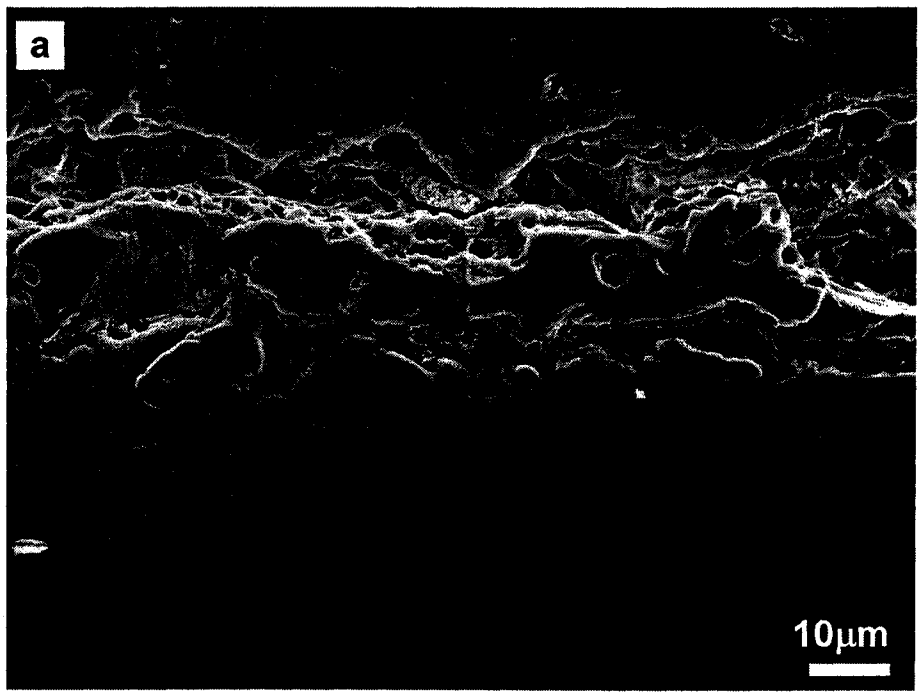

Fig. 5.4(a)

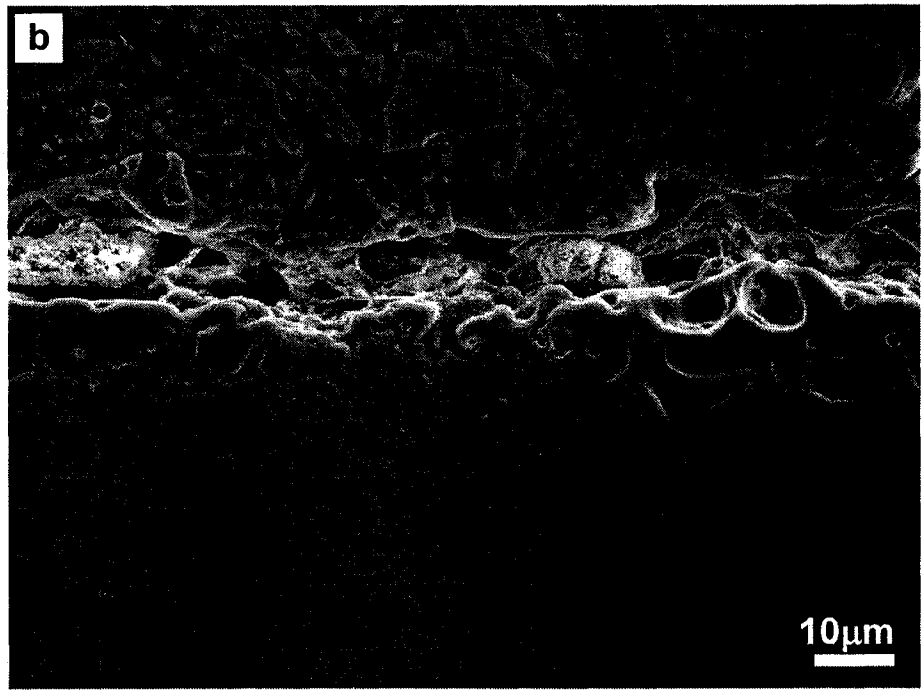

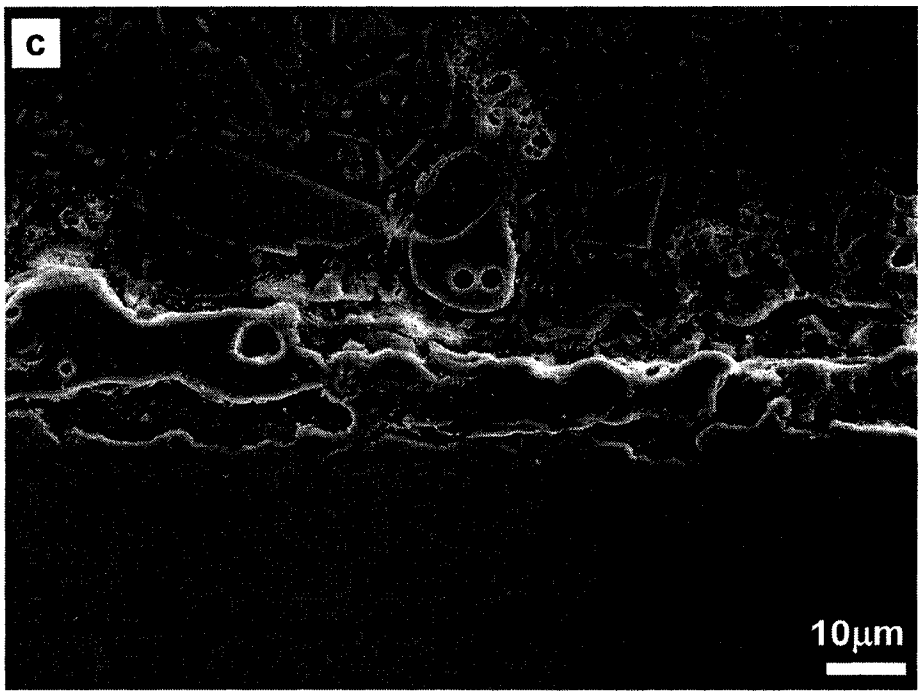

Fig. 5.4(b, c)

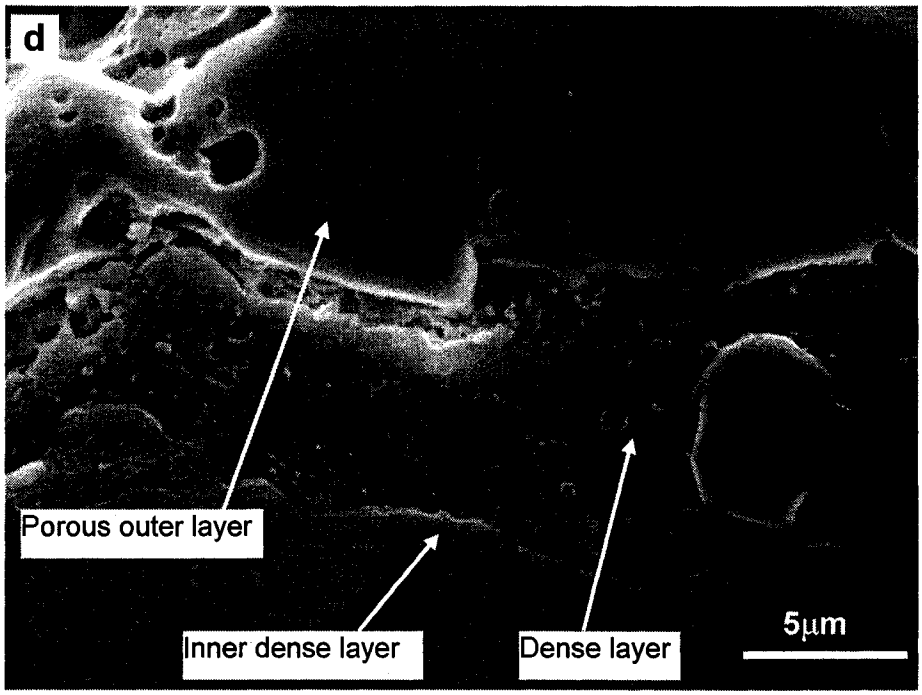

Fig. 5.4 SEM micrographs of cross-section structures of samples (a) A21, (b) A22, (c) A23, and (d) the magnified cross-section micrograph of A21.

5.1.3 Surface morphology

Fig. 5.5 shows the surface morphology of coatings deposited in 4g/l Na_2SiO_3 electrolyte with different current densities. Figs. 5.5 (a, c, e) show the surface morphology of coatings A11, A12 and A13, respectively. To show surface morphology of oxide coatings in detail, magnified micrographs of the corresponding samples presented in Figs. 5.3(b, d, f). Qualitatively, the three coatings have the similar surface morphology, i.e., oxide coatings with circle or elliptical pores.

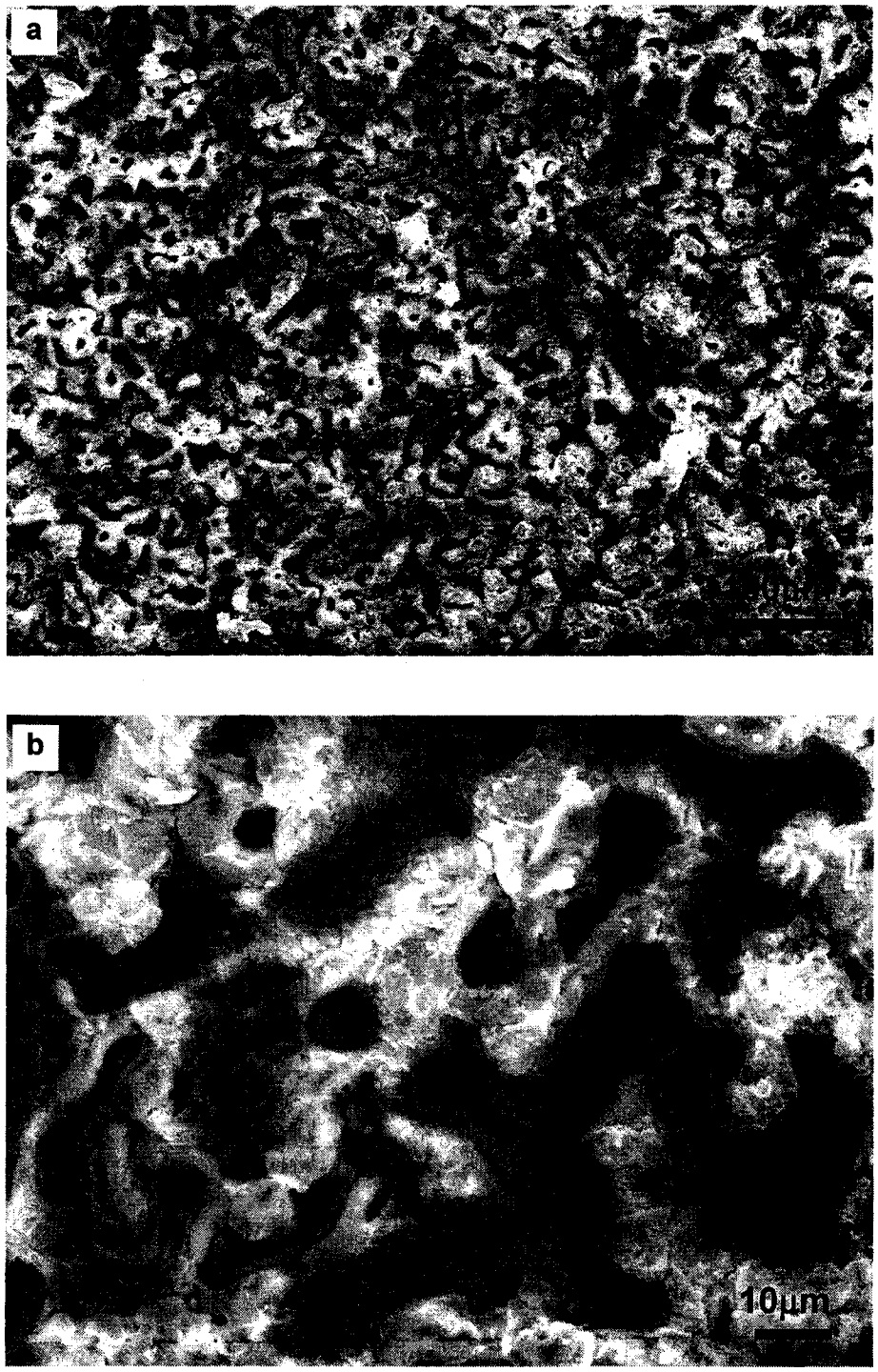

Fig. 5.5 Micrographs of surface morphology of sample A11: (a) x200 and (b) x1000.

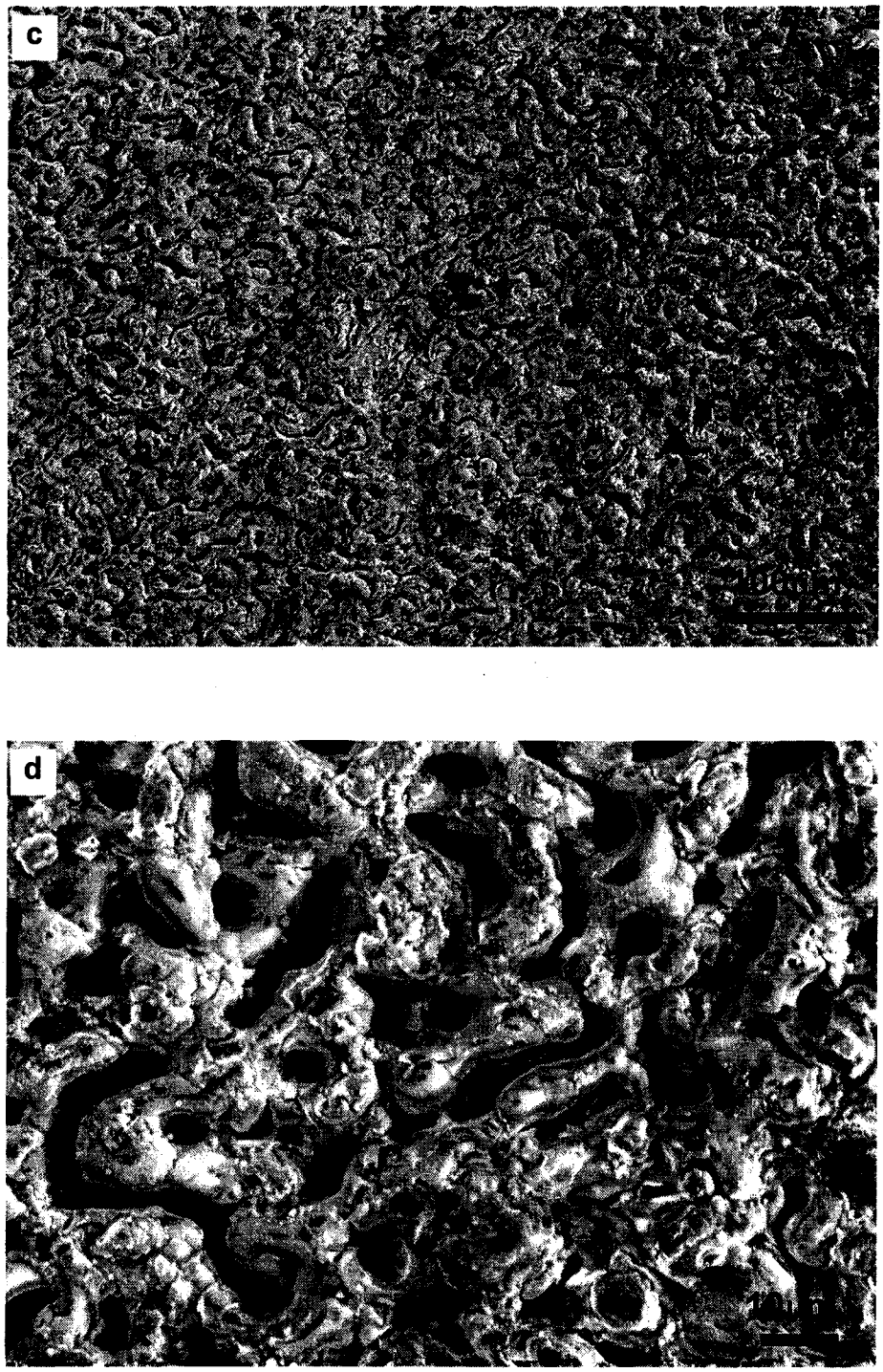

Fig. 5.5 Micrographs of surface morphology of sample A12: (c) x200 and (d) x1000.

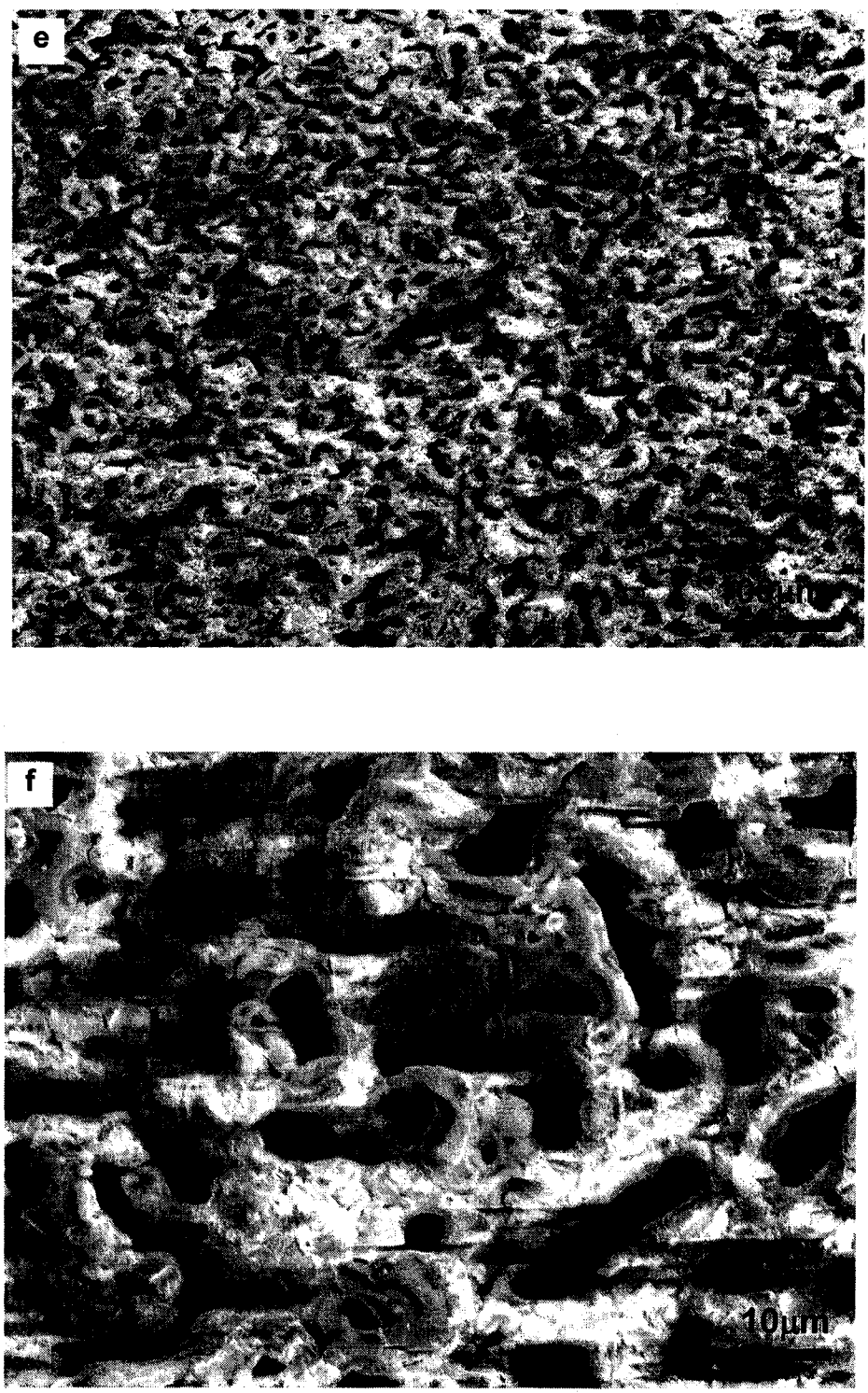

Fig. 5.5 Micrographs of surface morphology of sample A13: (e) x200 and (f) x1000.

Fig. 5.6 shows the surface morphology of coatings deposited in the 8g/l Na_2SiO_3 electrolyte with different current densities. The low magnification micrographs (Figs. 5.4(a, c, e)) show the surface morphology of coatings A21, A22, and A23. Figs. 5.4 (b, d, f) are the corresponding high magnification micrographs. Compared with the coatings deposited in the low concentration electrolyte (4g/l Na_2SiO_3), the surface projections are coarse and the size of projections is much larger. Obviously, the number of pores (i.e., porosity) is less than that of the coating produced in the 4g/l Na_2SiO_3 electrolyte, and the pores are mainly circular.

Figs. 5.5 and 5.6 indicate that coatings deposited in the same electrolyte but different current densities, still have a similar surface morphology. To identify the surface distinction quantitatively, the surface profiles of coatings produced by various electrolyte and electrical parameters were analyzed and compared. Figs. 5.7(a-f) present the typical surface profiles of coatings A11, A12, A13, A21, A22, and A23. At the methods described in chapter 3, the size of projections is calculated and summarized in Table 5.2.

Table 5.2 Size of projections and roughness of coating surfaces

Samples	Average size of projection (mm)	Roughness (Ra) (μm)
A11	0.014523	1.79
A12	0.015392	1.82
A13	0.016734	1.88
A21	0.035836	5.87
A22	0.038346	6.06
A23	0.045522	6.35

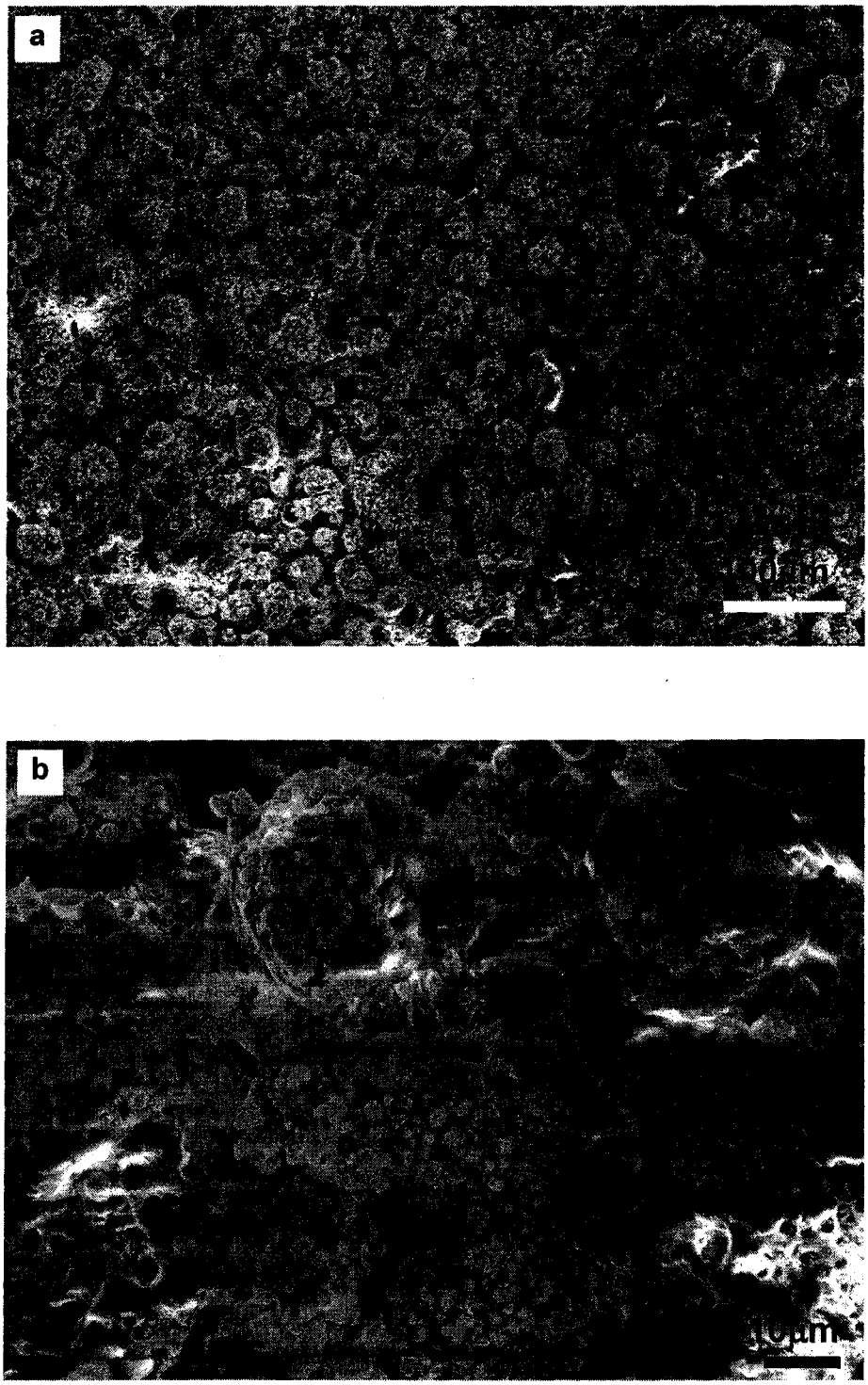

Fig. 5.6 Micrographs of surface morphology of sample A21: (a) x200 and (b) x1000.

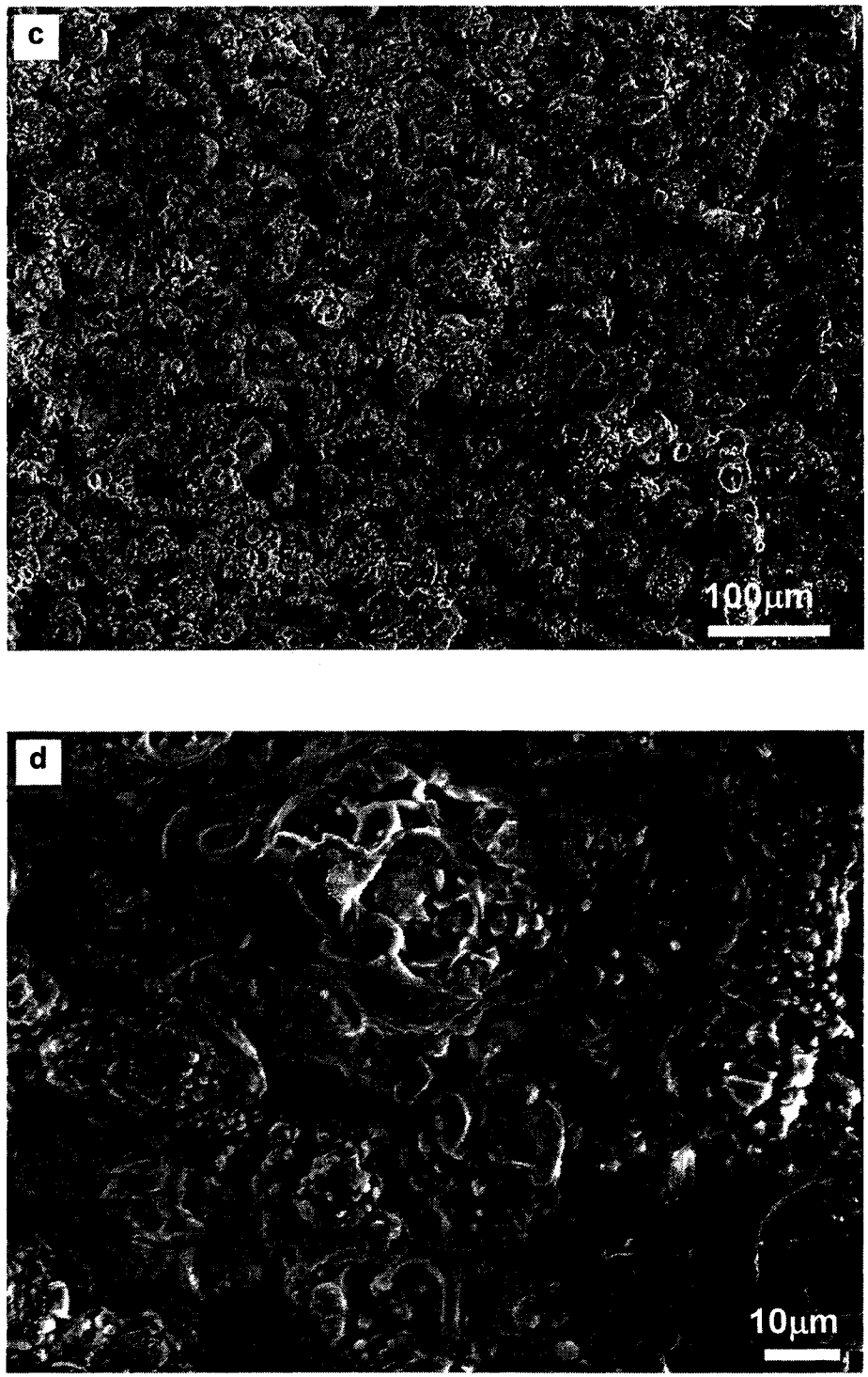

Fig. 5.6 Micrographs of surface morphology of sample A22: (c) x200 and (d) x1000.

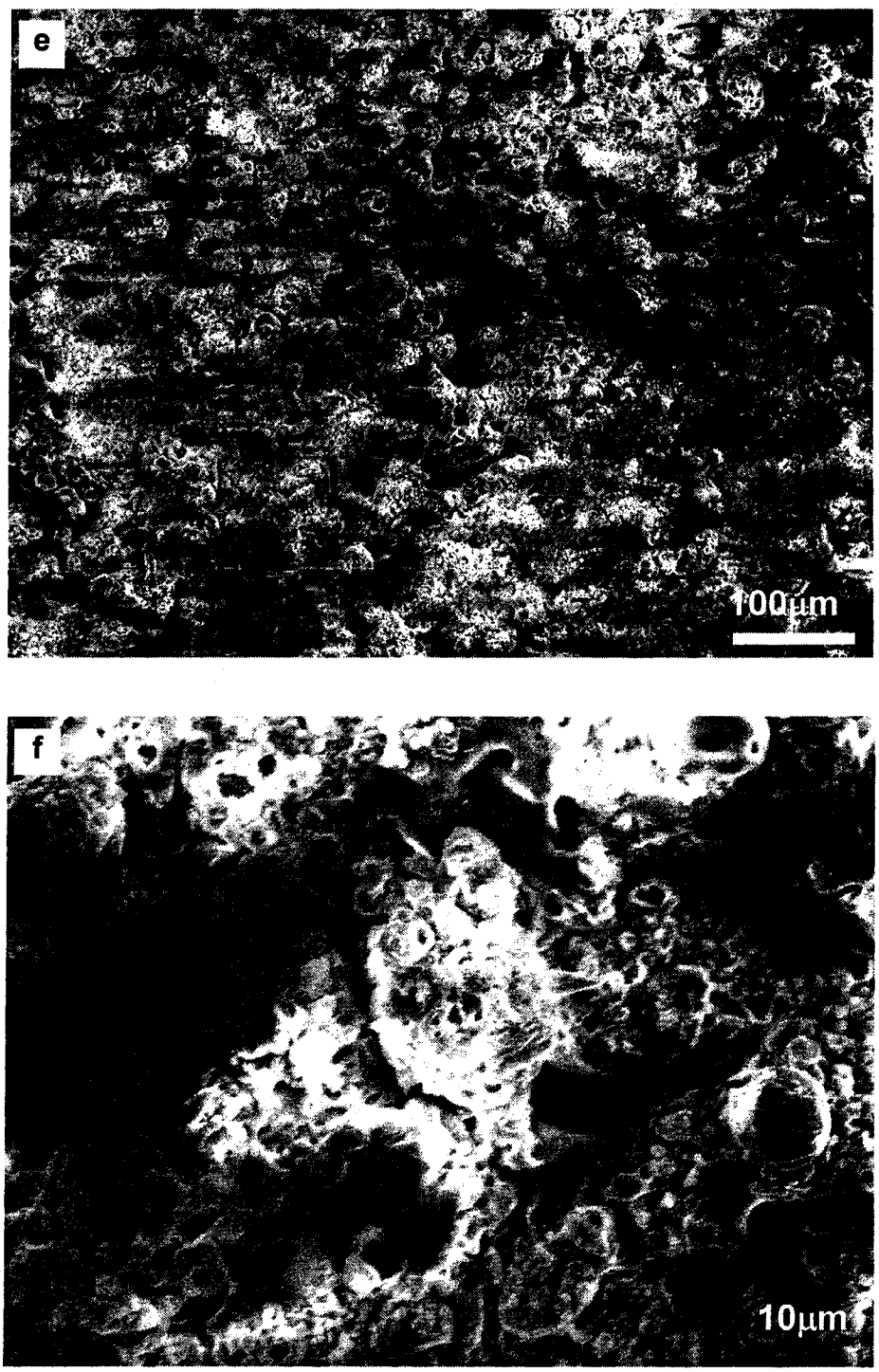

Fig. 5.6 Micrographs of surface morphology of sample A23: (e) x200 and (f) x1000.

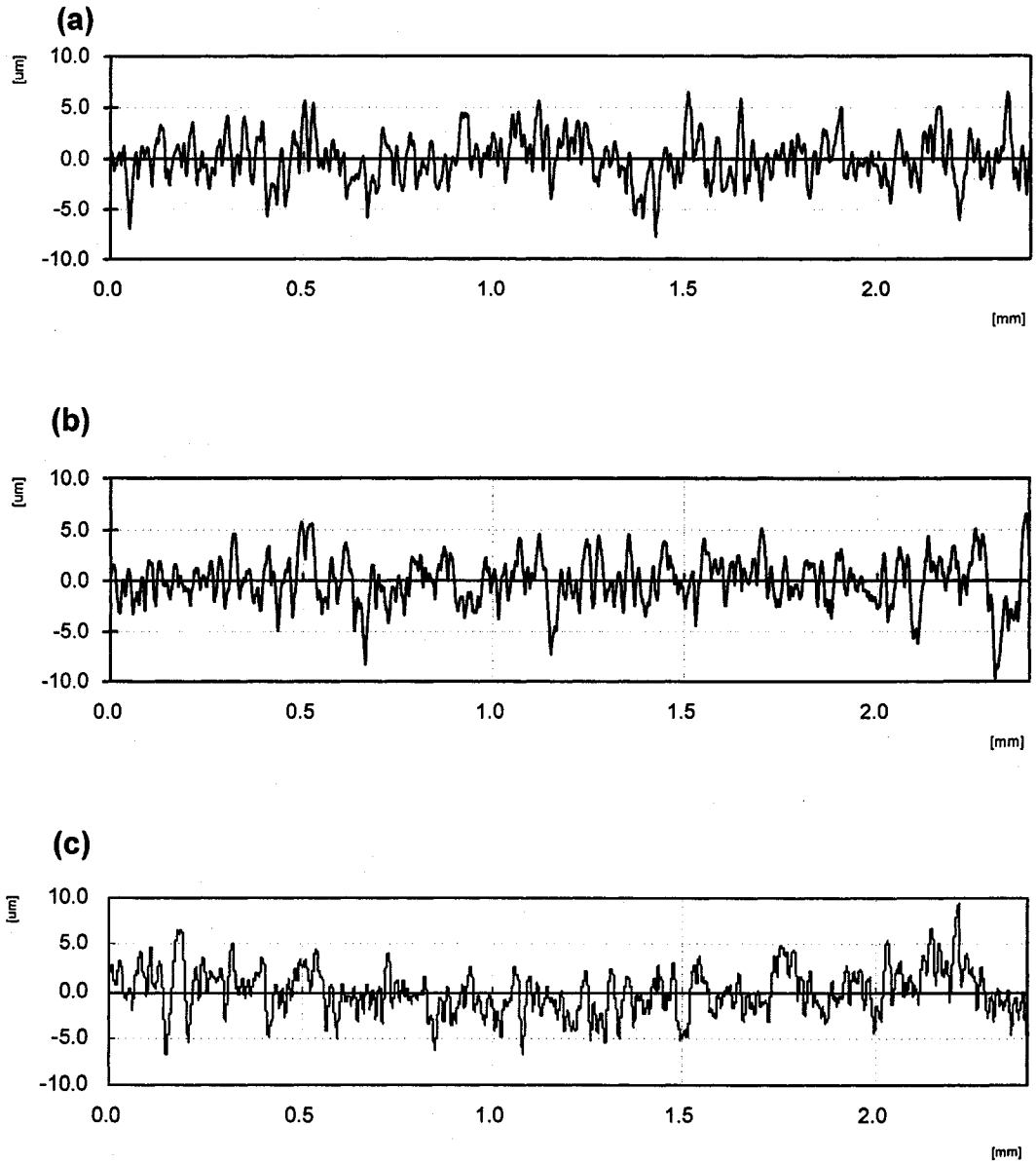

Fig. 5.7 The plots of typical surface profiles of samples: (a) A11, (b) A12, and (c) A13.

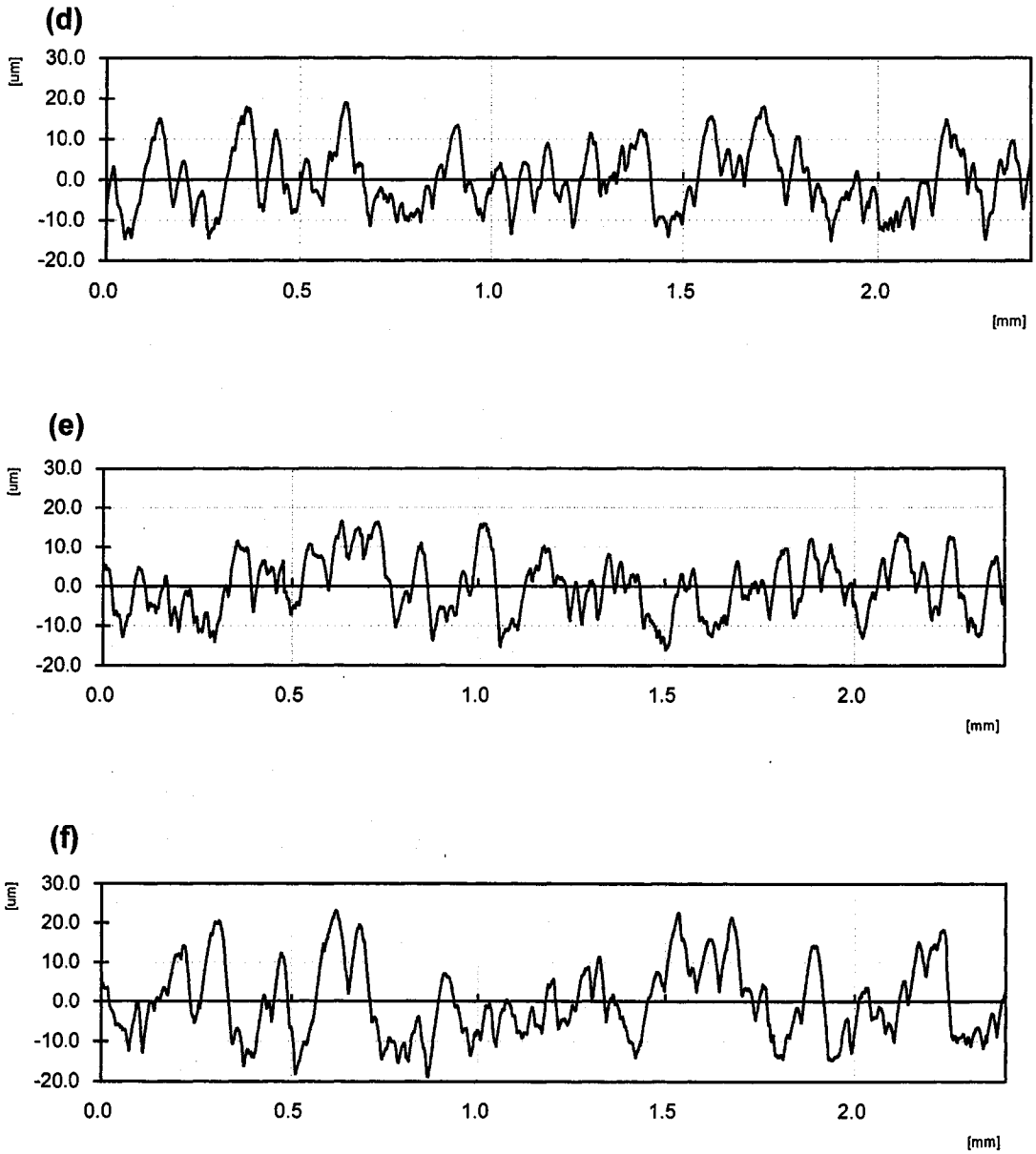

Fig. 5.7 The plots of typical surface profiles of samples: (d) A21, (e) A22, and (f) A23.

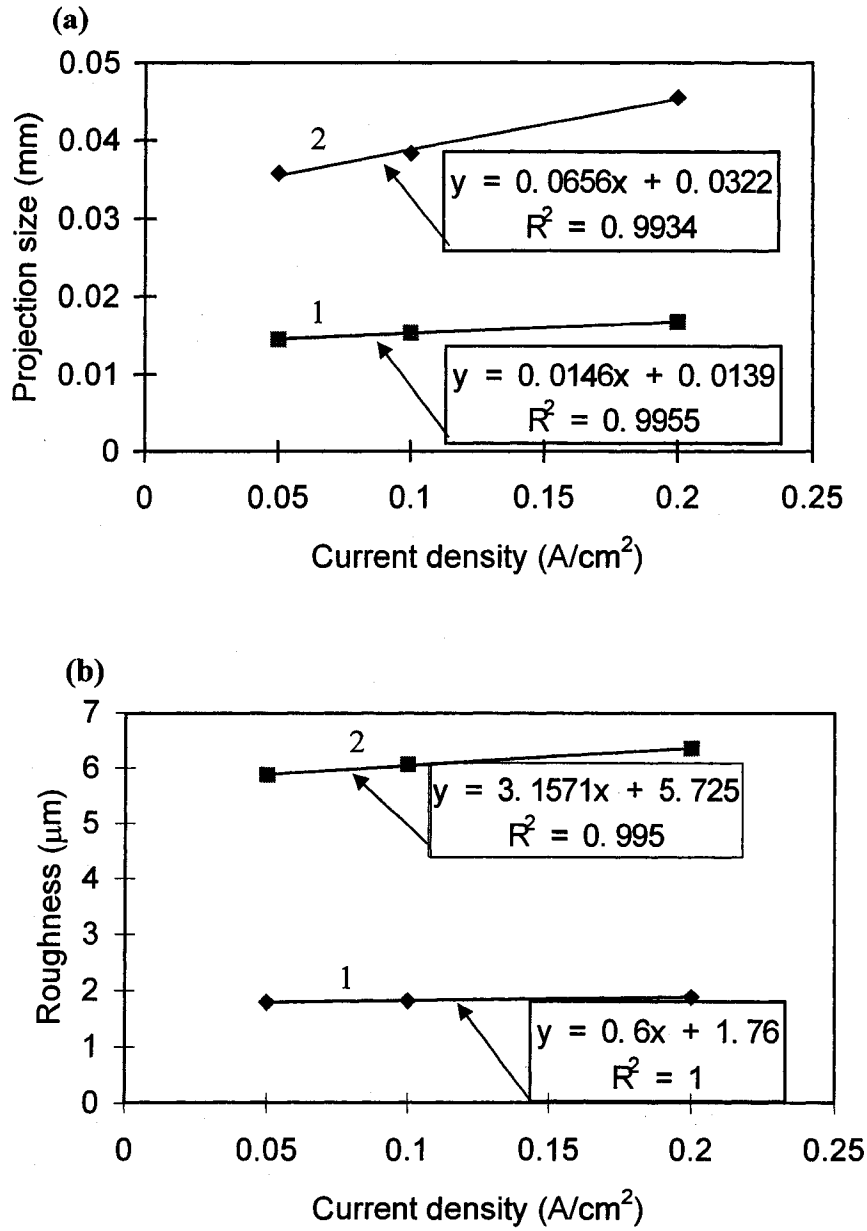

Fig. 5.8 Relationships of surface morphology vs. electrolyte concentration and current density. (a) Surface projection size vs. current density and (b) surface roughness vs. current density.

Figs. 5.8(a, b) show relationships of surface morphology vs. electrolyte concentration and current density. In those plots, line 1 and line 2 are corresponded to the

coatings prepared by 4g/l and 8g/l Na_2SiO_3 electrolyte and the equations, and reliability of the trend lines are shown in the insets in Figs. 5.8(a, b). Figs. 5.8(a) illustrates the relationship of projection size vs. electrolyte concentration and current density. The data in Table 5.2 and Fig. 5.8(a) indicate that the oxide projection size on thick coating surfaces (A21, A22 and A23) linearly increased with current density from 35μm to 45μm. The thin coatings (A11, A12 and A13) have a much smaller feature size and with the current density change from 0.05A/cm^2 to 0.2A/cm^2, the size only linearly increases from 14μm to 16μm.

The surface roughness of the coatings is also listed in Table 5.2. Fig. 5.8(b) presents the relationships of surface roughness vs. electrolyte concentration and current density. Fig. 5.8(b) indicates that the coatings produced using the high electrolyte concentration have much rougher surfaces than those by use of low electrolyte concentration. The roughness of former is around 6μm and latter is about 1.8 μm. For coatings prepared in 4g/l electrolyte, the surface roughness linearly increased from 1.79μm to 1.88μm with current densities from 0.05A/cm^2 to 0.2A/cm^2. However, surface roughness of coatings treated in 8g/l electrolyte linearly increased from 5.87 to 6.35 for the same range of current density increasing. Thus, the electrolyte concentration has a significant effect on surface roughness. However, the current density does not appear to have a strong effect on the roughness and projection size when the coatings are prepared in a given electrolyte.

5.1.4 Hardness

The hardness of the coatings was measured on the coating cross-sections by a Vickers hardness tester. The results are shown in Fig. 5.9. The coating hardness is at the range of 800-1000. The coatings produced in the high Si electrolyte have a lower hardness than those of in the low concentration electrolyte. The current density has a slight effect on coating hardness.

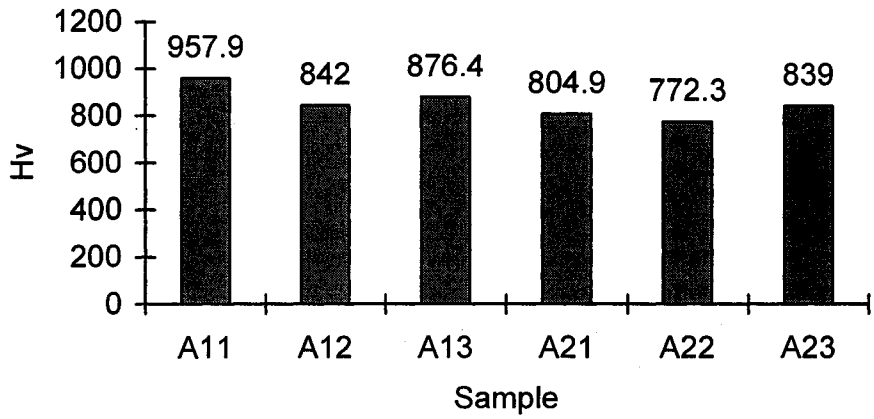

Fig. 5.9 Hardness of cross-section

5.1.5 XRD

Figs. 5.10 (a, b, c) are XRD-patterns of samples A11, A12 and A13. The main phases are γ-Al_2O_3 plus a little amount of α-Al_2O_3 and some Al-Si-O phases. Figs. 5.11 (a, b, c) show XRD-patterns of samples A21, A22 and A23. Compared with the XRD patterns of coatings A11, A12 and A13 (shown in Fig. 5.10), besides γ-Al_2O_3 and α-Al_2O_3, Al_2O_3-SiO_2 phases can be detected. Moreover, from 10-30 degrees, a lot of unidentified peaks with a wide shoulder exist, which could result from an amorphous Al-Si-O glassy phase in the coatings.

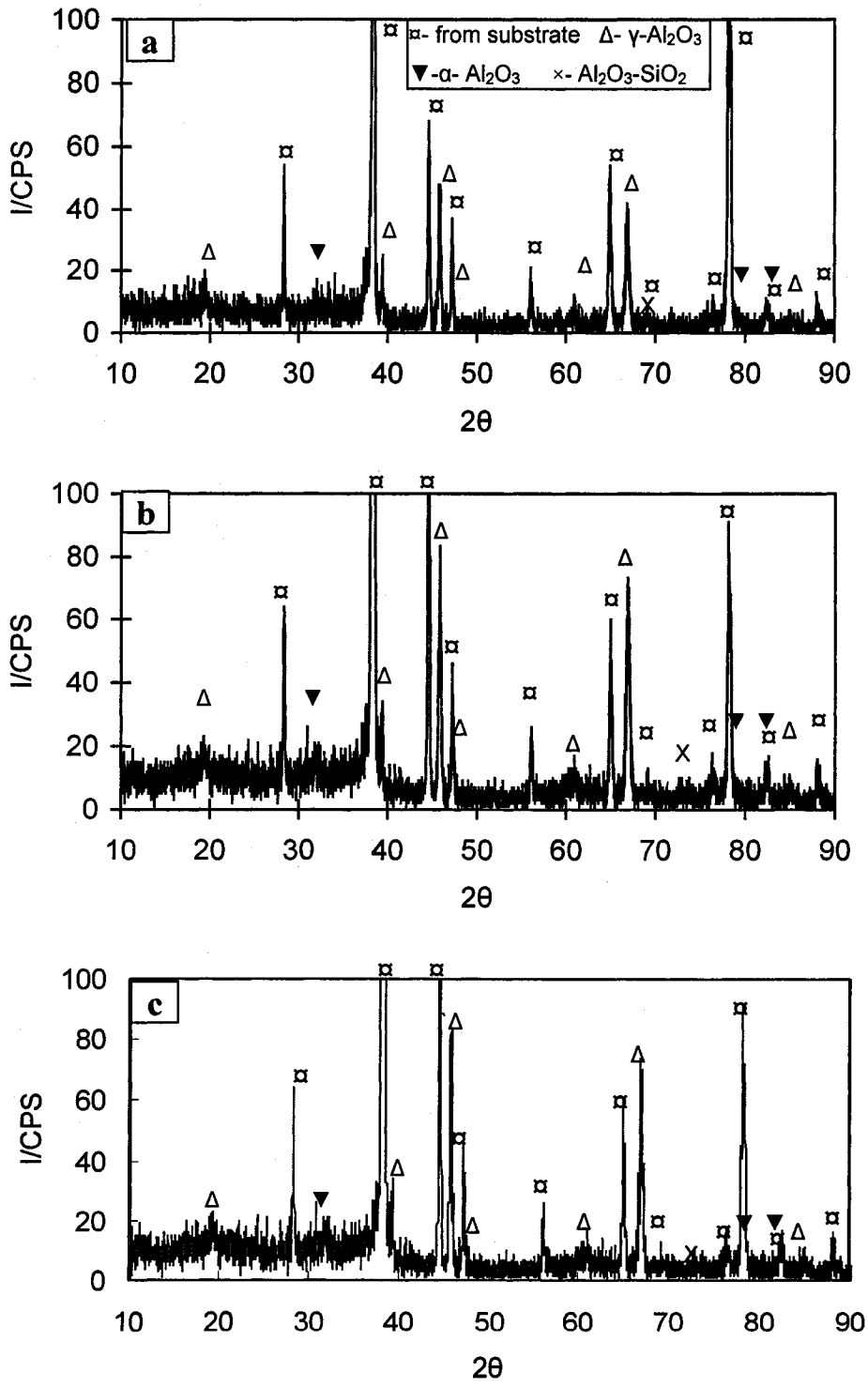

Fig. 5.10 XRD-patterns of samples: (a) A11, (b) A12, and (c) A13.

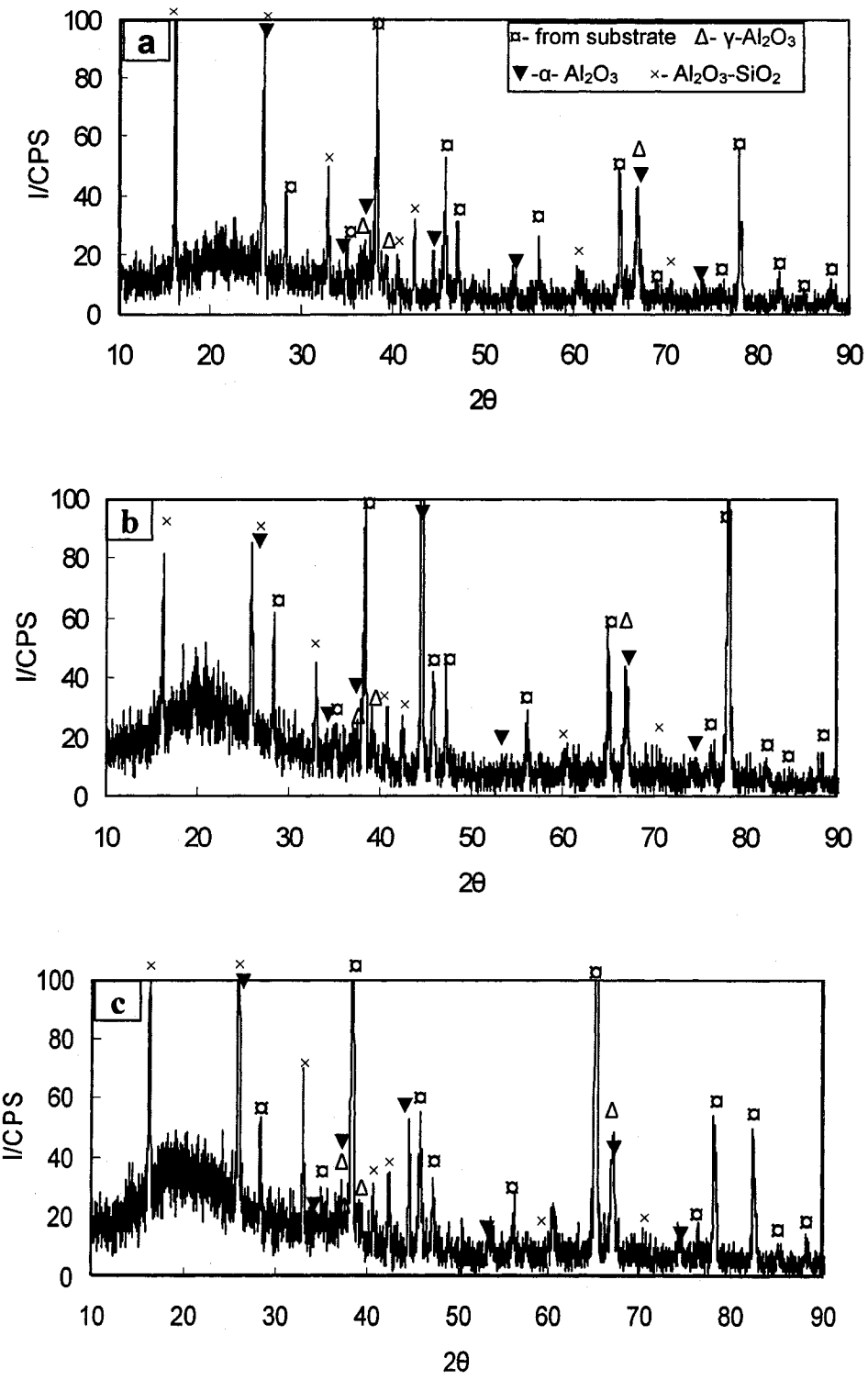

Fig. 5.11 XRD-patterns of samples: (a) A21, (b) A22, and (c) A23.

5.2 Summary

The PEO process using a higher concentration electrolyte can produce a thicker oxide coating. The thickness of coatings deposited in 4g/l Na_2SiO_3 with the maximum 500V voltage is about 10μm and the coatings is composed of an outer layer, non-continuous dense layer and inner dense layer. The phase composition of the thin PEO coating is mainly γ-Al_2O_3. The PEO coating prepared in an 8g/l Na_2SiO_3 electrolyte has a larger thickness (20-25 μm) and the coating appears to have a continuous dense layer in the between of outer porous layer and inner dense layer. It was also found that the coating deposited in the high concentration electrolyte has more amounts of Al_2O_3-SiO_2 compound phases, and also α-Al_2O_3 phase. Although the coating phase composition is different, the hardness of the coatings deposited by different parameters is all in the range of 800-1000 HV. The coatings treated by the higher concentration electrolyte have slightly lower hardness than that of in low concentration electrolyte. The current density effect on coating structure, and coating hardness was not found to be significant. However, with the current density increase, the surface morphology change increased due to the oxide projection size increase, which could result from intensive discharge occurrence under higher current density.

CHAPTER 6 EXPERIMENT RESULTS AND DISCUSSION

PART C – OXIDE-GRAPHITE COMPOSITE COATING

6.1 Results

6.1.1 Morphology of oxide-graphite composite coatings

Fig. 6.1 is SEM micrographs of surface morphology of composite coatings: AG12 (Fig. 6.1(a)) and AG22 (Fig. 6.1(b)). Fig. 6.1(c) is the EDX spectra corresponding to regions *i* and *ii* on AG12 surface which show element compositions of a typical oxide-graphite composite coating. Graphite (region *ii*) was embedded into the pores (region *i*) on the PEO outer layer. Graphite covers about 60% and 70% surface areas of samples AG12 and AG22, respectively. The rough surface profile of the PEO coating with pores is believed to provide the graphite with anchors, and then graphite were embedded in the top layer of the composite coating during the subsequent localized plasma discharge. The size of oxide projections and pores on the AG22 sample is much larger than that of on sample AG12, which provides the graphite with more preferential anchor sites. Thus, a more graphite coverage appears on the surface of sample AG22 than sample AG12.

Fig. 6.2 shows cross-sectional structures of composite coatings AG12 (Fig. 6.2(a)) and AG22 (Fig. 6.2 (b)). The composite coating has a cross-sectional morphology similar to a typical PEO coating structure, i.e. porous outer layer, intermediate dense layer and inner dense layer. It is believed that graphite-oxide mixture occurs mostly in the top outerlayer. The graphite may be peeled off at the polishing process during the cross-section sample preparation. The cross-section structure in Fig. 6.2(a) shows that the

average thickness of this composite coating AG 12 is about 12μm, among which outlayer is about 9 μm thick i.e., 75% of total coating thickness. Within the outerlayer, the thickness of oxide-graphite composite toplayer is about 1-2μm. Fig. 6.2 (b) is the cross-section micrograph of composite coating AG22, which indicates that the average thickness of this composite coating AG22 is about 25μm. The outer layer with about 5μm oxide-graphite composite layer as its top layer is approximately 15 μm thick, i.e., 60% of total coating thickness.

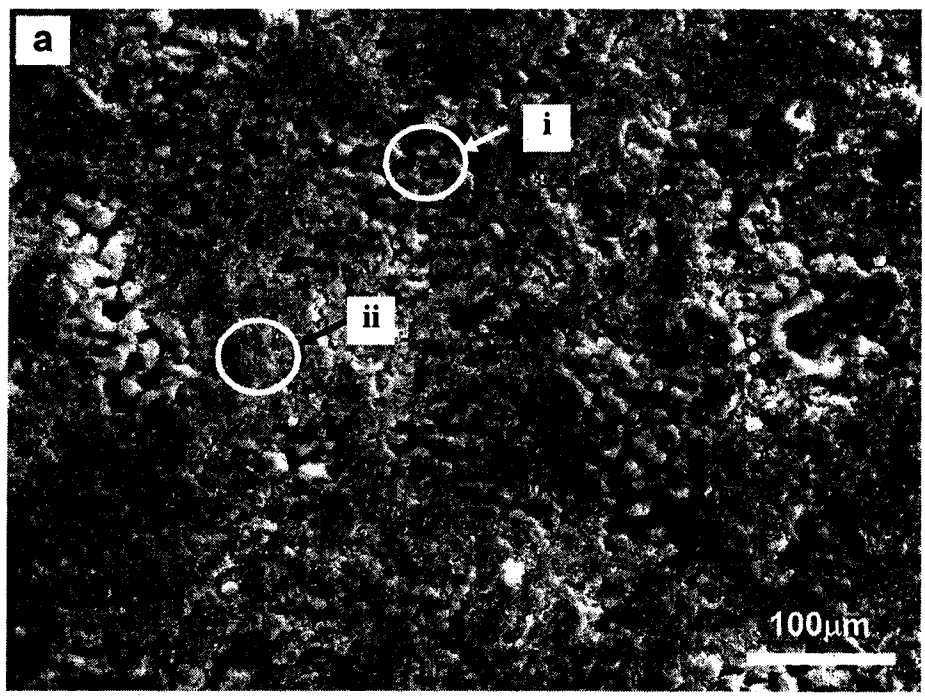

Fig. 6.1(a)

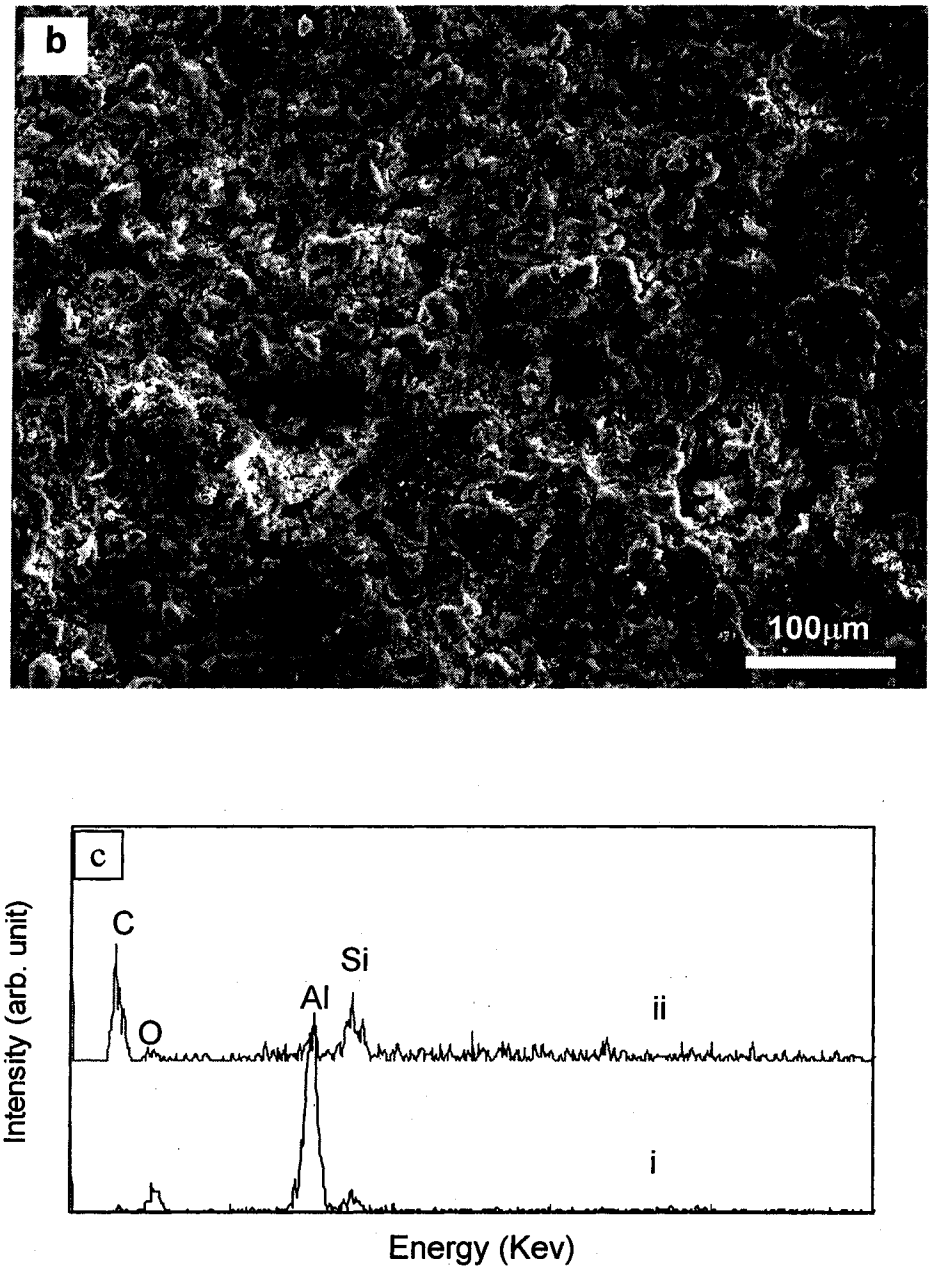

Fig. 6.1 SEM micrographs of surface morphology and EDX spectra of oxide-graphite composite coatings. The typical surface morphology of composite coatings: (a) AG12 and (b) AG22. (c) EDX spectra of corresponding regions i and ii on the AG12 surface.

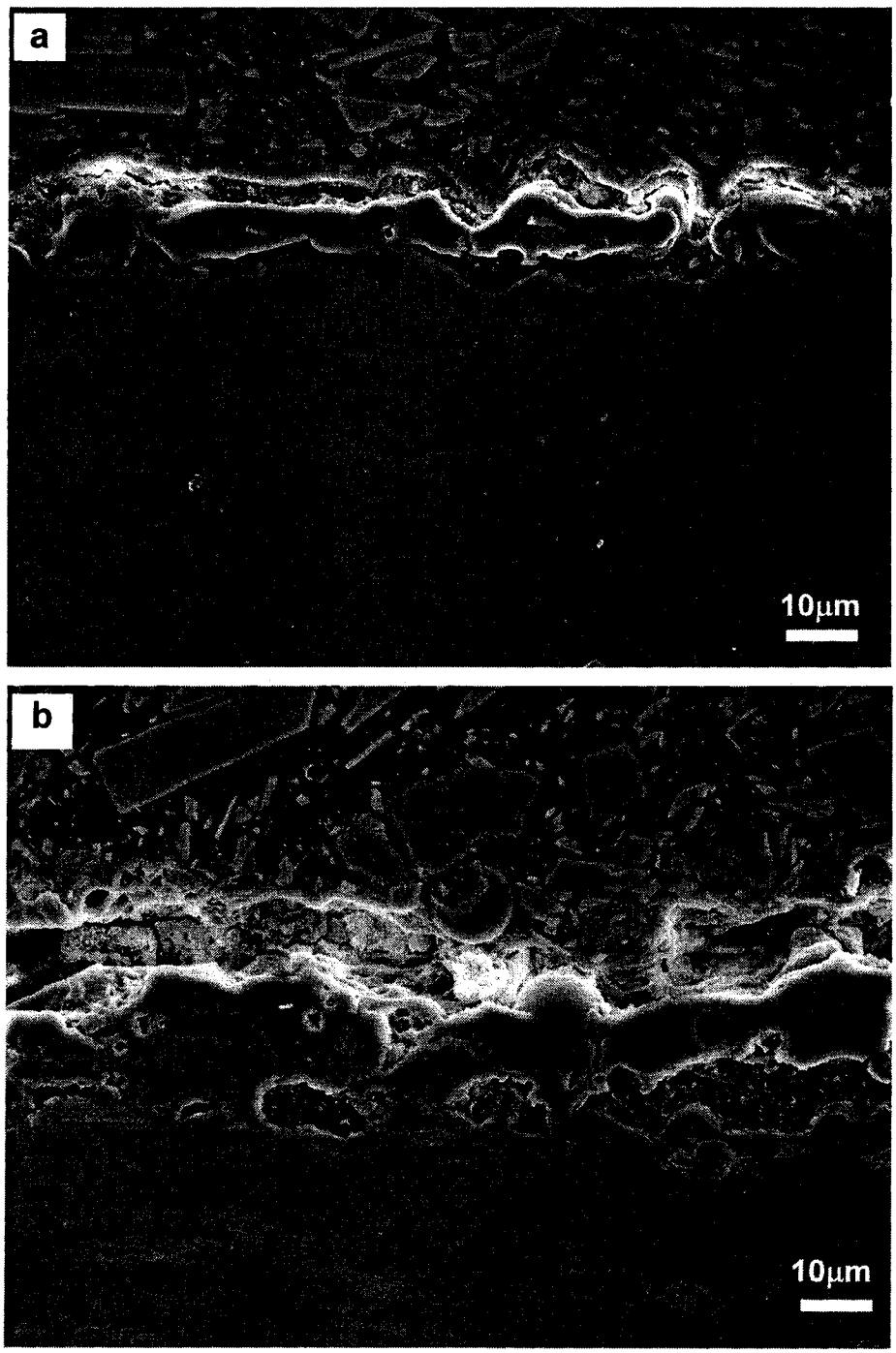

Fig. 6.2 SEM micrographs of cross-section structures of oxide-graphite composite coatings. (a) AG12 and (b) AG22.

Table 6.1 Roughness and microhardness (Vickers hardness) of the PEO oxide and oxide-graphite composition coatings

Samples	Roughness (μm)	Hardness of top layer (from cross-section)
A12	2.01	842.0
AG12	1.82	876.0
A22	6.06 (polished to 2.10)	772.3
AG22	2.80(polished to 2.10)	839.0

Surface roughness of the PEO oxide (A12 and A22) and composite (AG12 and AG22) coatings is listed in Table 6.1. The as-deposit surfaces of composite coatings have lower surface roughness than that of oxide coatings; especially for thick coatings A22 and AG22, the roughness of as-deposit surfaces reduced from 6μm to less than 3μm. As described in chapter 5, the rough surface of A22 resulted from the coarse Al-Si-O projections, which is produced by reaction between coating material and high concentration electrolyte. The rubbing of graphite during preparation of the composite coatings can also rub off the loosen oxide particles and graphite fills into the pores, making the coating surface smoother. Thus, the composite coatings have a much lower roughness than the corresponding oxide PEO coatings.

6.1.2 Hardness of the coatings

Table 6.1 also lists microhardness of the PEO oxide coatings (A12 and A22) and composite coatings (AG12 and AG22). The Vickers hardness of coatings is in the range from 700 to 900. The hardness of the thin coatings (A12 and AG12) is slightly higher than that of thick coatings (A22 and AG22). Table 6.1 shows that the composite coatings

(AG12 and AG22) have a higher hardness than the corresponding oxide coatings (A12 and A22). The increased hardness for AG12 and AG22 may result from their thicker and denser top layers compared with A12 and A22.

6.1.3 Tribological properties

6.1.3.1 Tribological behaviors under dry sliding tests

The pin-on-disc tribological tests were conducted for investigation of tribological behaviors of the composite coatings. Before the pin-on-disc test, the coated sample surfaces were polished to roughness 2±0.2 μm (see Table 6.1). For comparison, uncoated Al alloy and the PEO oxide coatings were also tested.

Fig. 6.3 presents the variation of the coefficient of friction of uncoated 319 Al-Si alloy substrate under dry sliding condition. At the beginning, i.e., a break-in stage [69], the coefficient of friction (C.O.F) was high, above 1.2. With increase in sliding distance, the C.O.F reduced gradually with localized fluctuation. After 4000 revolutions, the C.O.F is reduced to 0.8. Then from 4000 revolutions to 6000 revolutions, the C.O.F increase to 0.9 and finally enters a stable stage.

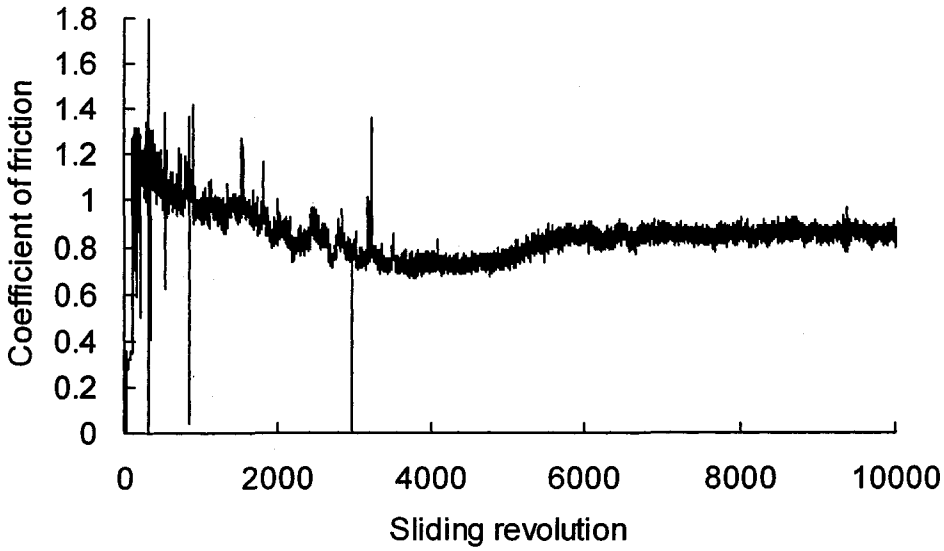

Fig. 6.3 Tribological behaviour of uncoated 319 Al-Si alloy substrate under dry sliding condition.

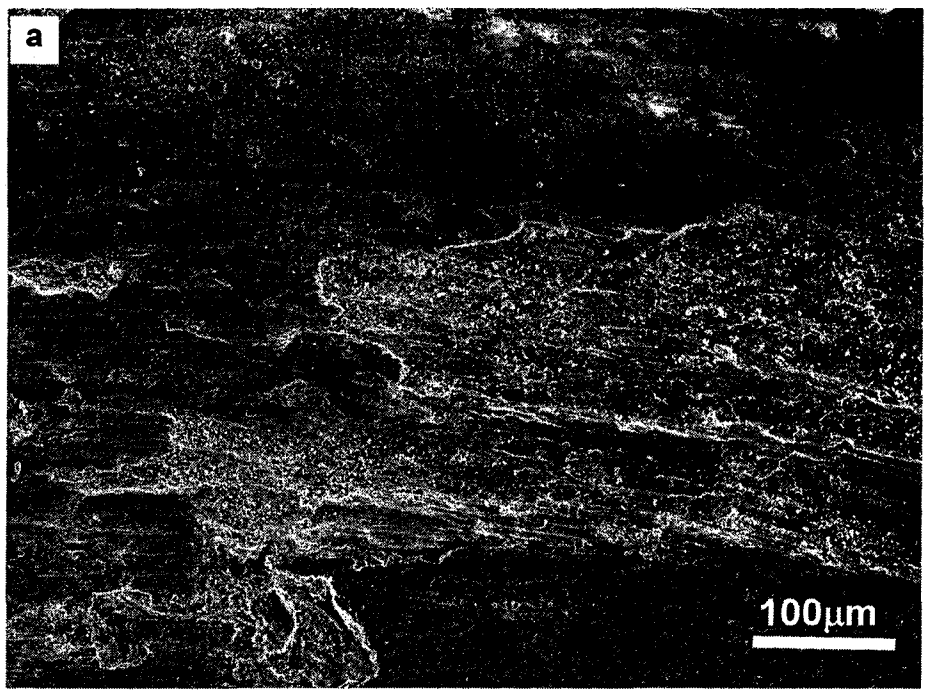

Fig. 6.4(a)

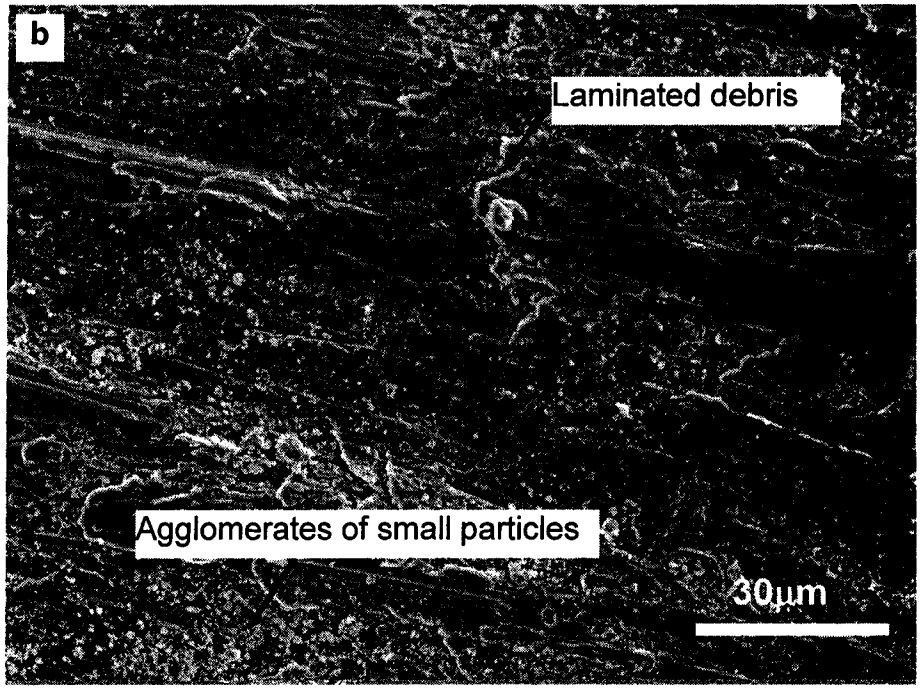

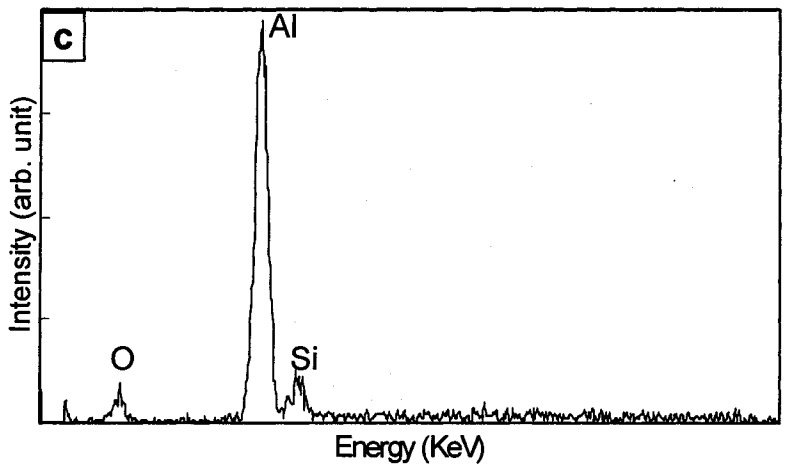

Fig. 6.4 SEM micrographs of wear tracks on the uncoated aluminum alloy under dry sliding condition. (a) Morphology of wear track, (b) the magnified micrograph of wear track showing the debris in the wear track, and (c) EDX spectrum collected from agglomerates of small particles region in the wear track.

The wear track on the uncoated sample is shown in Fig. 6.4. Fig. 6.4(a) is the micrograph of morphology of the wear track where large amounts of deformation and adhesive wear can be observed. In the wear track (the magnified micrograph of wear track Fig. 6.4(b)), there are two types of debris, i.e., agglomerates of small particles and relatively large laminated debris. From the EDX spectrum (Fig. 6.4(c)) collected from wear tracks, the presence of oxygen can only be detected on the agglomerates of small particles. From the C.O.F curve and SEM investigation of wear tracks, it could be deduced that after the break-in stage, the contact surface temperature rise during the sliding test, which results in thermal softening processes and then formation of the oxide film. As a result, the C.O.F reduced. With the increase in surface contact conformity, deformation spreads laterally and downwards into the material, the material transferred from relatively soft substrate is laminated and a compact press layer formed by workharening near the sliding surface. The friction behaviour entered the stable stage, at which the C.O.F is relative high.

Fig. 6.5 presents the variation of the coefficient of friction of thin oxide PEO (curve A12) and oxide-graphite composite coatings (curve AG12). During the sliding (10,000 revolutions), the C.O.F of thin oxide coating (A12) increased from 0.2 to 0.5. The coating was not penetrated during the entire duration of the pin-on-disc tests, i.e., 10,000 revolutions. Curve AG12 in Fig. 6.5 shows an improved tribological behaviour provided by the oxide-graphite composite coating (sample AG12). The composite coating exhibited an average coefficient of friction of 0.2 in the steady state wear region that was almost two times lower than that of the oxide PEO coating (A12) and four times lower than that of the uncoated aluminum alloy. Fig. 6.6(a) shows the wear tracks morphology on samples A12 and Fig. 6.6(b) is the corresponding magnified micrograph. Fig. 6.6(c) is

an EDX spectrum collected from the wear track. The wear track of thin oxide PEO coating (Fig. 6.6(a)) shows a smooth aspects and large amount of iron element can be detected by EDX (Fig. 6.6(c)), which indicated that the wear track are covered by iron mix. From its magnified micrograph (Fig. 6.6(b)), ceramic particles existed in the iron mix and abrasive wear can be observed. It suggests that during the sliding the ceramic particles abraded the steel pin counter surface. The steel material was transferred to the wear track and then was pressed into the wear track in the subsequent sliding.

For the thin oxide-graphite composite coating (Figs. 6.7(a, b)), slightly abrasive wear still can be observed in the wear track. The EXD spectrum (Fig 6.7(c)) shows that the wear track is covered by oxide mix with relatively low amount of carbon and iron element, which indicates that the graphite in the surface layer can improve the wear behaviour.

Fig. 6.8 shows tribological testing results of thicker oxide (sample A22) and oxide-graphite composite coatings (sample AG22). In Fig. 6.8, Curve A22 shows that the coefficient of friction increased from 0.2 to 0.7 in the first 5000 sliding revolutions and stabilized at 0.7. Compared with the C.O.F curve of A12 sample, the curve A22 is much fluctuated and the range of fluctuation is about ± 0.1. However, the curve AG22, showing the variation of the coefficients of friction of the thicker oxide-graphite composite coatings (sample AG22), is relatively smooth and the average coefficient of friction is about 0.16, much lower than oxide PEO coating. The morphology of wear tracks on sample A22 (Figs. 6.9(a, b)) shows that abrasive wear occurs on the wear track and during the sliding, the surface was polished. On the polished wear track surface (Fig. 6.9(b)), the mix of oxide and iron is laminated. Fig. 6.10 is the micrographs of wear track

on AG22. Only a small wear scar can be observed on the composite coating surface. The coating surface is polished and no abrasive wear is observed.

The worn surfaces of counterfaces are shown in Fig. 6.11. Except that the pin against the uncoated aluminum alloy is covered by adhesion material transferred from relative soft aluminium alloy, all the counterface pins are wore off. Fig. 6.12 is the summary of wear rate of counterface material. From Figs. 6.11 and 6.12, it can be seen that the composite coatings (AG12 and AG22) only cause a low wear loss to the pin counterfaces. Sample AG22 has slightly better counterface compatibility than AG12, which may result from the more graphite coverage on the latter surface than the former.

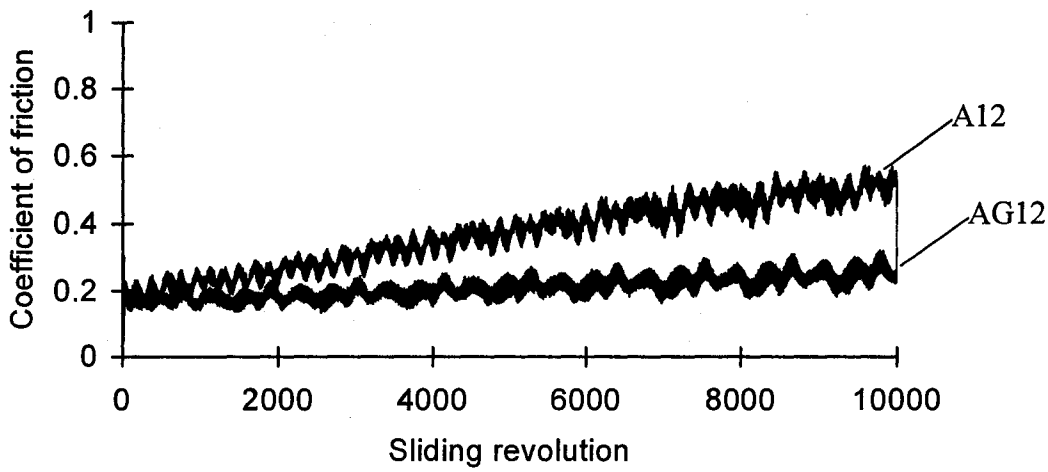

Fig. 6.5 Tribological behaviour of thin PEO oxide (A12) and oxide-graphite composite coatings (AG12) under dry sliding conditions.

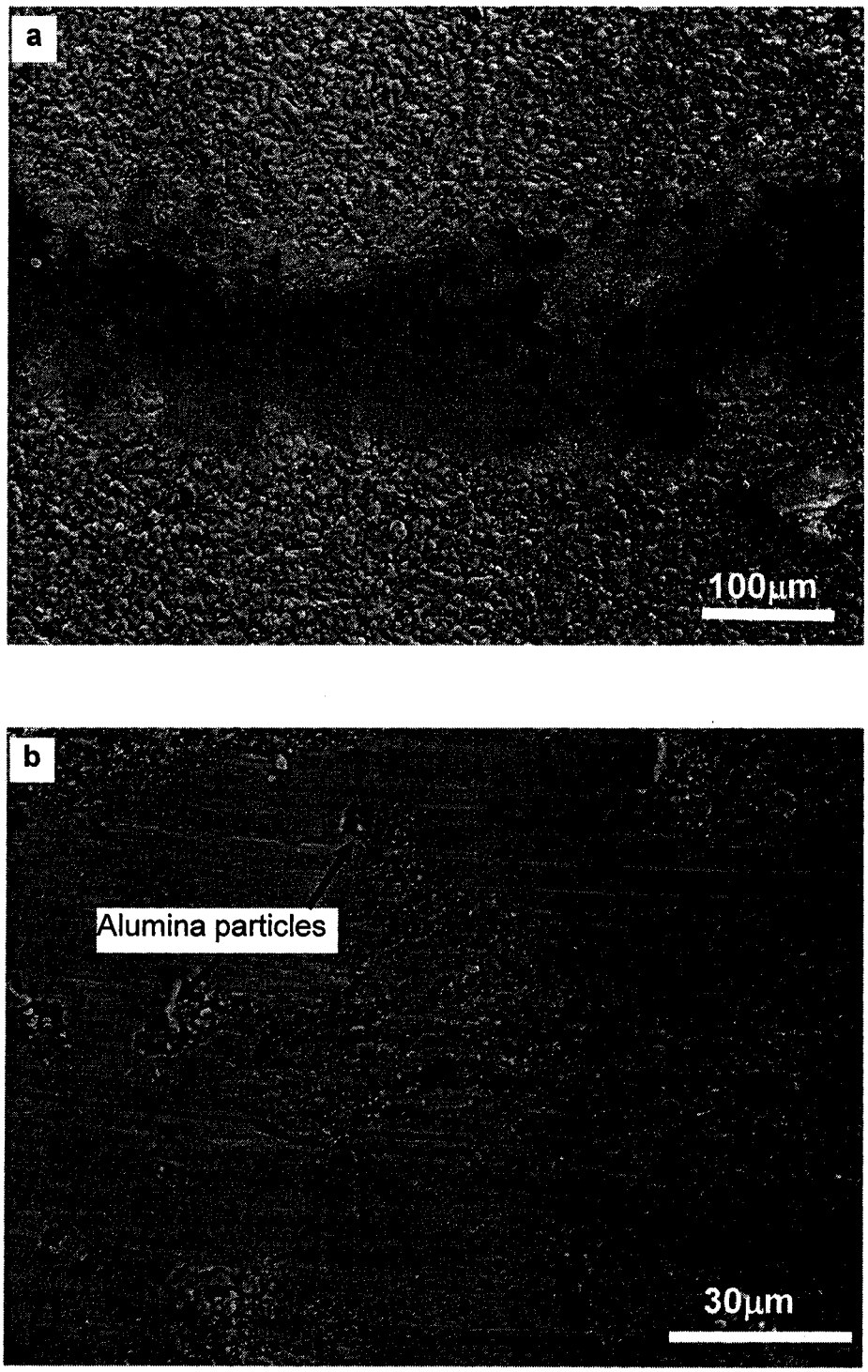

Fig. 6.6(a, b)

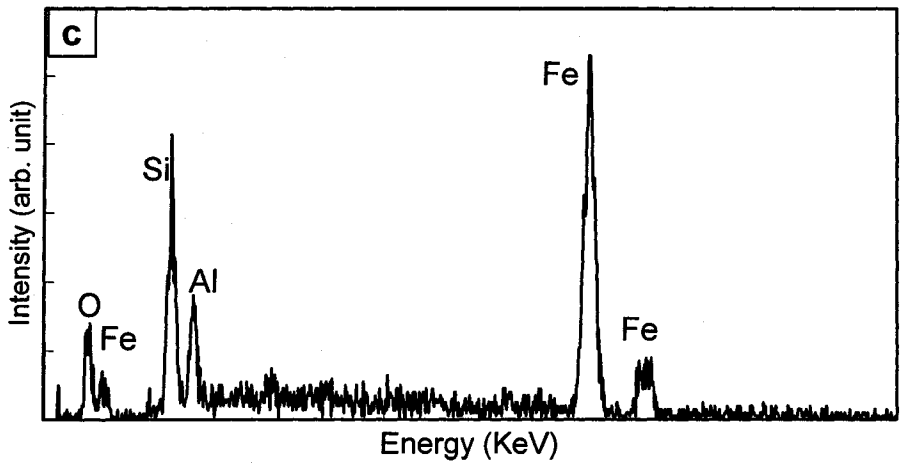

Fig. 6.6 SEM micrographs and EDX spectrum of wear tracks on samples A12. (a) the wear track morphology, (b) magnified micrograph of (a), (c) EDX spectrum of the wear track.

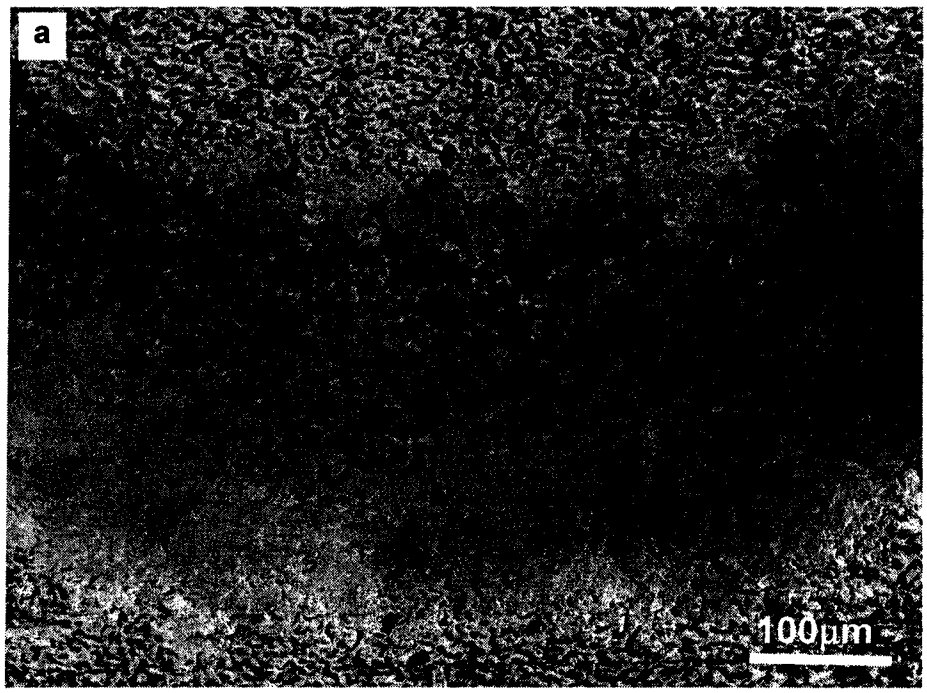

Fig. 6.7(a)

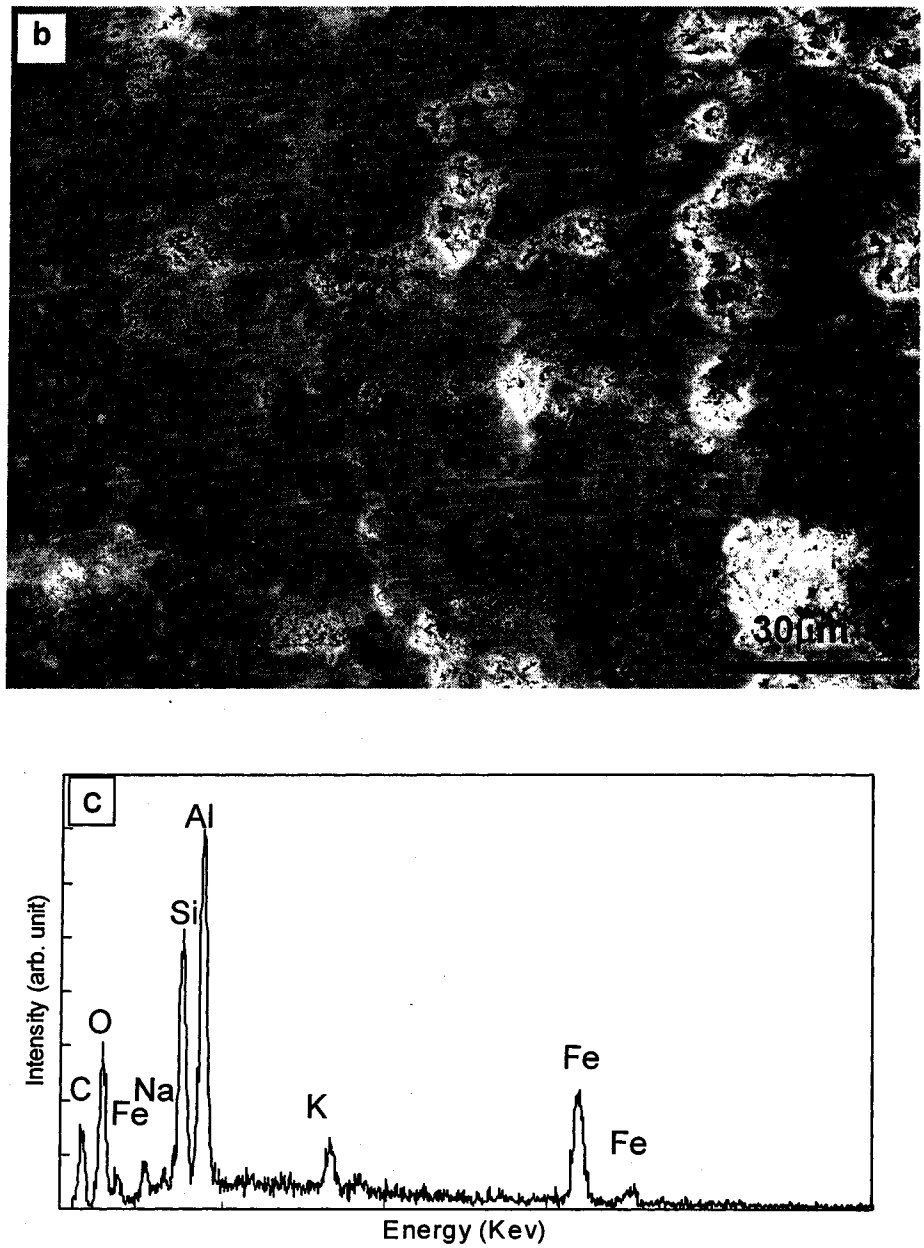

Fig. 6.7 SEM micrographs and EDX spectrum of wear tracks on sample AG12. (a) morphology of wear track, (b) magnified micrographs of (a), (c) EDX spectrum of the wear track.

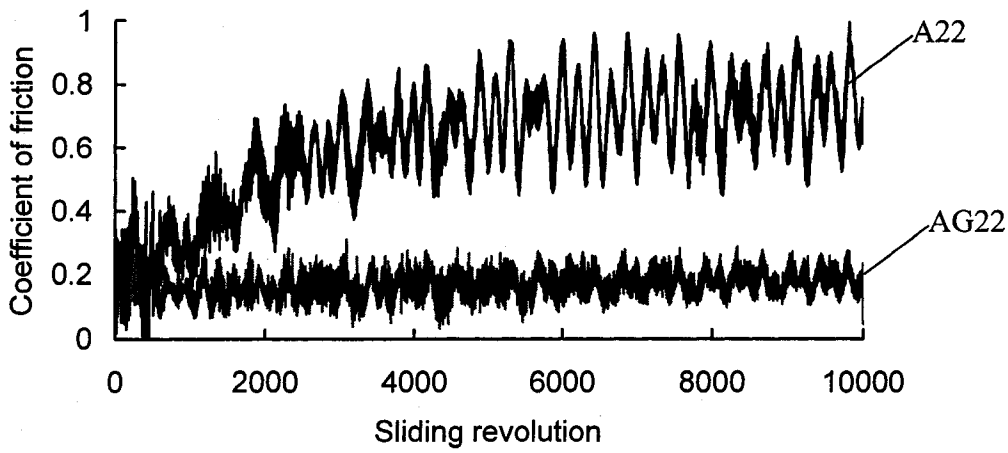

Fig. 6.8 Tribological behaviour of the thick oxide PEO (A22) and oxide-graphite composite coatings (AG22) under dry sliding conditions.

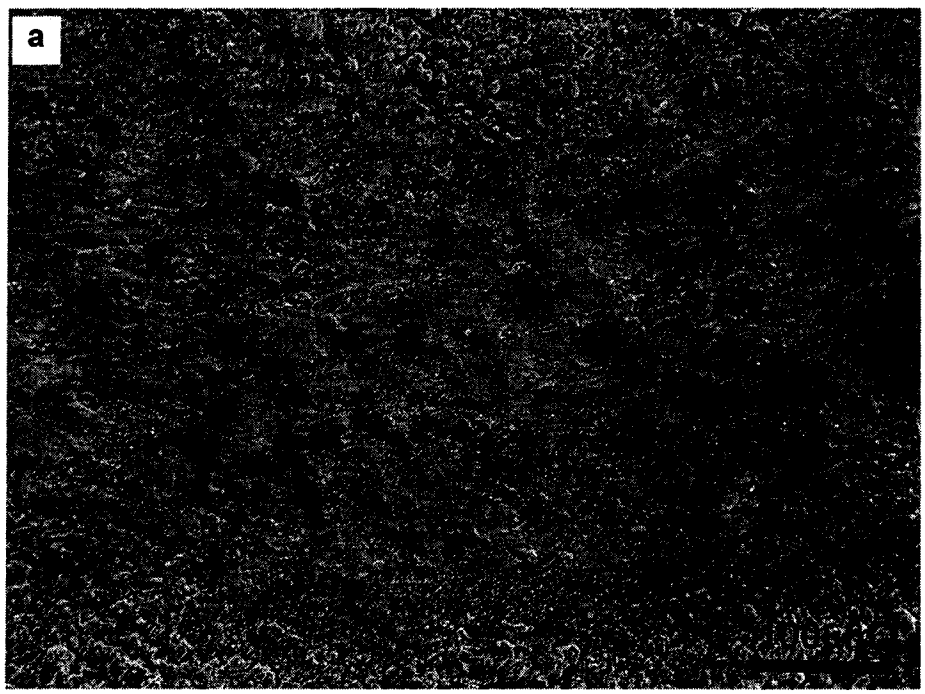

Fig. 6.9(a)

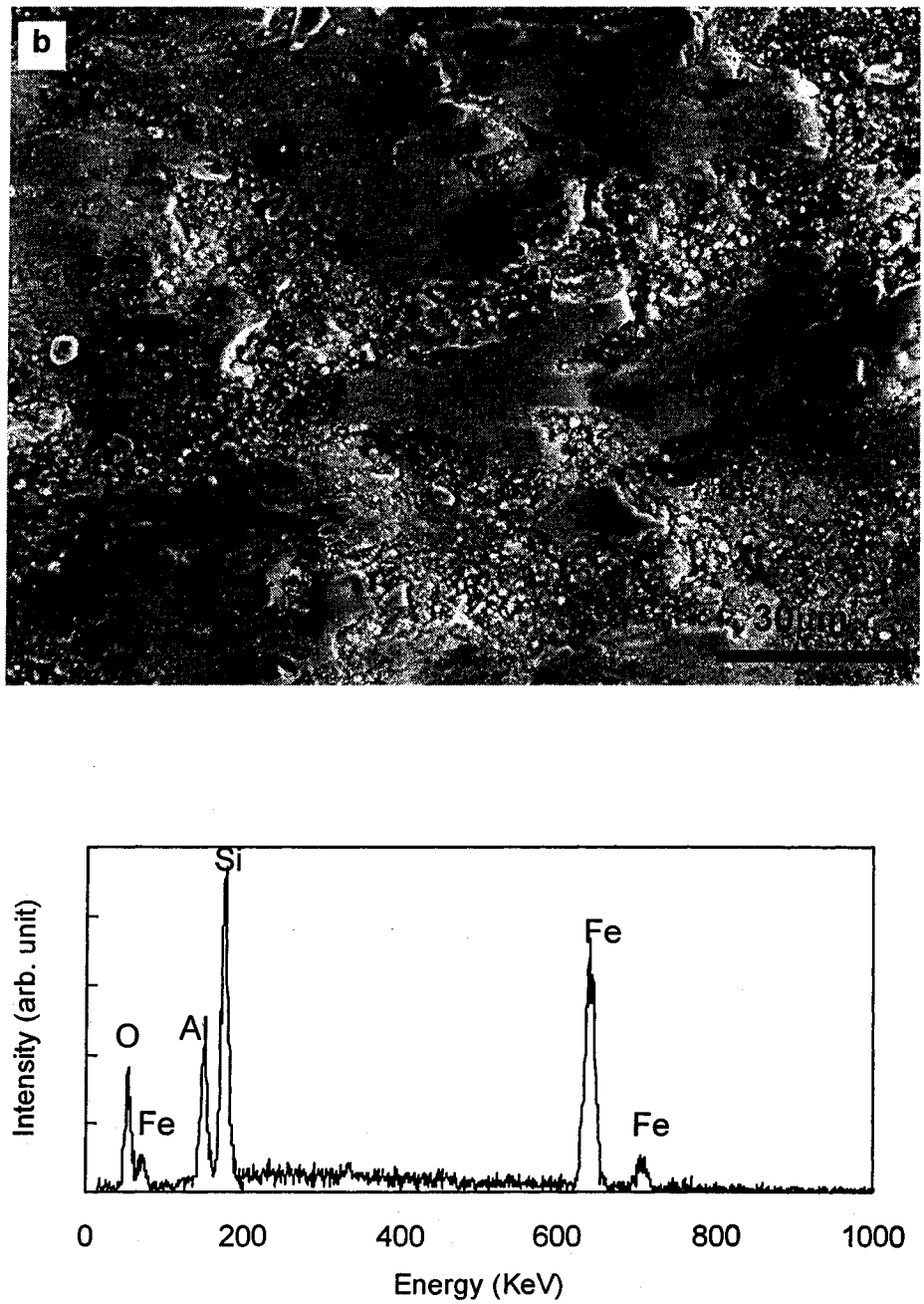

Fig. 6.9 SEM micrographs and EDX spectrum of wear track on sample A22. (a) morphology of wear track, (b) magnified micrographs of (a), (c) EDX spectrum of the wear track.

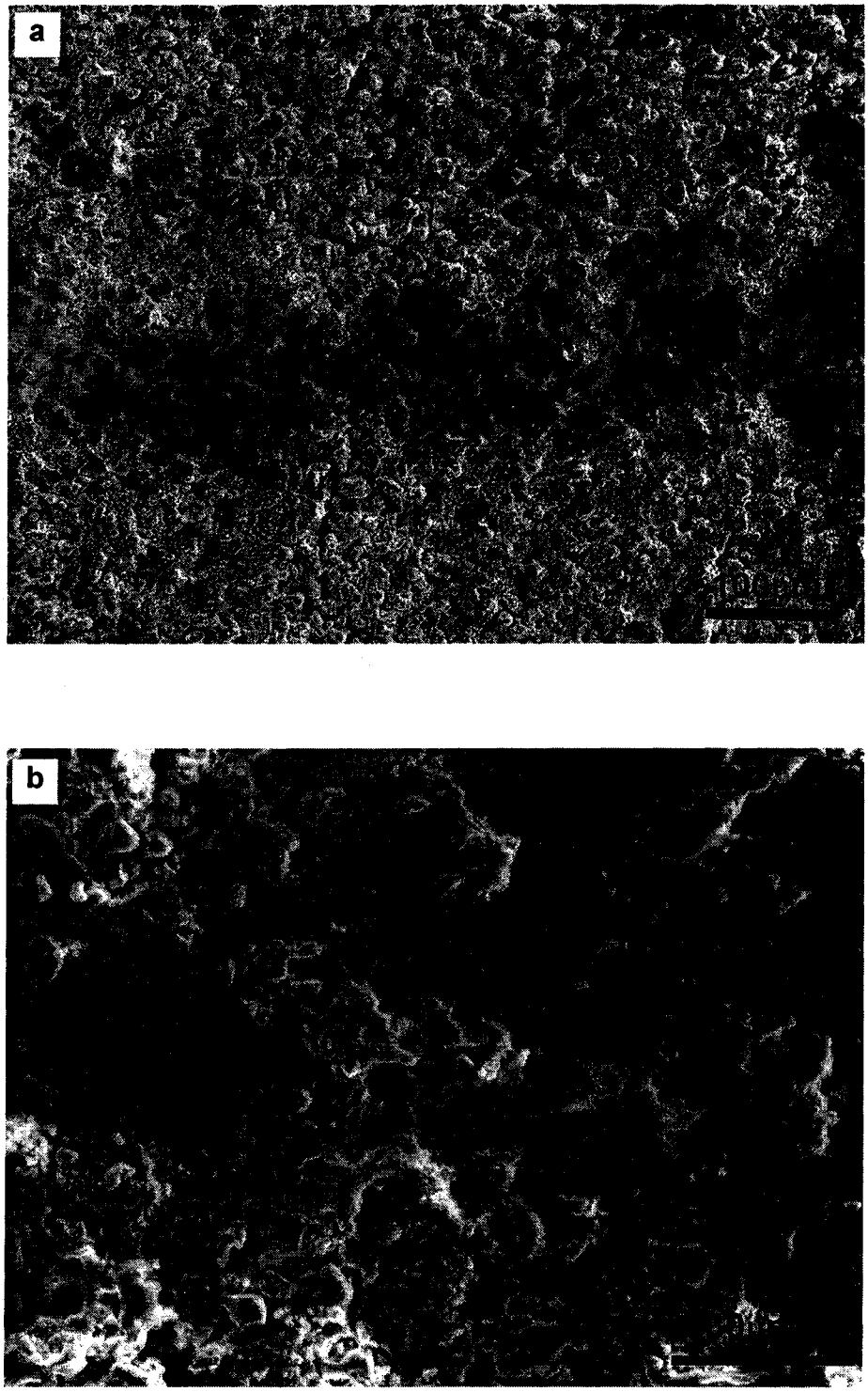

Fig. 6.10(a, b)

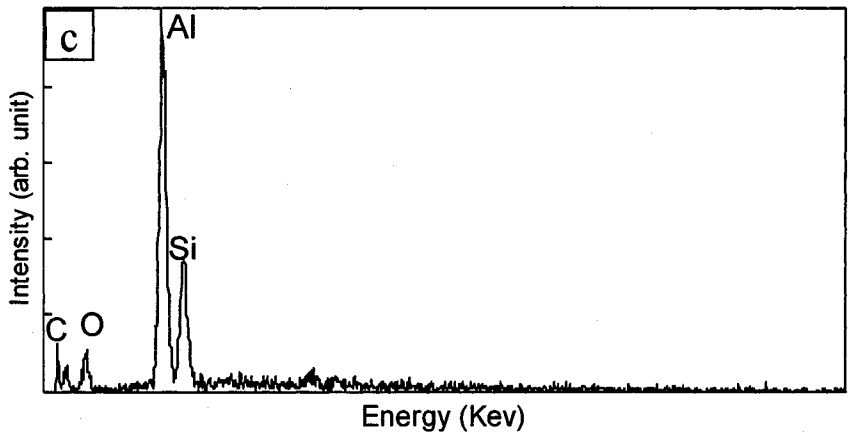

Fig. 6.10 SEM micrographs of wear tracks and EDX spectrum on sample AG22. (a) morphology of wear track (b) magnified micrographs of (a), (c) EDX spectrum of the wear track.

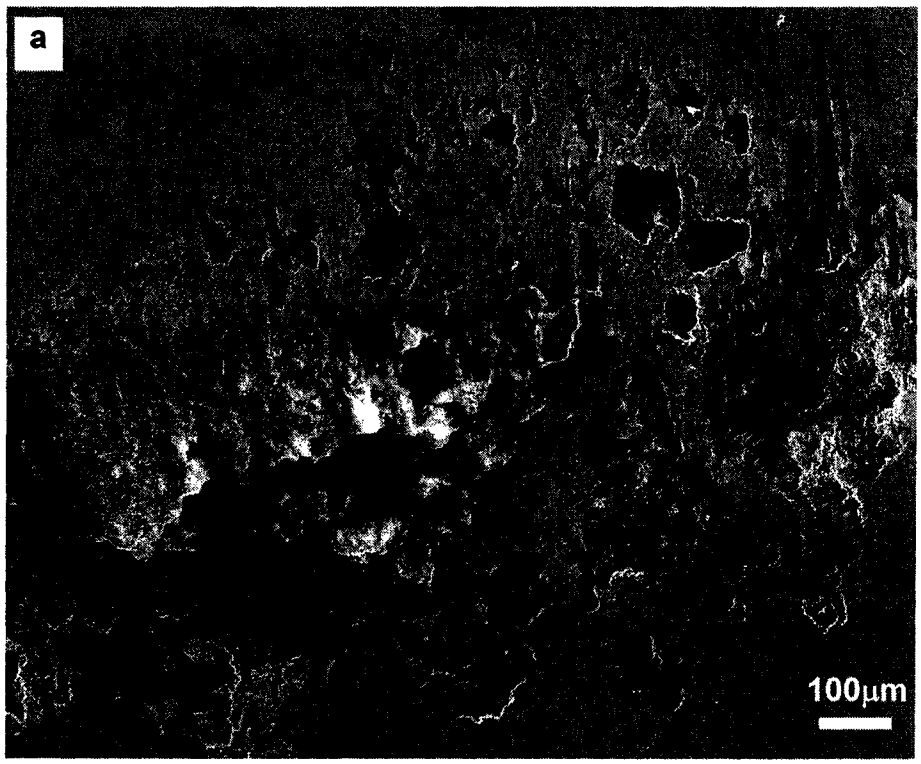

Fig. 6.11(a)

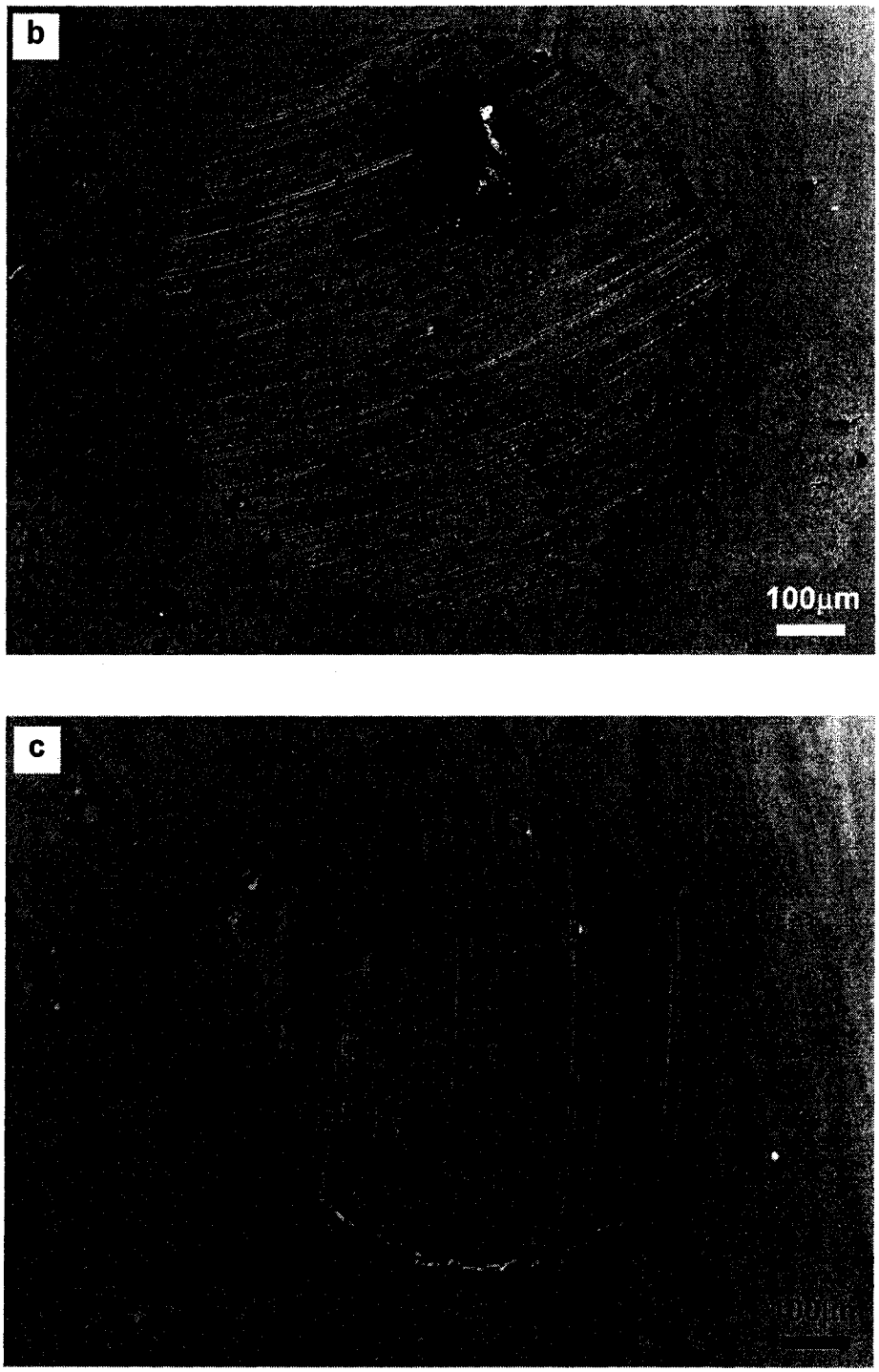

Fig. 6.11(b, c)

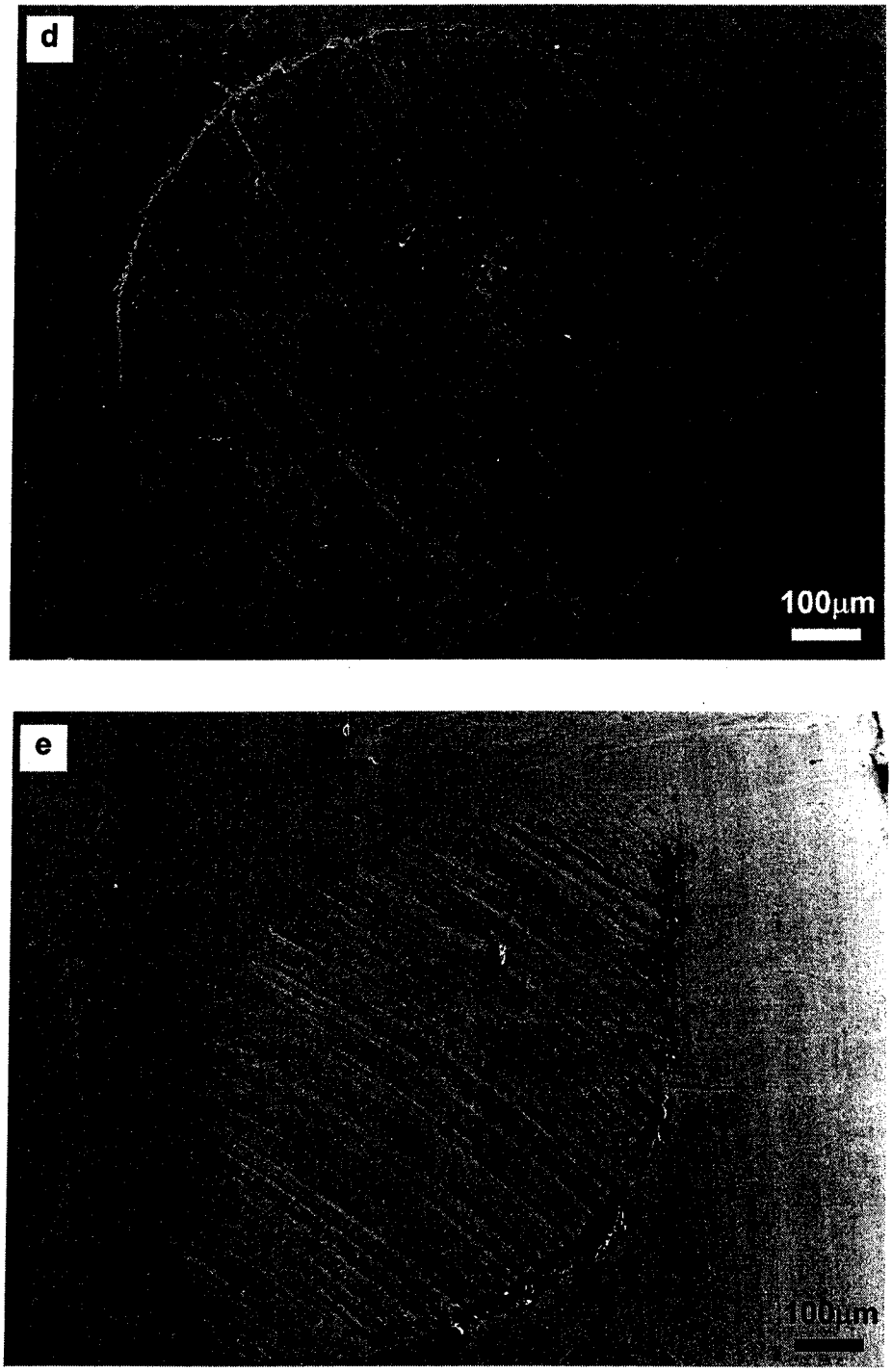

Fig. 6.11 SEM micrographs of the worn counterface pins against samples (a) uncoated Al alloy, (b) A12, (c) AG12, (d) A22 and (e) AG22.

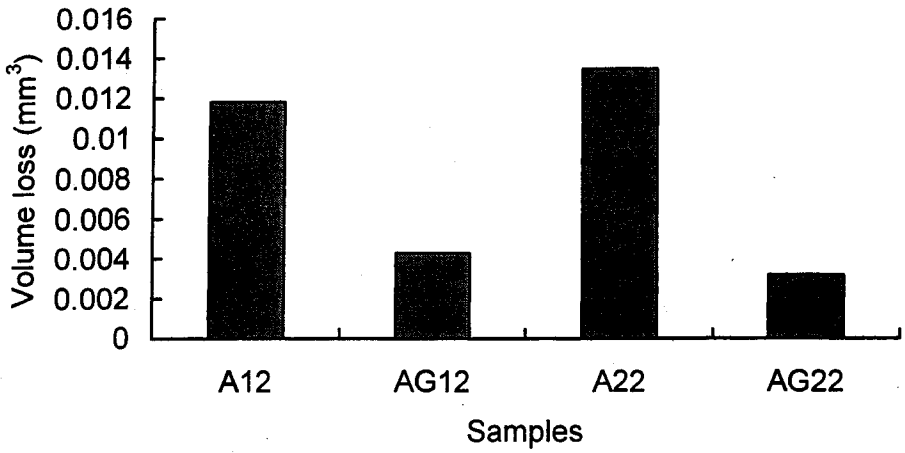

Fig. 6.12 Wear loss of counterface pins after sling wear tests under dry condition.

6.1.3.2 Tribological tests with lubricant

Fig. 6.13 shows the coefficient of friction of samples during sliding wear test under lube condition. Fig. 6.13(a) shows the tribological behaviour of the uncoated Al alloy under lube sliding condition. During the whole wear test, the friction coefficient is stable and the value is about 0.1. In Fig. 6.13(b), the plotted curves A12 and AG12 are overlapped, which indicates that under lube sliding the two coated samples A12 and AG12 have similar wear behaviour. The friction coefficients of both coatings are about 0.14. Fig. 6.13(c) shows the C.O.F variation of samples A22 (curve A22) and AG22 (curve AG22). Like Fig. 6.13(b), the two coatings have similar wear behaviour during the wear test, and average value of C.O.F is about 0.16. The wear track on uncoated Al alloy after sliding test with lube and its magnified micrograph are respectively shown in Fig. 6.14(a) and Fig. 6.14(b). Slightly abrasive wear can be observed in the wear track, where the soft Al matrix material is abraded. At the given lube testing condition, the wear tracks

on the coated samples are too shallow and blurred to have a good image. Thus, no SEM micrograph is shown for the coatings.

Fig. 6.15 shows the worn counterface pins against different samples: (a) uncoated Al alloy, (b) sample A12, (c) sample AG12, (d) sample A22, and (e) sample AG22. By investigating the worn area on pins, the wear rate of pins can be calculated. The calculated results are plotted in Fig. 6.16, showing that the volume loss of counterface pins against the oxide-graphite composite coatings is much lower than that against the oxide coatings. The sample AG22, which has higher graphite content in the composite coating than the sample AG12, causes the lowest wear loss to a steel counter pin. Thus, the sample AG22 has the best compatibility with steel counterface.

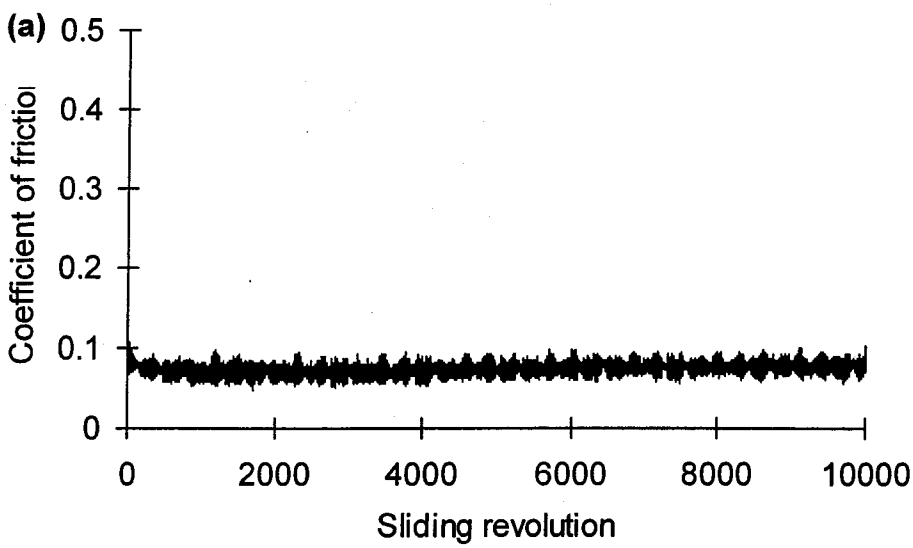

Fig. 6.13(a)

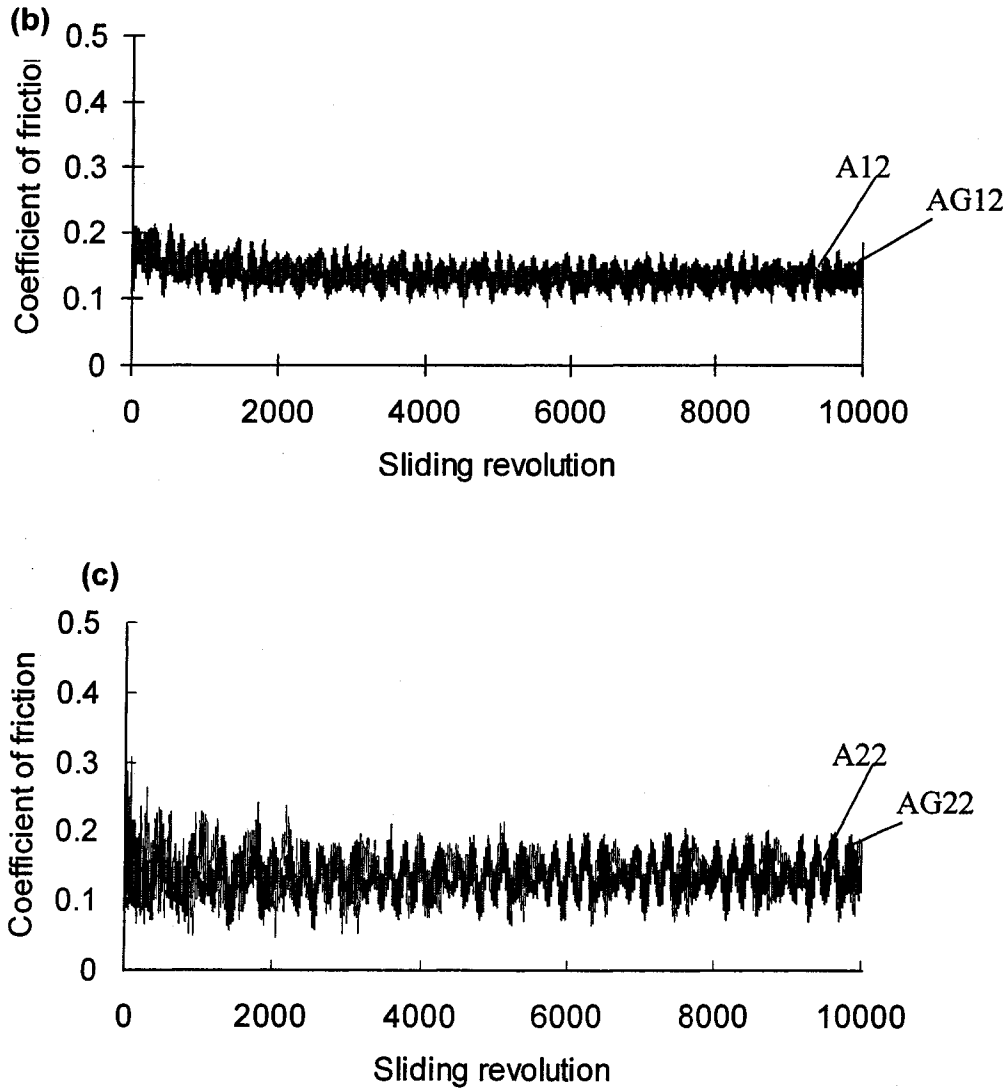

Fig. 6.13 Tribological behaviour of (a) uncoated substrate, (b) samples A12 and AG12, and (c) samples A22 and AG22 under lube sliding condition.

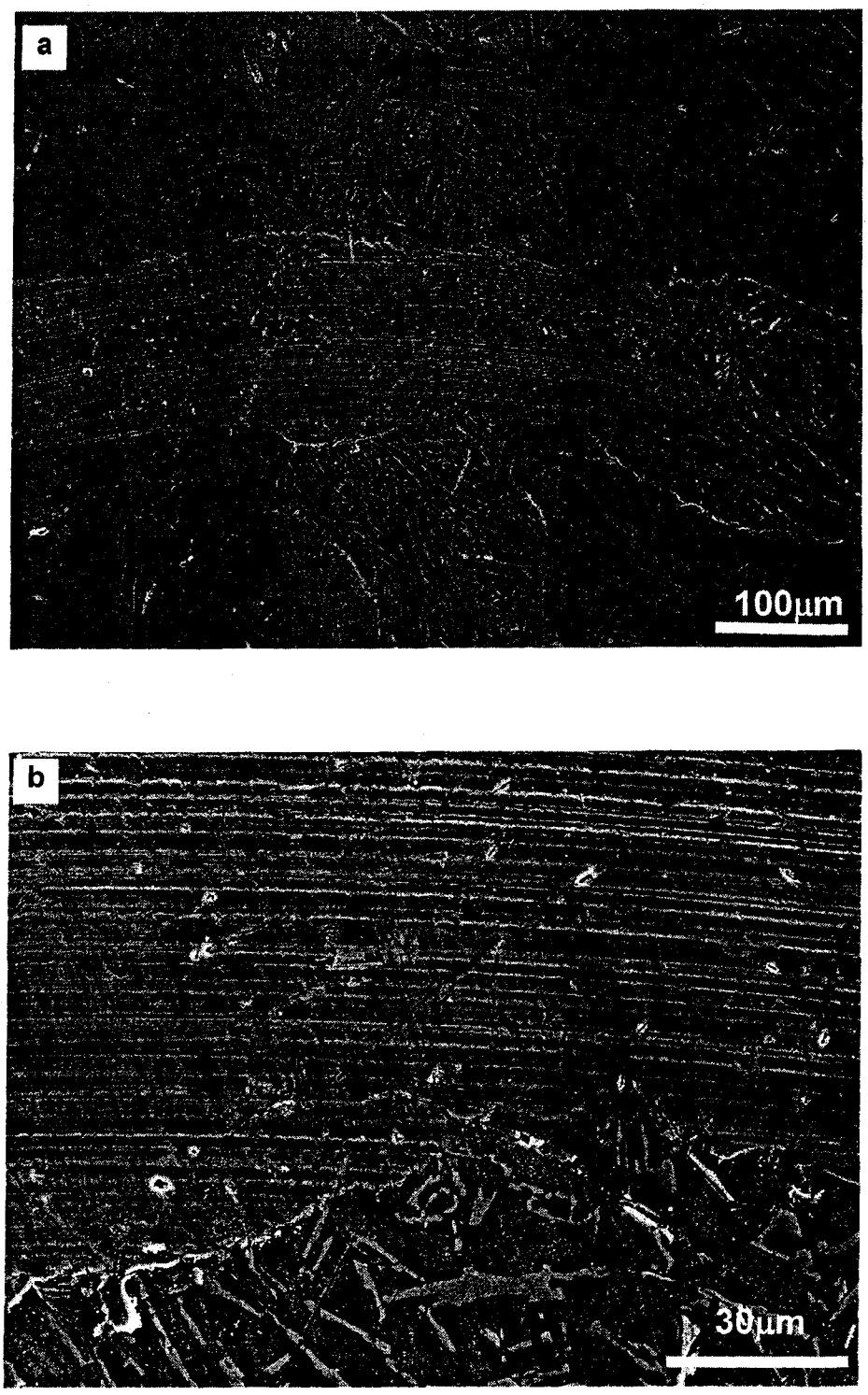

Fig. 6.14 SEM micrographs of the wear track on uncoated Al alloy at lube sliding test. (a) wear track morphology, and (b) magnified micrograph of the wear track.

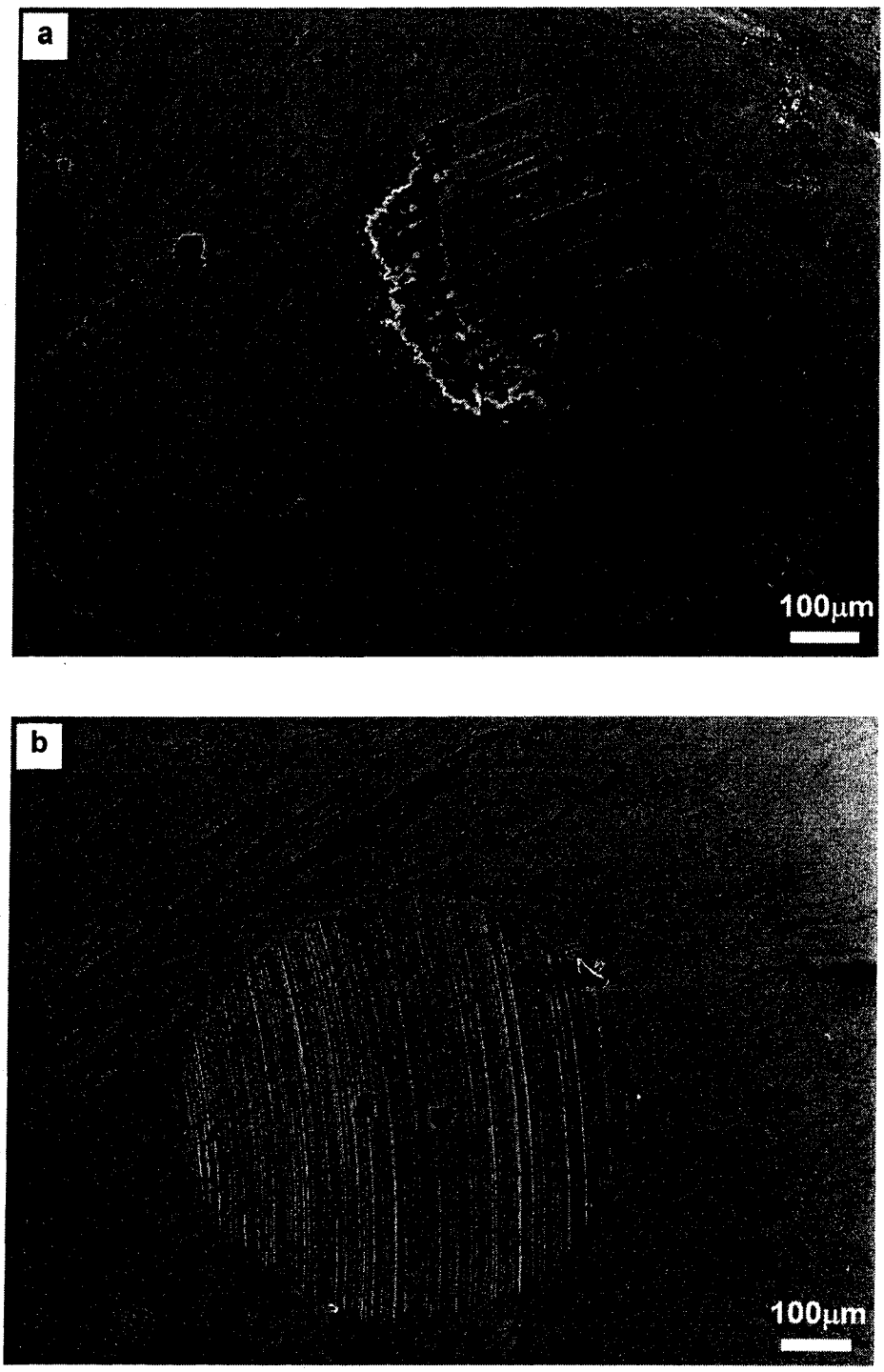

Fig. 6.15(a, b)

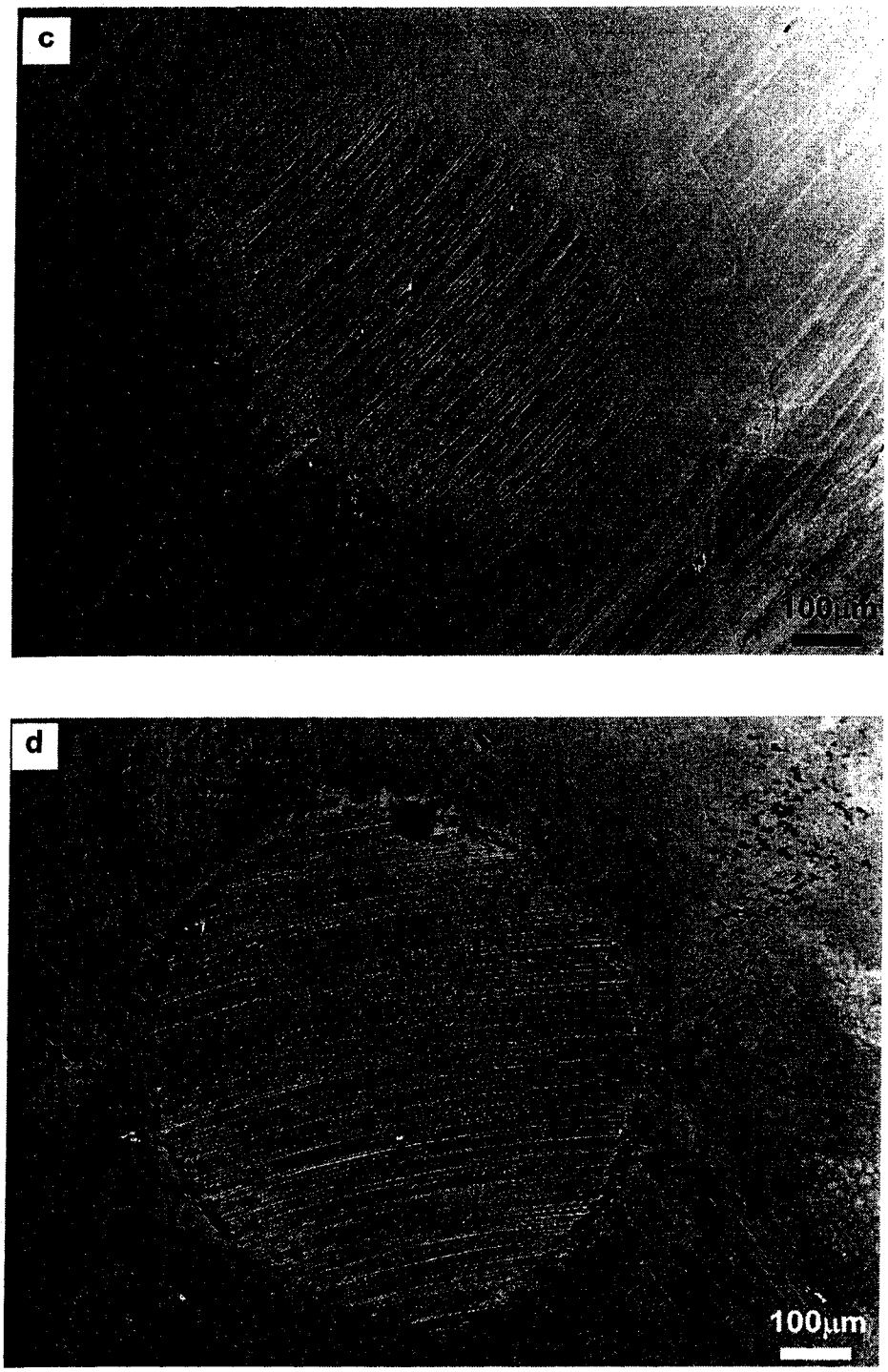

Fig. 6.15(c, d)

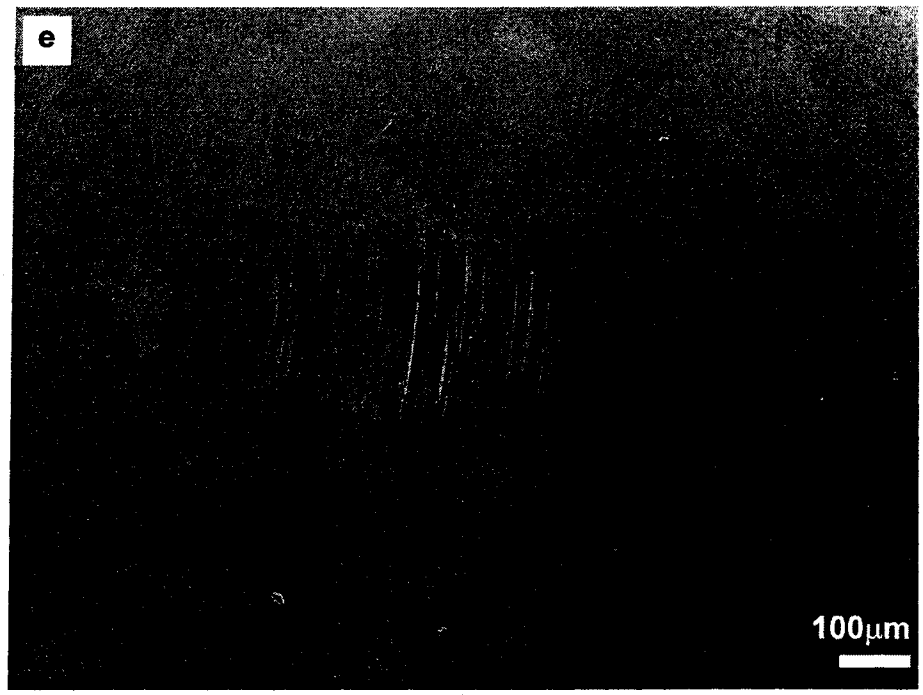

Fig. 6.15 SEM micrographs of worn counterface pins after sliding wear test with lube against (a) uncoated Al alloy sample, (b) sample A12, (c) sample AG12, (d) sample A22, and (e) AG22.

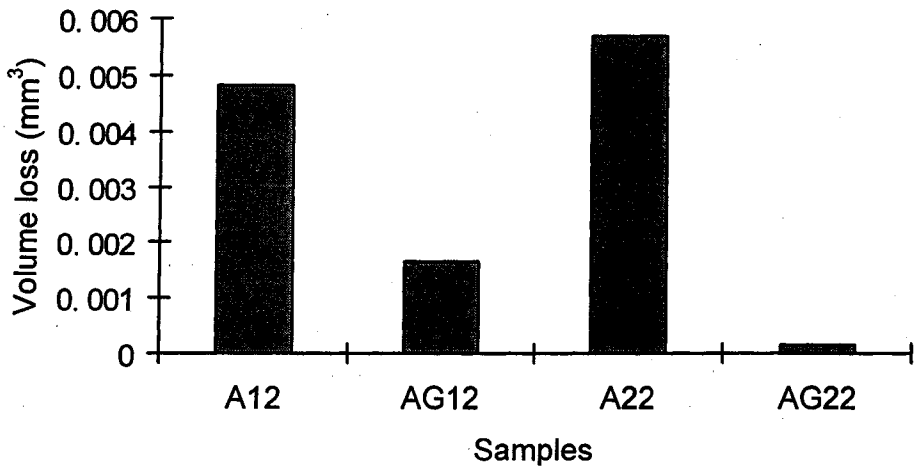

Fig. 6.16 Wear volume loss of counterface pins after sliding wear test with lube.

6.2 Discussion

Fig. 6.17 schematically illustrates the structure of an oxide-graphite composite coating. At the final stage of the PEO treatment, coating fusing, mixing and quenching occur. Pores in the outer layer provide graphite particles with anchors. The graphite after rubbing is embedded into the porous top layer. During the subsequent treatment, though some graphite may be oxidized or ejected away from coating surface by discharges, part of the graphite still can be integrated into the oxide coatings. As a result, an oxide-graphite composite coating forms, which has been observed in SEM investigation (Fig. 6.1). In the composite coating, graphite particles are scattered in distribution which is similar to that of graphite in the metal matrix-graphite composites [70]. Since the rough surface can enhance the graphite coverage ratio on the surface, the thicker composite coating (sample AG22) has higher graphite coverage due to its relatively rougher surface and larger oxide projections and valleys. The tribological testing results of Al alloy substrate (Fig. 6.3-6.4) indicate that the wear mechanism of Al-Si alloy under the dry sliding test in this part of experiment is mainly adhesive wear and under lube sliding test (Fig. 6.13(a) and Fig. 6.14), it turns out to be a slight abrasive wear. The sliding test results show that all the PEO coatings can protect substrate from severe adhesive and abrasive wear. While, under dry sliding test, the oxide PEO coatings have much high C.O.F, i.e., the value is about 0.8. The wear mechanism of oxide coatings is mainly two body abrasion (ceramic particles and steel) or three body abrasive wear due to fine oxide particle transferred to contact interface. The abrasive wear severely hurt the counterface material, thus large material loss occurs on the worn steel pins. Because the oxide projection size on the thick A22 coating is larger than that of A12, as described in chapter

5, the C.O.F curve of A22 (Fig. 6.8) fluctuated a lot during the sliding. The C.O.F curve of the coating A12 is smoother (Fig. 6.5).

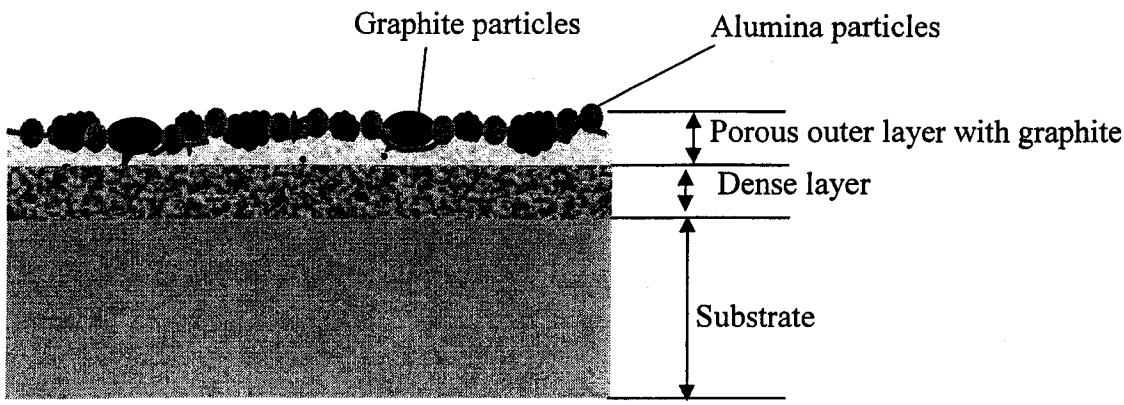

Fig. 6.17 Schematic of the structure of oxide-graphite composite coating

The oxide-graphite composite coatings exhibit a significantly reduced friction coefficient (Figs. 6.5 and 6.8) and wear loss of counterface pins (Fig. 6.11), compared with those of uncoated substrate and oxide PEO coatings. The C.O.F is about 0.2 under dry sliding condition. This is an indication of effective intervention of a thin film of graphite existed between the coating and counterface. During the sliding, the film of graphite forms gradually and continuously as a result of graphite supplied from the composite coating surface and subsurface. Fig. 6.18 illustrates the formation of graphite film during the sliding process. The graphite is held by oxide projections. During the sliding, the composite layer not only can supply graphite continuously but also can bear a high load. Moreover, due to continuous graphite film formed at the interface, the coating has good compatibility with counterface. Unlike the hard composite ceramic coating synthesized in this study, conventional polymer-base solid film lubricant (SFL) coatings [71] on treated or untreated aluminum surfaces can not withstand a large contact load.

The SFL topcoat is subject to remove by plowing under normal load, which is illustrated in Fig. 6.19. The topcoat will lose its lubricated function after a short sliding distance under high load applications.

Under the lubricant, all the coatings have similar wear behaviour. Their values of C.O.F are about 0.15. The wear loss of counterface pins is much lower under lube tests than under dry tests. For the lube tests, the composite coatings AG12 and AG22 cause lower wear loss on pins than the oxide coatings A12 and A22. The coating AG22 gives the lowest wear loss to steel pin.

6.3 Summary

In this chapter, we attempt to develop an oxide-graphite composite coating with excellent tribological properties including low friction, high wear resistance but also excellent compatibility with counterface materials. The composite coatings have a structure similar to the PEO coating except for an oxide-graphite outer top layer, in which graphite is embedded in the pores between the oxide projections. The oxide PEO coating improved the wear resistance of the Al-Si alloy substrate; however, it caused a severe abrasive wear on the steel counterface. The composite layer in the oxide-graphite coating can supply graphite gradually and continuously, which results in formation of a lubricant layer at the interface during the sliding. Thus, incorporation of lubricant graphite into the top oxide layer, forming an oxide-graphite composite coating provided not only high wear resistance and low friction to the coated Al-Si alloy but also good compatibility to the steel counterface.

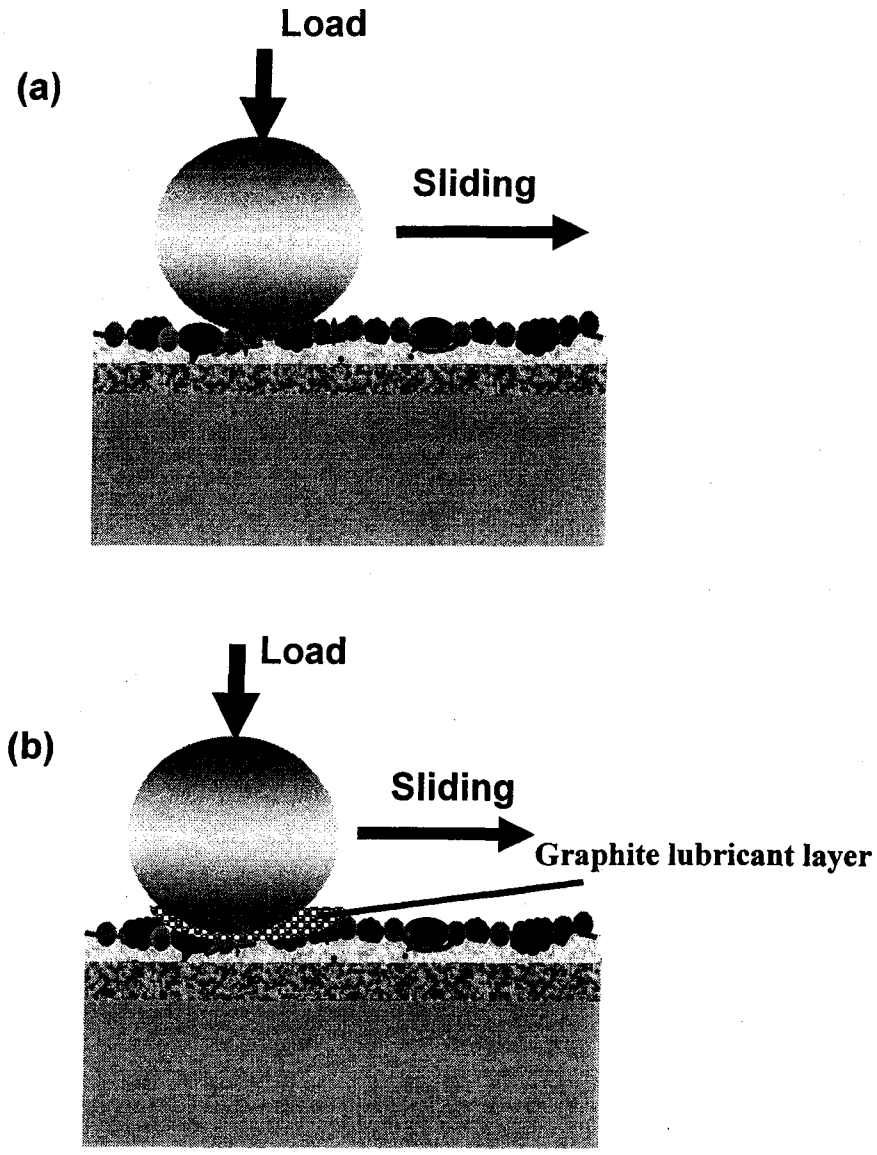

Fig. 6.18 Schematic of wear behaviour of oxide-graphite composite coatings.

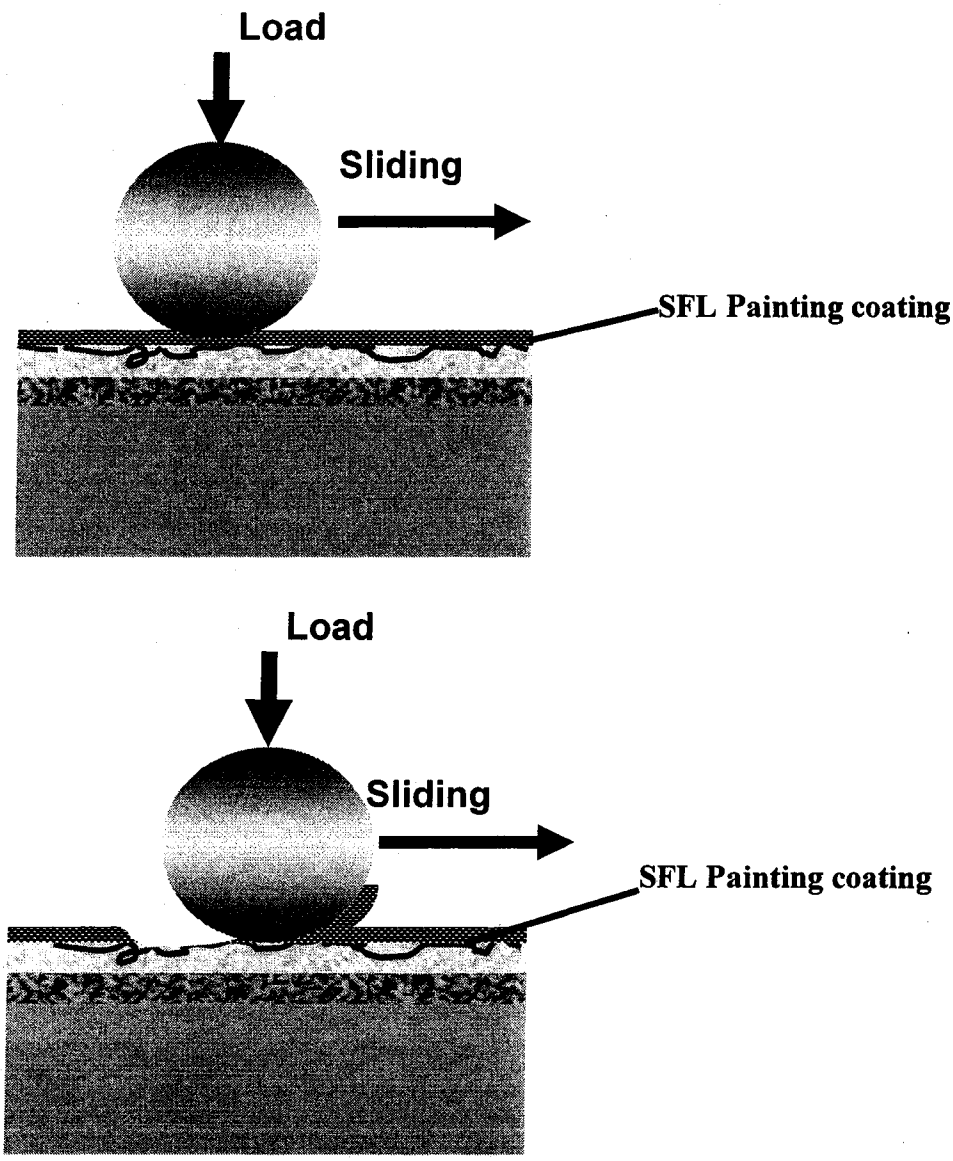

Fig. 6.19 Schematic of polymer-base solid film lubricant (SFL) on hard coatings. The painted SFL coating may readily be removed under a high contact load.

CHAPTER 7 CONCLUSIONS

In this thesis, investigations into the effect of Si content and process (electrolytic and electrical) parameters on the PEO coating formation and properties were conducted. A PEO oxide-graphite composite coating with high wear resistance, low friction, and friendly compatibility to pin steel counterface was particularly developed for the tribological application. The thesis includes three parts of study, and the research results are summarized as follows.

The effect of silicon content on the PEO coatings

Effect of silicon content on the coating process, morphology, and composition were investigated in the first part of study. Using low current density and low electrolyte concentration, thin PEO coatings (about 10 μm in thickness) were produced on 319 and 390 Al-Si alloys. The coating process was found to have four distinguished stages. In the first three stages, the duration time and morphology of each stage were considerably affected by the silicon content in Al-Si alloys. The micro-arc discharge started to appear at Al-Si interfaces on the alloy surface when the electrical potential reached up to the critical voltage of ~390V for the 319 alloy and ~400 V for the 390 alloy. At the silicon-rich region in the alloys, an Al-Si-O compound with a relatively low melting point formed and it exhibited a porous microstructure comparing with the aluminium rich matrix. The higher silicon content in 390 alloy resulted in a rougher coating surface on the PEO-treated 390 alloy than on the PEO-treated 319 alloy. After the applied voltage was higher than 480V and the process entered stage IV, the composition of the oxide coating for the 319 and 390 alloys were similar. The main phases were γ-Al_2O_3 and a

small amount of Al_2O_3-SiO_2 compound for both coated alloys. Although the thin coating on the 390 alloy exhibited a higher surface roughness than the thin coating on the 319 alloy, the coating surface morphology and roughness are expected to be similar for both alloys when the voltage increases to a higher level (e.g., 600V). The effect of silicon content in a thicker coating (e.g., >50 μm) might not be significant.

The effect of electrolytic and electrical parameters on the PEO coatings

The second part of study has investigated the effect of electrolytic and electrical parameters, where various electrolytic and electrical parameters were selected to prepare the PEO coatings on the 319 alloy. The thickness of coatings deposited in 4g/l Na_2SiO_3 with the maximum 500V voltage is about 10μm and the coatings is composed of an outer layer, non-continuous dense layer and inner dense layer. The phase composition of the thin PEO coating is mainly γ-Al_2O_3. The PEO coating prepared in an 8g/l Na_2SiO_3 electrolyte has a larger thickness (20-25μm) and the coating appears to have a continuous dense layer in the between of outer porous layer and inner dense layer. It was also found that the coating deposited in the high concentration electrolyte has more amounts of Al_2O_3-SiO_2 compound phases, and also α-Al_2O_3 phase. Although the coating phase compositions are different, the hardness of the coatings deposited by different parameters is all in the range of 800-1000 HV. The current density effect on coating structure, and coating hardness was not found to be significant. However, with the increase in current density, the surface morphology change increased due to the oxide projection size increase, which could result from intensive discharge occurrence under the higher current density.

Oxide-graphite composite coating

In the final part of study, an oxide-graphite composite coating with an improved tribological property was developed. The composite coating has a structure similar to a PEO coating except for an oxide-graphite outer top layer, in which graphite is embedded into the pores between the oxide projections. The oxide PEO coating improved the wear resistance of the Al-Si alloy substrate; however, it caused a severe abrasive wear on the steel counterface. The composite layer in the oxide-graphite coating can supply graphite continuously to form a solid lubricant layer at the contact interface during the sliding. Thus, incorporation of solid lubricant graphite into the top oxide layer, forming the oxide-graphite composite coatings, provided not only high wear resistance and low friction to the coated Al-Si alloy but also good compatibility to the steel counterface.

REFERENCES

[1] A.M. Sherman, in E.A. Starke, Jr., T.H. Sanders, Jr., W.A. Cassada (ed.), Aluminium alloys: their physical and mechanical properties, Vol. 331-337, Part 1, Trans tech publications Ltd., 2000, p3-4.

[2] J.T. Staley, R.L. Rolf, in C. Bickert, M. Bouchard, G. Davies, E. Ghali, Eva Jiran (ed.), Light metals processing and application, Canadian institute of mining, Montreal, 1993, p629-642.

[3] R Shivanath, P.K. Sengupta, Eyre T S, The British Foundryman, 70 (1977), 349-356.

[4] A.S. Reddy, B.N.P Bai, K.S.S. Murthy, S.K. Biswas, Wear, 171 (1994), 115-127.

[5] B.S. Shabel, D.A. Granger, W.G. Truckner, in D. Olson Hardbound (ed.), ASM Handbook, Vol. 18, 1992, p785-794.

[6] M.J. Koczak, S.C. Khatri, J.E. Allison, M.G. Bader, in S. Suresh, A. Mortensen, A. Needleman (ed.), Fundamentals of Metal-Matrix Composites, Elsevier, 1993, p301-308.

[7] V.J. Michaud, A.K. Ghosh, in S. Suresh, A. Mortensen; A. Needleman (ed.), Fundamentals of Metal-Matrix Composites, Elsevier, 1993, p3-40.

[8] S.Q. Wu, H.Z. Wang, S.C. Tjong, Composites Science and Technology, 56 (1996), 1261-1270.

[9] S. Wilson, A.T. Alpas, Wear, 196 (1996), 270-278.

[10] J. W Cox, in R.F. Bunshah (ed.), Handbook of Hard Coatings, William Andrew Publishing, 2001, p420-457.

[11] Y.C. Wang, S.C. Tung, Wear, 225-229 (1999), 1100-1108.

[12] A.E. Ostermann, Experiences with Nickel-Silicon Carbide Coatings in Cylinder Bores of Small Aluminum Engines, TP 790843, Society of Automotive Engineers, 1979.

[13] A. Edrisy , T. Perry, Y.T. Cheng, A.T. Alpas, Wear, 251 (2001), 1023-1033.

[14] Ronald A. Walsh, Electromechanical Design Handbook (3rd Edition), McGRAW-HILL, New York (2000), p13.15.

[15] E.I. Meletis, X. Nie, F.L. Wang, J.C. Jiang, Surface & Coatings Technology, 150 (2002), 246-256.

[16] X. Nie, C. Tsotsos, A. Wilson, A.L. Yerokhin, A. Leyland, A. Matthews, Surface & Coatings Technology, 139 (2001), 135-142.

[17] A.A. Voevodin, A.L. Yerokhin, V.V Lyubimov, M.S. Donley, J.S. Zabinski, Surface & Coatings Technology, 86-87 (1996), 516-521.

[18] X. Nie, E.I. Meletis, J.C. Jiang, A. Leyland, A.L. Yerokhin, A. Mathews, Surface & Coatings Technology, 149 (2002), 245-251.

[19] L.Rama Krishna, K.R.C. Somaraju, G. Sundararajan, Surface & Coatings Technology, 163-164 (2003), 484-490.

[20] G. Sundararajan, L. Rama Krishna, Surface & Coatings Technology, 167 (2003), 269-277.

[21] X. Nie, A. Wilson, A. Leyland, A. Matthews, Surface & Coatings Technology, 131 (2000), 506-513.

[22] X. Nie, A. Leyland, A. Matthews, Surface & Coatings Technology, 125 (2000), 407-414.

[23] A.L. Yerokhin, V.V. Lyubimov, R.V. Ashitkov, Ceramics International, 24 (1998), 1-6.

[24] L.O. Snizhko, A.L. Yerokhin, A. Pikington, N.L Gurevina, D.O. Misnyankin, A. Leyland, A. Matthews, Electrochimica Acta, 49 (2004), 2085-2095.

[25] G.A. Markov and G.V. Mmarkova, USSR Patent 526961, Bulletin of Inventions, 32 (1976), 1

[26] A.V. Nikolaev, G.A. Markov, B.I. Peshchevitskij, Izv. SO AN SSSR. Ser. Khim. Nauk, 5 (12) (1977), 32.

[27] G.A. Markov, V.V. Tatarchuk, M.K. Mironova, Izv. SO AN SSSR. Ser. Khim. Nauk, 3 (7) (1983), 34.

[28] L.A. Snezhko, L.A. Beskrovnyj, Yu.M. Nevkrytyj, V.I. Tchernenko, Zashch. Met., 16 (3) (1980), 365.

[29] L.A. Snezhko, G.V. Rozenboym, V.I. Tchernenko, Zashch. Met.,17 (5) (1981), 618.

[30] L.A. Snezhko, V.I. Tchernenko, Elektron. Obrab. Mater., (2) (1983), 25.

[31] L.A. Snezhko, V.I. Tchernenko, Elektron. Obrab. Mater., (4) (1983), 38.

[32] V.I. Tchernenko, L.A. Snezhko, C.B. Tchernova, Zashch., Met. 20 (3) (1984), 454.

[33] L.A. Snezhko, S.G. Pavlus, V.I. Tchernenko, Zashch. Met., 20 (4) (1984), 292.

[34] G.A. Markov, M.K. Mironova, O.G. Potapova, Izv. AN SSSR. Ser. Neorgan. Mater., 19 (7) (1983), 1110

[35] A.A. Petrosyants, V.N. Malyshev, V.A. Fyedorov, G.A. Markov, Trenie Iznos, 5 (2) (1984), 350.

[36] V.N. Malyshev, S.I. Bulychev, G.A. Markov, V.A. Fyedorov, A.A. Petrosyants, V.V. Kudinov, M.H. Shorshorov, Fiz. Khim. Obrab. Mater., (1) (1985), 82.

[37] V.A. Fyedorov, V.V. Belozerov, N.D. Velikosel'skaya, S.I. Bulychev, Fiz. Khim. Obrab. Materialov, 4 (1988), 92.

[38] V.S. Rudnev, P.S. Gordienko, preprint no. 3384-B87, Inst. Khimii DVO AN SSSR,

Vladivostok, 1987.

[39] O.A. Khrisanfova, P.S. Gordienko, preprint no. 2986-B89, Inst. Khimii DVO AN SSSR, Vladivostok, 1987.

[40] P.S. Gordienko, P.M. Nedozorov, L.M. Volkova, T.P. Yarovaya, O.A Khrisanfova, Zashch. Met., 25 (1) (1989), 125.

[41] P. Kurze, W. Krysmann, G. Marx, Z. Wiss, Tech. Hochsch. Karl-Marx-Stadt, 24 (1982), 139.

[42] K.H. Dittrich, W. Krysmann, P. Kurze, H.G. Schneider, Cryst. Technol., 19 (1) (1984), 93.

[43] W. Krysmann, P. Kurze, K.H. Dittrich, H.G. Schneider, Cryst.Technol., 19 (7) (1984), 973.

[44] P. Kurze, J. Schreckenbach, T. Schwarz, W. Krysmann, Metalloberflaeche, 40 (12) (1986), 539.

[45] L.S. Saakian, A.P. Yefremov, L.Y. Ropyak, A.V. Apelfeld, Corrosion Control and Environment Protection. Informative survey, VNIIOENG, Moscow, (6), 1986.

[46] V.A. Fyedorov, A.G. Kan. R.P. Maksutov, Surface Strengthening of Oil & Gas Trade Facilities by Micro Arc Oxidation, VNIIOENG, Moscow, (6) 1989.

[47] G.A. Markov, B.S. Gizatullin, I.B. Rychazhkova, USSR Patent 926083, Bulletin of Inventions, 17, 1982.

[48] L.A. Snezhko, V.I. Techernenko, USSR Patent 973 583, Bulletin of Inventions 23, 1982.

[49] P. Kurze, W. Krysmann, G. Marx, K.H. Dittrich, DDR Patent DD-WP C25 D/236988(5).

[50] A.L. Yerokhin, X. Nie, A. Leyland, A. Matthews, S.J. Dowey, Surface & Coatings

Technology, 122 (1999), 73-93.

[51] A.L. Yerokhin, L.O. Snizhko, N.L. Gurevina, A. Leyland, A. Pilkington, A. Matthews, J. Phys, D: Appl. Phys., 36 (2003), 2110-2120.

[52] A.L. Yerokhin, L.O. Snizhko, N.L. Gurevina, A. Leyland, A. Pilkington, A. Matthews, Surface & Coatings Technology, 177-178 (2004), 779-783.

[53] S. Ikonopisov, A. Girginov, M. Machrova, Electrochim. Acta, 24 (1979), 451.

[54] A.L. Yerokhin, A. Leyland, A. Matthews, Applied. Surface. Science, 200 (2002), 172-184.

[55] L.O. Snizhko, A.L. Yerokhin, A. Pilkington, N.L. Gurevina, D.O. Misnyakin, A. Leyland, A. Matthews, On-line Abstracts of 8th European Congress on Advanced Materials and Processes EUROMAT 2003, 1-5 September, Lausanne, Switzerland, Symposium F6, www.Euromat2003.fems.org.

[56] N Klein, Thin Solid Films, 50 (1978), 223.

[57] J.M. Albella, I. Montero, J.M. Martinez-Duart, Electrochim. Acta, 32(1987), 255 (1984), 973.

[58] A.Hickling, M.D. Ingram, Trans. Faraday Soc., 60 (1964), 783.

[59] H.E. Wagner, R. Brandenburg, K.V. Kozlov, A. Sonnenfeld, P. Michel, J.F. Behnke, Vacuum, 71(2003), 417.

[60] www.techplate.com.tw, supported by Techplate International Co., Ltd.

[61] A.L. Yerokhin, A.A. Voevodin, V.V. Lyubimov, J. Zabinski, M. Donley, Surface & Coatings Technology, 110 (1998), 140-146.

[62] X.Nie, A. Leyland, H.W. Song, A.L. Yerokhin, S.J. Dowey, A. Matthews, Surface and Coatings Technology, 116-119 (1999), 1055-1060

[63] L.R Krishna, K.R.C. Somaraju, G. Sundararajan, Surface & Coatings Technology,

163-164 (2003), 484-490

[64] V.D.N Rao, H.A. Cikanek, B.A. Boyer, SAE paper, 970022, 1997

[65] X. Nie, L. Wang, E. Konca, A.T. Alpas, Surface & Coatings Technology, 188-189 (2004), 207-213

[66] W.B Xue, C. Wang, Y.L Li, R.Y. Chen, T.H. Zhang, ISIJ International, 42 (2002), 1273-1277.

[67] M. Warmuzek, Aluminum-Silicon Casting Alloys: Atlas of Microfractographs, ASM International, 2004, p3.

[68] H. F. Okorn-Schmidt, IBM J. Res. Develop, 43 (1999), 351-365.

[69] Peter J. Blau, Frcition and wear transitions of materials: break-in, run-in, wear-in, Noyes, New Jersey, 1989, 275.

[70] P.K. Rohatgi, S. Ray, Y. Liu, International materials reviews, 37 (1992), 129

[71] CECW-ET Engineer Manual 1110-2-1424, Engineering and Design: lubricants and hydraulic, Department of the army, U.S. Army Corps of, Washington, 1999 p6-1-p6-10.

APPENDIX

The author's publications on plasma electrolytic oxidation (PEO) technology concerning the results from this thesis.

X. Nie, **L. Wang**, E. Konca, A.T. Alpas, Tribological Behaviour of Oxide/graphite Composite Coatings Deposited by using an Electrolytic Plasma Process, Surface & Coatings Technology, 188-189 (2004), 207-213.

L. Wang, X. Nie, Silicon effects on formation of EPO oxide coatings on aluminium alloys, Thin Solid Films, (August, 2005 in press)

X. Li, D.O. Northwood, **L. Wang**, and X. Nie, Corrosion Protection Properties of Anodic Oxide Coatings on an Al-Si alloy, Surface & Coatings Technology, (June 2005 Accepted)

The author's publications on other electrolytic plasma process (EPP) technology during the Master's program in the University of Windsor:

X. Nie and **L. Wang**, Z.C. Yao, L. Zhang and F. Cheng, Sliding Wear Behaviour of Electrolytic Plasma Nitrided Cast Iron and Steel, Surface & Coatings Technology (June 2005 Accepted).

VITA AUCTORIS

Linlin Wang was born in 1975 in Anshan, Liaoning, P.R. China. She obtained her B.Sc. and M.A.S. from Anshan Institute of Iron and Steel Technology in Materials Engineering in 1997 and 2001. She is currently a candidate for the Master's degree in Engineering Materials at the University of Windsor and hopes to graduate in Fall 2005.